

For Limited Circulation Only

Contents

Message from the President and Secretary, ISRAPS	i
Editor's Desk	iii
Cavity Ring-down Spectroscopy coupled to Quantum Cascade Lasers: applications to atmospheric trace gas sensing <i>Manik Pradhan</i>	1
Gas Phase Photo-oxidation of Selected Atmospherically Important VOCs <i>Aparajeo Chattopadhyay, Koushik Mondal and Piyali Chatterjee</i>	10
Role of volatile organic air pollutants in lower atmospheric chemistry, their sources and health concerns <i>Dipanjali Majumdar</i>	21
Developing a dual channel receptor for Cu ²⁺ and F ⁻ by structural Modification: a comparative review <i>Arghyadeep Bhattacharyya, Subhash Chandra Makhal, Subhajit Saha and Nikhil Guchhait</i>	27
Carbonic Acid Isomerization and Decomposition Chemistry of Potential Atmospheric Significance <i>Sourav Ghoshal and Montu K. Hazra</i>	34
Cl Atom Radical Initiated Photo-Oxidation Reaction Kinetics of Alkyl Esters <i>Ramya Cheramangalath Balan and Rajakumar Balla</i>	39
Morpholine: In Gas Phase and Interface <i>Sumana SenGupta, Ankur Saha, Awadhesh Kumar and P.D. Naik</i>	46

ISRAPS Bulletin

SPECIAL ISSUE

On

ATMOSPHERIC CHEMISTRY



Guest Editors

Tapas Chakraborty
Sumana Sengupta

Message from the President and Secretary

Dear ISRAPS Members,

On behalf of the ISRAPS Executive Council, we take this opportunity to acknowledge all the ISRAPS Life Members and other researchers who have contributed in organizing various activities of ISRAPS at different institutes across the country.

Contributing to ISRAPS outreach program in the diverse area of Radiation and Photochemistry, ISRAPS in collaboration with Indian Photobiology Society, organized a One Day Discussion Meeting on Spectroscopy and Dynamics of Chemical and Biological Systems at Kolkata on 5th May 2018. Moving ahead, this thematic One Day Discussion Meeting on Atmospheric Chemistry is being organized jointly by ISRAPS and Indian Association for the Cultivation of Science (IACS), Kolkata on November 24, 2018, at IACS. The meeting would focus on the state of the art research on Atmospheric Chemistry, undertaken by different research groups in the country. This would also be beneficial to start collaboration, based on mutual interests, by sharing technical information among the research groups in the community. This bulletin is a collection of articles on the topics discussed in the meeting. The Executive Council of ISRAPS takes this opportunity to thank all the speakers/contributors of this discussion meeting and express our gratefulness to Prof. Tapas Chakraborty and Dr. Sumana SenGupta for organising and Guest Editing this issue. ISRAPS executive council sincerely requests all the member scientists and students to participate and contribute whatever way possible to the spread the knowledge of Radiation and Photochemical Sciences among young researchers in the country. The society will be happy to provide all logistic support for such an event.

ISRAPS looks forward to the forthcoming National Symposium on Radiation and Photochemistry (NSRP-2019) at Visva Bharati, Santiniketan, Kolkata, during Feb. 7-9, 2019, organized in collaboration with Integrated Science Education and Research Centre. The participation details and the abstract submission process are available at www.israps.org.in. The ISRAPS council wish to express our sincere gratitude to all life members for their constant support and encouragement. The council looks forward to your valuable suggestions and active participation in the forthcoming events of ISRAPS.



(P. D. Naik)
President, ISRAPS



(A. C. Bhasikuttan)
Secretary, ISRAPS



ISRAPS Bulletin

A Publication of
Indian Society for Radiation and Photochemical Sciences

Editor's Desk...

We are pleased to bring out this special issue of ISRAPS bulletin on 'Atmospheric Chemistry', in the occasion of a one-day Discussion Meeting organized at IACS Kolkata on November 24, 2018, jointly with ISRAPS. The need of atmospheric chemistry research with respect to parameters of our everyday life does not require to be overstated. The atmosphere is connected to everything of this planet and our societal system. The vital parameter of the atmosphere is the composition of its trace gases that determine the climatic condition and crucial for sustainability of life on the earth. The composition, as recorded in the pre-industrial ages, was the outcome of a critical balance of interactions involving land, ocean, biosphere and radiation. The impact of anthropogenic emissions in the post-industrial era on the balance of trace gas composition is found to be intimately linked with the photochemical processes occurring in the atmosphere. Therefore, it is indeed a rational step, on the part of Indian Society for Radiation and Photochemical Sciences, to initiate a discussion meeting on Atmospheric Chemistry, and to support in publishing this special bulletin.

The present issue of this bulletin is enriched with seven articles describing research ranging from field measurements for abundances of trace atmospheric gases in different geographic and urban environments to laboratory investigations of the fate as well as reaction kinetics of these trace gases under exposure of radiation. The guest editors sincerely thank the authors for their sincere cooperation and efforts in writing the articles in extremely short notice. The time and effort put by Ms. Piyali Chatterjee, Senior Research Scholar in the School of Chemical Sciences of IACS in technical editing of all the articles are also acknowledged gratefully.

Tapas Chakraborty & Sumana Sengupta
(Guest Editors)



Dr. Tapas Chakraborty is currently a Senior Professor of Physical Chemistry in the School of Chemical Sciences of Indian Association for the Cultivation of Science (IACS), Kolkata, since 2007. He was a member of the faculty of chemistry at IIT Kanpur during 1994-2007. His research interest is gas phase photochemistry relevant to atmospheric processes, LIF spectroscopy of molecular complexes, matrix isolation infrared spectroscopy and mass spectrometry. Dr. Chakraborty got his Ph.D. Degree from Jadavpur University working at IACS under the supervision of Late Prof. Mihir Chowdhury, and he also worked as a postdoctoral researcher with Prof. Edward C Lim at the University of Akron, USA. He was a DAAD visiting Scholar at Technical University of Munich, Germany, during 1996-97, and worked as visiting Associate Professor at the Department of Physics and Astronomy, University of Aarhus, Denmark, in the year 2005. Dr. Chakraborty is an elected fellow of the Indian Academy of Sciences, Bangalore.



Dr. Sumana SenGupta obtained her M. Sc. Degree from University of Calcutta in the year 2001, and obtained her Ph.D. degree from Homi Bhabha National Institute in 2012. She joined Bhabha Atomic research centre in 2002. Her current interest lies in the research and development in chemistry of environmentally important molecules in the gas phase and different interfaces.



INDIAN SOCIETY FOR RADIATION AND PHOTOCHEMICAL SCIENCES (ISRAPS)

EXECUTIVE COUNCIL (2018-2020)

President

Dr. P. D. Naik

Vice-Presidents

Prof. S. Wategaonkar

Dr. D. B. Naik

Secretary

Dr. A.C. Bhasikuttan

Joint Secretary

Prof. A. Datta

Treasurer

Dr. (Mrs) J. Mohanty

Executive Members

Dr. S. Adhikari

Dr. T. Bandyopadhyaya

Dr. Atanu Barik

Prof. T. Chakraborty

Dr. Alope Das

Dr. Awadhesh Kumar

Prof. A. S. Kumbhar

Dr. S. Nath

Dr. D. K. Palit

Dr. C. N. Patra

Prof. P. Ramamurthy

Dr. H. P. Upadhyaya

Co-opted Members

Dr. Y.K. Bhardwaj

Dr. G. R. Dey

Dr. T. K. Ghanty

Dr. (Mrs) Nandita Maiti

Dr. J. P. Mittal

Dr. J. A. Mondal

Dr. Alok Samanta

Dr. S. K. Sarkar

Dr. (Mrs) S. Sen

Gupta

Prof. Anil K. Singh

Dr. V. S. Tripathi

Dr. R.K. Vatsa

Web Master

Mr. Abhishek Das

Contact Details:

C/o Radiation & Photochemistry Division

Bhabha Atomic Research Centre, Mumbai - 400 085

E-mail: israps.secretary@gmail.com

Telephone: (022)- 25595398/25593866/25593771

Web: www.israps.org.in



Indian Society for Radiation and Photochemical Sciences

(Reg. No. 617/1985, GBBSD, Bombay; Trust No. F-10965)

Radiation & Photochemistry Division

Bhabha Atomic Research Centre, Mumbai - 400 085

Member Enrolment Form

1. Name in Block Letters:
2. Date of Birth:
3. Highest Academic Qualification:
4. Present Position:
5. Addresses:

Photograph

Office	Residence
Telephone E-mail	Telephone E-mail

6. Address for Correspondence: Office / Residence
7. Category of Membership Applied for: Annual / Life / Corporate member
8. Remittance: DD in favour of 'ISRAPS' payable at MUMBAI
For Bank Transfer:
A/c No.10536133801, SBI, BARC Branch, IFSC SBIN0001268
(e-mail the money transfer details along with the details requested above to israps.secretary@gmail.com and CC to bkac@barc.gov.in)

Category	Fees	Admission fee	Total Amount
Annual	Rs 200/-	Rs 100/-	Rs 300/-
Life Member	Rs 1500/-	Rs 100/-	Rs 1600/-
Corporate Member	Rs 20000/-	Rs 1000/-	Rs 21000/-

9. Brief Resume of activities and research interests:
10. List of memberships of other professional bodies, if any:
11. List of prizes/awards/fellowships received, if any:
12. Number of Publications:

I agree to abide by the constitution and bye-laws, and rules and regulations of the SOCIETY.

Place:

Signature

Date:

Contents

Message from the President and Secretary, ISRAPS	i
Editor's Desk	iii
Cavity Ring-down Spectroscopy coupled to Quantum Cascade Lasers: applications to atmospheric trace gas sensing <i>Manik Pradhan</i>	1
Gas Phase Photo-oxidation of Selected Atmospherically Important VOCs <i>Aparajeo Chattopadhyay, Koushik Mondal and Piyali Chatterjee</i>	10
Role of volatile organic air pollutants in lower atmospheric chemistry, their sources and health concerns <i>Dipanjali Majumdar</i>	21
Developing a dual channel receptor for Cu²⁺ and F⁻ by structural modification: a comparative review <i>Arghyadeep Bhattacharyya, Subhash Chandra Makhal, Subhajit Saha and Nikhil Guchhait</i>	27
Carbonic Acid Isomerization and Decomposition Chemistry of Potential Atmospheric Significance <i>Sourav Ghoshal and Montu K. Hazra</i>	34
Cl Atom Radical Initiated Photo-Oxidation Reaction Kinetics of Alkyl Esters <i>Ramya Cheramangalath Balan and Rajakumar Balla</i>	39
Morpholine: In Gas Phase and Interface <i>Sumana SenGupta, Ankur Saha, Awadhesh Kumar and P.D. Naik</i>	46

Cavity Ring-down Spectroscopy coupled to Quantum Cascade Lasers: applications to atmospheric trace gas sensing

Manik Pradhan

Department of Chemical, Biological and Macromolecular Sciences, S. N. Bose National Centre for Basic Sciences, Salt Lake, JD Block, Sector III, Kolkata-700106, India

Email: manik.pradhan@bose.res.in

<http://bose.res.in/~manik.pradhan/index.htm>

Abstract

A number of atmospheric pollutants and greenhouse gases have strong fundamental vibrational transitions in the mid-IR spectral range (4-24 μm), which marks the region particularly important for trace gas sensing. Here, we present our recent developments of mid-IR continuous-wave (cw) cavity ring-down spectroscopy (CRDS) techniques coupled with external-cavity (EC) mode-hop-free (MHF) quantum cascade lasers (QCL) operating at both 5.2 μm and 7.5 μm . We validated the EC-QCL based high-resolution cw-CRDS system by measuring several molecular species such as $^{12}\text{CH}_4$ and $^{13}\text{CH}_4$ isotopes of methane (CH_4) along with nitrous oxide (N_2O) which served as benchmark molecules. The direct, quantitative and selective measurements of ^{12}C and ^{13}C isotopes of CH_4 as well as N_2O in ambient air in the levels of parts per billion by volume (ppbv) were made by probing rotationally resolved vibrational transitions of CH_4 and N_2O . We achieved a noise-equivalent absorption coefficient (NEA) of $1.86 \times 10^{-9} \text{ cm}^{-1}\text{Hz}^{-1/2}$ with 100 Hz data acquisition rate for the current cw-CRDS spectrometer. The current high-resolution cw-CRDS system could be further exploited to harness the full advantage of the spectral region to monitor several other trace molecular species along with their isotopic compositions.

1. Introduction

The mid-infrared (mid-IR) spectral band extending from 4-24 μm is considered to be the key “molecular fingerprint” region with strong characteristic fundamental vibrational transitions of several important greenhouse gases (i.e. CH_4 and N_2O) and atmospheric pollutants (i.e. H_2S , NO , SO_2 , OCS , HNO_3 , C_2H_2 and H_2O_2). This spectral region thus provides a unique opportunity to study numerous trace molecules within a single and relatively small spectral range along with to understand the atmospheric chemistry in real-time. Moreover, particularly the 7.5-8 μm spectral region is in the close vicinity of atmospheric transmission window of 8-13 μm , which makes the spectral

region important for applications in high-resolution molecular spectroscopy and atmospheric trace gas sensing. However, this spectral band covering 7.5-8 μm along with several other mid-IR regions such as 5.2 μm has not extensively been studied earlier due to unavailability of laser source lasing in this mid-IR region. The recent advancements in sophisticated continuous-wave (cw) external-cavity (EC) quantum cascade laser (QCL) technology opens up a new frontier providing the access to entire mid-IR region ranging from 3 μm to 25 μm and thus enabling us to explore the high-resolution fundamental vibrational transitions of molecules with unprecedented molecular selectivity.

The high-finesse optical cavity enhanced absorption techniques such as integrated cavity output spectroscopy (ICOS) and cavity ring-down spectroscopy (CRDS) have widely been employed to achieve ultra-high sensitivity of 10^{-9} - 10^{-11} cm^{-1} , thus facilitating the measurement capability of trace molecular species as low as parts-per-trillion (ppt) levels. CRDS is an ultra-sensitive direct optical absorption technique where decay-rate of optical signal, trapped in a high-finesse optical cavity has been utilized for ultra-low and high-precision measurements of molecular concentration. But, the reports of *cw*-CRDS technique combined with the latest *cw* EC-QCL are still very limited in the mid-IR spectral region due to unavailability and prohibitively expensive optical components such as optical isolator and acousto-optic modulator (AOM).

Therefore, the aim of the report is to demonstrate the potential of *cw*-CRDS techniques coupled with EC-QCLs operating at some specific wavelengths such as $5.2 \mu\text{m}$ and $7.8 \mu\text{m}$ for selective and quantitative detection of atmospheric trace gases in real-time by means by high-resolution molecular spectroscopy. studies. We validated the CRD spectrometer by ultra-sensitive direct detection of methane isotopes ($^{12}\text{CH}_4$ and $^{13}\text{CH}_4$), nitrous oxide (N_2O), acetylene (C_2H_2), carbonyl sulphide (OCS) etc which served as benchmark molecules in the mid-IR spectral region with strong fundamental vibrational transitions.

2. Experimental Setup and Cavity Ring-down Methodology

The experimental set-up is depicted in Fig. 1. A room temperature water-cooled *cw* EC-QCL (Daylight Solutions, USA) with mode-hop-free (MHF) tunability was utilized as a high-resolution ($<0.0003 \text{ cm}^{-1}$) and high power ($<100 \text{ mW}$) optical source for *cw*-CRDS sensor.

The highly collimated laser light was first allowed to pass through an optical isolator (FIO-5-7.8; Innovation Photonics) and subsequently through an acousto-optic modulator (AOM; AGM406B11M; IntraAction Corp; USA) which acts as an optical Bragg-diffractor to produce zeroth-order and first-order laser beams. The zeroth-order beam was directed to a wavemeter (621B-MIR; Bristol Instruments) for real-time and continuous monitoring of laser wavelength with an accuracy of $\pm 0.001 \text{ cm}^{-1}$, whereas the first-order beam was precisely aligned along the central-axis of the optical cavity. The high-finesse cavity was formed by placing two high-reflective (HR) mirrors (CRD Optics Inc.; USA) with manufacturer specified reflectivity of $R > 99.98\%$ at $7.35 \mu\text{m}$ and 1 metre radius of curvature (ROC) at the two ends of a 50 cm long quartz-coated ring-down cell (RDC). The optical signal was finally focused on to a four-stage thermo-electrically cooled photovoltaic mercury-cadmium-telluride (MCT) detector (PVI-4TE-8-1X1; Vigo System S.A.) using a gold-coated 90° off-axis parabolic mirror (50338 AU; Newport Corporation). The detector was further connected to an external low-noise voltage pre-amplifier (SR560; Stanford Research Systems) for amplification of electrical signal.

We next utilized cavity-length modulation technique to achieve the periodic resonance between laser mode and cavity mode. We applied ~ 60 Volt in parallel to the three piezoelectric transducers (PZT, Thorlabs PE4) attached to the front mirror-mount, using a triangular ramp function ($V_{pp} = 2.91\text{V}$, 50 Hz, 15X gain), to modulate the length of the cavity over one free-spectral-range (FSR) or half of the wavelength ($\lambda/2$). An intra-cavity light intensity (TEM_{00} mode) was built-up periodically inside the optical cavity when the

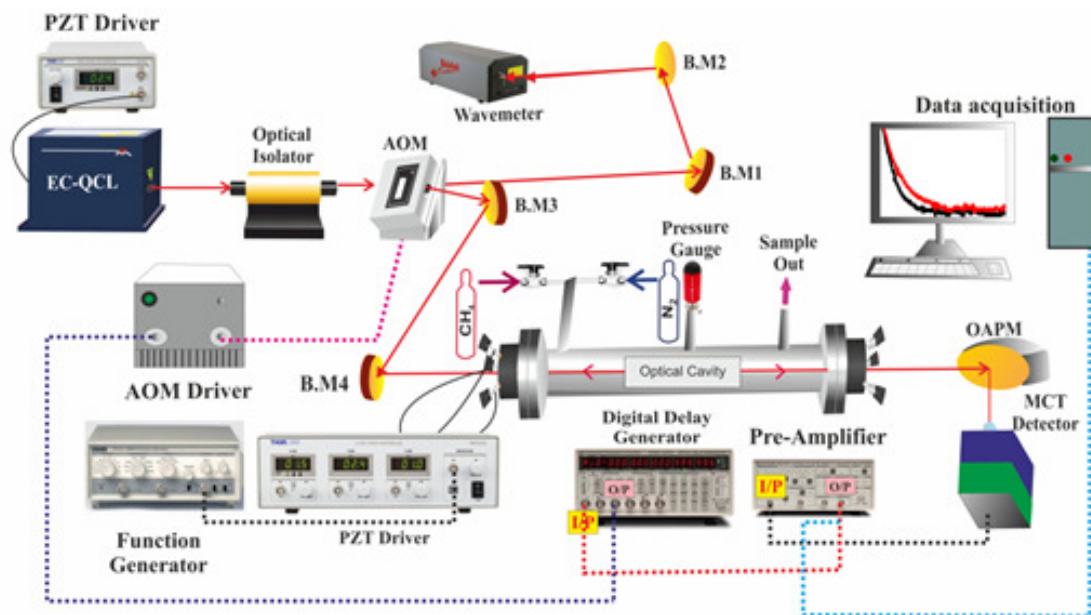


Fig. 1. A schematic representation of the experimental set-up.

frequency of cavity mode matches with the laser mode frequency. The intra-cavity light intensity whenever reached to a pre-defined value, a pulse-delay generator (DG645; Stanford Research Systems) connected to the AOM driver was utilized to switch-off the first-order diffracted beam and an exponential decay of the intra-cavity light was observed. The exponential decay trace was captured by a high-speed (100 MS/s) data-acquisition card (5122 PCI National Instrument, 14-bit, 100 MHz bandwidth) and subsequently analysed by a custom-written LabVIEW program.

In the present EC-QCL based cw-CRDS system, we achieved an empty cavity ring-down time of $\tau_0 = 14.13 \mu\text{s}$ and standard deviation (1σ) of 0.56% with an averaging of 5 successive ring-down events. Based on these parameters the limiting sensitivity of the cw-CRDS system was estimated to be $\alpha_{\text{min}} = 1.32 \times 10^{-8} \text{ cm}^{-1}$. However, to assess the laser line-width, we modulated the cavity-length over one FSR to excite two successive TEM_{00} modes in a single piezo scanning (Fig. 2a) and subsequently studied the individual TEM_{00} mode (Fig. 2b). Thus, we obtained the time-

scaled values of FSR (Δt_{FSR}) and individual TEM_{00} ($\Delta t_{\text{TEM}_{00}}$) mode. Then using the relation, $\Delta \gamma_{\text{QCL}} / \text{FSR} = \Delta t_{\text{TEM}_{00}} / \Delta t_{\text{FSR}}$ and the known value of FSR ($= c/2l$) of 300 MHz, we found the line-width of QCL ($\Delta \gamma_{\text{QCL}}$) of 13.66 MHz (i.e. 0.0004 cm^{-1}) which was in good agreement with the manufacturer specified linewidth ($< 0.0003 \text{ MHz}$) of the current EC-QCL source. In contrast, the cavity line-width was measured to be $\Delta \gamma_{\text{Cavity}} = (\text{FSR} / \text{Finesse}) = 11.46 \text{ kHz}$. Therefore, the high-finesse ($F \sim 26000$) optical cavity coupled with an extremely narrow linewidth of cw EC-QCL provided an excellent platform for high-resolution and high-sensitivity spectral study of molecular absorptions.

We subsequently investigated the stability of the cw-CRDS spectrometer by means of Allan variance analysis to determine the optimum integration time to maximize the signal to noise ratio and thereby improving the limiting sensitivity of the current method. Figure 2c depicts a plot of the Allan-variance (σ_{λ}^2) of empty cavity ring-down times (τ_0) against the integration time (t) at a particular wavelength $\sim 7.5 \mu\text{m}$ with a data acquisition

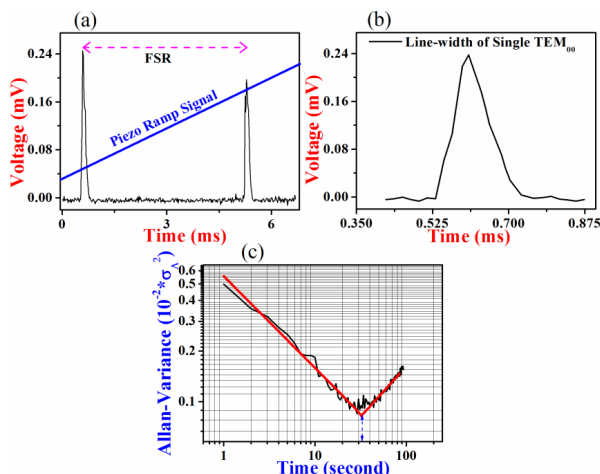


Fig. 2. (a) Laser-cavity resonances during cavity mirror oscillation over one free-spectral-range (FSR), (b) A zoom-in of single resonance, and (c) An Allan-variance plot of empty cavity ring-down time (τ_0).

rate of 100 Hz. The log-log plot of the Allan-variance initially decreased linearly with the increase of integration time as the increase of data averaging reduces the noise level. We found an optimum integration time of 33 seconds which corresponds to 3300 ring-down decay signals for 100 Hz data acquisition rate and a noise-equivalent absorption coefficient (NEA) of $1.86 \times 10^{-9} \text{ cm}^{-1}\text{Hz}^{-1/2}$ was achieved. However, after 33 sec there is no advantage of additional signal averaging since several instabilities arise in the system.

3. Results and Discussions

3.1 Trace detection of methane isotopes in ambient air by QCL-based CRDS at 7.8 μm

Methane (CH_4) is the second most important anthropogenically emitted greenhouse gas possessing global warming potential (GWP) 25 times greater than that of CO_2 over a 100 year time horizon and the present atmospheric concentration of CH_4 has been increased by 166% since the pre-industrial times. The measurements of methane isotopes will provide the process-specific information

and the possible sources and sinks of the molecule. However, we evaluated the performance of the *cw*-CRDS sensor for sensitive, accurate quantitative measurements of ^{12}C and ^{13}C isotopes of CH_4 within 7.5-8 μm region by probing the interference-free molecular transitions of $^{12}\text{CH}_4$ and $^{13}\text{CH}_4$ isotopes arising from the fundamental symmetric bending (ν_4 band) vibrations of the bonds located at $\sim 1327.244 \text{ cm}^{-1}$ and $\sim 1332.946 \text{ cm}^{-1}$, respectively, as shown in the HITRAN simulated spectra (Figure 3a and 3b). Figure 4a and 4b shows the examples of the high-resolution *cw*-CRDS spectra of CH_4 isotopes when certified calibration gas mixtures of $9.62 \pm 0.05 \text{ ppm}$ of $^{12}\text{CH}_4$ and $438 \pm 2 \text{ ppb}$ of $^{13}\text{CH}_4$

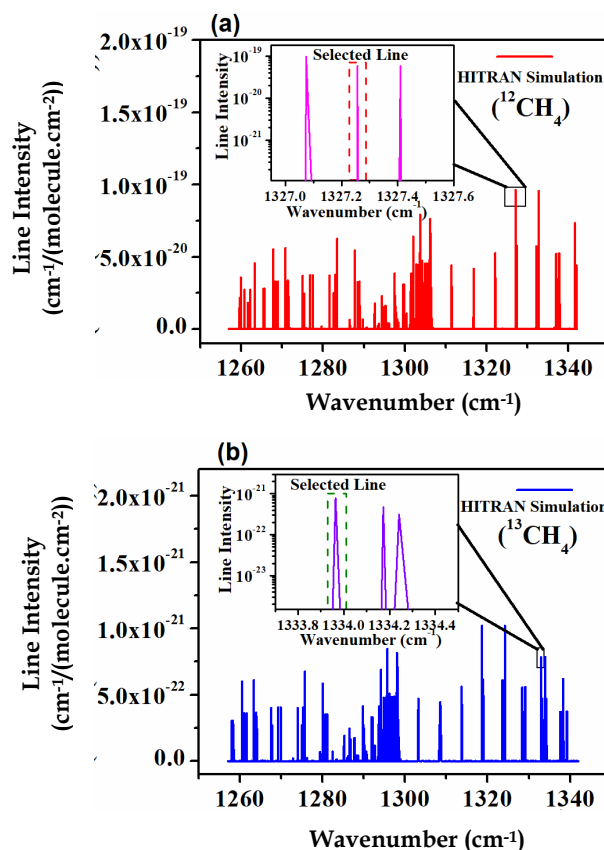


Fig. 3. (a) and (b) The simulated spectra from HITRAN database for ^{12}C and ^{13}C -isotopes of CH_4 , respectively in the spectral region covering 7.5-8 μm . The dotted regions represent the selected absorption lines of CH_4 isotopes.

in N₂ (Air Liquid, Uk and CIL, USA) were injected into the optical cavity with a pressure of 1 Torr and 15 Torr, respectively and spectral lines were fitted with the Voigt line-shape functions.

We then injected different concentrations of calibration standards of ¹²CH₄ and ¹³CH₄ isotopes into the optical cavity and acquired the wavenumber (cm⁻¹) dependent change of decay-rate (Δk in s⁻¹) across the selected molecular transitions. The integrated area under each absorption curve (cm⁻¹s⁻¹) was

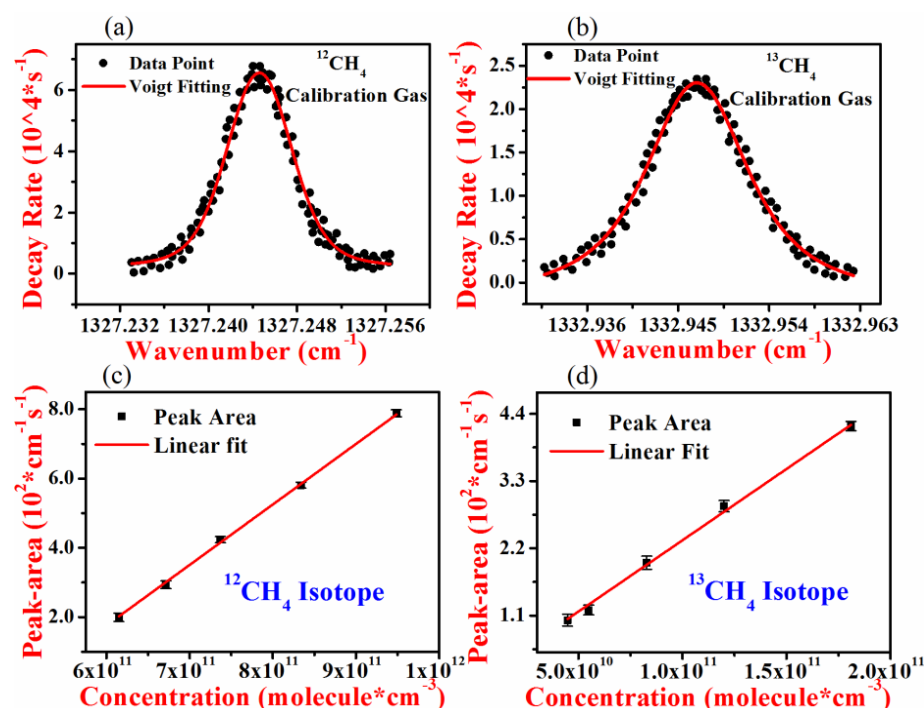


Fig. 4. (a), (b) CRDS spectra of calibration gases showing decay rate vs wavenumber plot of ¹²C and ¹³C isotopes of CH₄ centred at $\sim 1327.244 \text{ cm}^{-1}$ and $\sim 1332.946 \text{ cm}^{-1}$ respectively and fitted with voigt function, (c), and (d) a linear regression plot between the area of CRDS spectra and molecular concentration of ¹²C and ¹³C isotopes of CH₄ respectively.

plotted (Figure 4c ad 4d) against the different concentrations (i.e., no. of molecules cm⁻³) and from the linear regression plot, the line-integrated absorption cross-sections were determined to be $(\sigma_I)^{12}\text{CH}_4 = 5.82 \times 10^{-20} \text{ cm}^{-1} \text{ molecule}^{-1} \text{ cm}^2$ and $(\sigma_I)^{13}\text{CH}_4 = 7.8 \times 10^{-22} \text{ cm}^{-1} \text{ molecule}^{-1} \text{ cm}^2$ (normalized with isotopic

abundances), respectively for the molecular transitions of ¹²C and ¹³C-isotopes of CH₄ at the selected molecular transitions, which were in excellent agreement with the values reported in HITRAN database.

We next studied the pressure broadening effect on the absorption spectra of ¹²C and ¹³C-isotopes of CH₄ at the designated wavenumbers, introducing zero-air in the optical cavity, and simultaneously assessed the parameters of sensitivity and selectivity of the CRDS sensor at the higher pressure because the

pressure broadening has a direct effect on these parameters. Figure 5a and 5b illustrates the ring-down spectra for both the isotopes at different cavity-pressures retaining the same numbers of CH₄ molecules inside the cavity. A significant reduction of the peak height of isotopic CH₄ spectra was observed with increasing the pressure in the cavity. The spectra of such absorption lines were fitted with Voigt line-shape functions. Figure 5c and 5d shows the plots of the full-width half-maxima (FWHM in cm⁻¹) of the absorption lines of

¹²CH₄ and ¹³CH₄ isotopes against the different cavity-pressures (in Torr). The gradient of the linear regression of the plot provided the pressure-broadening coefficient of $0.067 \text{ cm}^{-1} \text{ atm}^{-1}$ and $0.052 \text{ cm}^{-1} \text{ atm}^{-1}$, respectively for ¹²C and ¹³C-isotopes of CH₄ which were in good agreement with the HITRAN values.

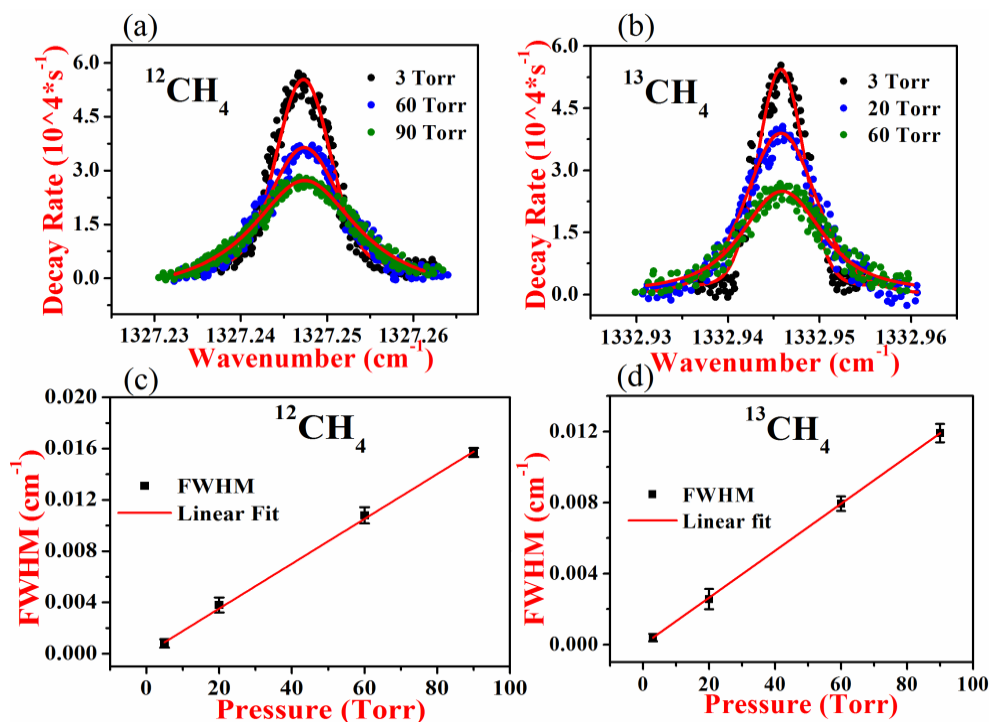


Fig. 5. (a), (b) Variation of absorption spectra of ^{12}C and ^{13}C isotopes of CH_4 respectively at different cavity pressures, (c), and (d) a linear regression plot between FWHM of absorption spectra and cavity pressures for ^{12}C and ^{13}C isotopes of CH_4 respectively.

Moreover, we observed that sample pressure inside the ring-down cavity can be increased up to 100 Torr without any significant overlapping with the adjacent foreign molecular transitions such as H_2O , CO_2 and N_2O and hence the sensitivity and specificity of the *cw*-CRDS sensor for CH_4 detection remain unaltered at that pressure limit. We also calculated the minimum detection limit of the CRDS-based CH_4 sensor to be 396 pptv and 287 pptv, respectively for ^{12}C and ^{13}C -isotopes of CH_4 at 100 Torr cavity-pressure without any deleterious effects of pressure broadening.

We finally evaluated the potential of the EC-QCL based CH_4 sensor exploiting the *cw*-CRDS technique for real-time monitoring of isotopic CH_4 concentrations

in ambient air. Figure 6a and 6b depicts the CRDS spectra of isotopic CH_4 in ambient air samples and the concentration levels of ^{12}C and ^{13}C -isotopic compositions of CH_4 were estimated to be 1200.4 ± 0.9 ppbv and 12.8 ± 0.8 ppbv, respectively. These observations suggest that the present EC-QCL based CH_4 sensor for quantitative detection of individual isotopes in the mid-IR spectral range has enormous potential to be applied in environmental sensing purposes.

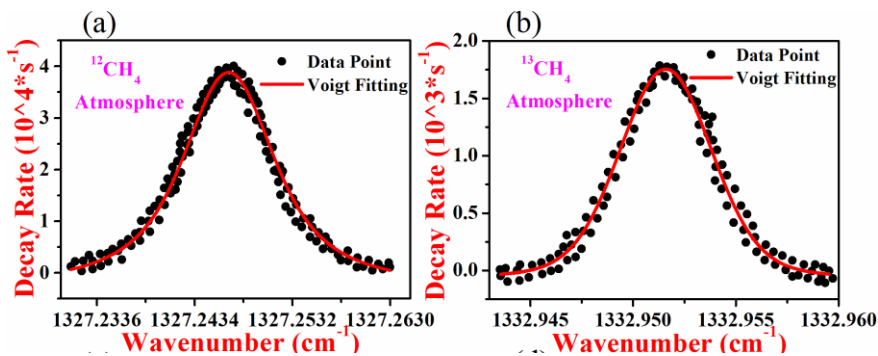


Fig. 6. CRDS spectra of ^{12}C and ^{13}C isotopic concentrations of CH_4 in (a), (b) ambient air at 20-30 Torr sample pressure.

3.2 Tracking Methane (CH₄) concentrations in different locations at Kolkata by CRDS

We next employed the present lab-based sensor for routine monitoring of atmospheric CH₄ originated from various anthropogenic sources to assess the feasibility as a future field-deployable sensor. We identified various sources of atmospheric CH₄ as listed in Table I, within a radius of 10 km around our institute, S. N. Bose Centre, Kolkata and collected air samples in Tedlar bags or small canisters each day of a week. Each sample was measured thrice and standard 1 ppm of CH₄ was measured between any two successive measurements of the atmospheric samples to ensure the measurement accuracy. Moreover, zero air was measured at the

We speculate that the anaerobic biodegradation of organic compounds in paddy fields and bacterial action in the digestive tracts of the ruminant animals in the dairy farm may have possibly attributed to the high evolvment of methane at the respective local environments. In contrast, the biodegradation of the industrial waste product may possibly contribute to the enrichment of CH₄ concentration in the industrial sector, but the detailed long-term and continuous monitoring of CH₄ are required to get insight into the actual source dependent CH₄ emission in our study. However, all the atmospheric samples were additionally measured by the residual gas analyzer mass-spectrometry system to validate the measurement accuracy of the QCL-based CRDS

	CH ₄ concentration in ppm									
	Paddy field		Industrial sector		Dairy farm		Wetland		Institute campus	
	Morning (06:00–07:00)	Afternoon (15:00–16:00)	Morning (06:00–07:00)	Afternoon (15:00–16:00)	Morning (06:00–07:00)	Afternoon (15:00–16:00)	Morning (06:00–07:00)	Afternoon (15:00–16:00)	Morning (06:00–07:00)	Afternoon (15:00–16:00)
DAY 1	3.94 ± 0.039	4.94 ± 0.033	4.2 ± 0.052	4.3 ± 0.055	7.8 ± 0.078	6.9 ± 0.073	2.4 ± 0.023	2.3 ± 0.023	1.87 ± 0.034	1.86 ± 0.024
DAY 2	4.3 ± 0.067	4.1 ± 0.057	4 ± 0.037	4.2 ± 0.039	8.2 ± 0.08	8.9 ± 0.076	2.5 ± 0.035	3.5 ± 0.035	1.83 ± 0.044	1.89 ± 0.044
DAY 3	4.2 ± 0.065	4.6 ± 0.069	4.6 ± 0.067	4.1 ± 0.061	7.9 ± 0.049	9 ± 0.049	2.5 ± 0.025	3.1 ± 0.025	1.88 ± 0.069	1.98 ± 0.062
DAY 4	3.95 ± 0.055	4.3 ± 0.059	4.3 ± 0.032	4.3 ± 0.039	7.7 ± 0.067	8.7 ± 0.067	2.3 ± 0.028	3.2 ± 0.028	1.87 ± 0.024	1.82 ± 0.034
DAY 5	4.5 ± 0.034	4.3 ± 0.035	4.8 ± 0.031	4.8 ± 0.034	8.6 ± 0.063	7.6 ± 0.053	2.5 ± 0.022	2.7 ± 0.023	1.83 ± 0.07	1.96 ± 0.07
DAY 6	4.8 ± 0.044	4.4 ± 0.041	4.9 ± 0.059	4.9 ± 0.051	8.4 ± 0.069	8.0 ± 0.065	2.6 ± 0.021	2.9 ± 0.027	1.84 ± 0.052	1.94 ± 0.053
DAY 7	4.3 ± 0.045	4.6 ± 0.042	5.0 ± 0.055	5.0 ± 0.059	8.2 ± 0.039	8.5 ± 0.049	2.7 ± 0.017	2.3 ± 0.019	1.88 ± 0.027	1.98 ± 0.027

Table I: Comparison of CH₄ mixing ratios at the different locations around S. N. Bose Centre, Kolkata.

optimized experimental conditions in every occasion after each sample measurement to ensure the removal of the residual of the previous sample. All the measurements were carried out each day within 3 hours after collecting the samples from different sources. It is evident from the Table I that CH₄ concentration at the local environment varied from 1 ppm to 8 ppm depending on the nature of the sources. A map of the different locations of the collected samples has been depicted in Fig. 7. We observed that the level of CH₄ was quite high (4-8 ppm) for the sources like paddy field, and dairy farm in comparison to the atmospheric concentration of CH₄ (~1.8 ppm) present in the Institute campus.

technique. We found an excellent agreement between the measurements from both the systems which signifies the robustness and efficacy of the EC-QCL-based sensor for monitoring of atmospheric methane with a wide range of concentrations.

3.3 Trace detection nitrous oxide (N₂O) in the atmosphere by CRDS at 5.2 μm

Nitrous oxide (N₂O) is one of the most important atmospheric greenhouse gases, contributing to global warming as well as climate change. The global warming potential (GWP) of N₂O is about 300 times greater than carbon dioxide (CO₂) over a 100 year time horizon.

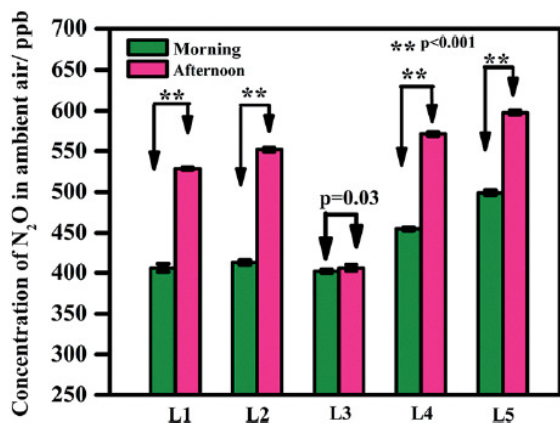


Fig. 7. Variation of ambient N₂O mixing ratios in different periods of the days in various sub-areas. L1: industrial sector, L2: highly traffic area, L3: residential complex, L4: agricultural land and L5: garbage disposal ground of Kolkata metropolitan.

In the atmosphere, N₂O is primarily originated from anthropogenic sources and also strongly influenced by human activities, in particular, the use of agricultural fertilizers. However, its mixing ratios in the troposphere are typically from 270 to 330 parts per billion by volume (ppbv, 1 part in 10⁹) and have been measured upto ~2000 ppbv in areas where soils are

effects in the atmosphere. Considering the environmental importance, real-time monitoring and molecule-specific detection of N₂O in the atmosphere with high sensitivity is of growing interest. We therefore focused to couple a widely tunable cw EC-QCL system to the high-resolution CRDS technique for accurate and selective measurements of N₂O in ppbv levels in ambient air.

The samples were collected from the five different localities surrounding S. N. Bose Centre, Kolkata on seven consecutive days (November, 4-10, 2016) in two different periods, morning (07:00-09:00 h) and afternoon (14:00-16:00 h). The sub-areas of our study included industrial sector (L1), highly traffic area (L2), residential complex (L3), agricultural land (L4) and garbage disposal ground of Kolkata metropolitan (L5). Air samples were analyzed by the cw-CRDS setup and the measured N₂O mixing ratios in the atmosphere were from 399 ppbv to 604 ppbv (see Figure 7 and Table 2) which lies in the typical range of N₂O emitted in the atmosphere depending on

Date	L1		L2		L3		L4		L5	
	Morning	Afternoon								
4.11.2016	399 ± 5	527 ± 7	410 ± 4	549 ± 7	401 ± 3	409 ± 5	456 ± 4	570 ± 3	495 ± 8	595 ± 5
5.11.2016	402 ± 4	533 ± 6	418 ± 3	553 ± 7	404 ± 3	413 ± 4	454 ± 6	570 ± 3	498 ± 6	604 ± 6
6.11.2016	404 ± 7	529 ± 7	413 ± 5	554 ± 4	401 ± 5	404 ± 8	453 ± 4	568 ± 4	498 ± 3	600 ± 3
7.11.2016	403 ± 9	528 ± 4	412 ± 5	553 ± 6	402 ± 5	404 ± 6	457 ± 3	574 ± 5	499 ± 7	596 ± 5
8.11.2016	409 ± 8	528 ± 4	412 ± 4	555 ± 5	402 ± 6	408 ± 6	458 ± 3	576 ± 7	499 ± 6	598 ± 8
9.11.2016	415 ± 6	529 ± 4	416 ± 3	549 ± 6	401 ± 7	403 ± 6	455 ± 4	574 ± 6	506 ± 4	597 ± 7
10.11.2016	410 ± 4	529 ± 6	411 ± 5	556 ± 5	407 ± 6	402 ± 5	454 ± 5	569 ± 6	501 ± 3	598 ± 4

Table 2: N₂O emission in a variety of environments in the different period of the day.

cultivated with artificial fertilizers. Therefore these values may differ strongly because of influence of the different anthropogenic and biogenic sources as well as depending on the level of local pollution. N₂O has atmospheric lifetime of several years (~120 years) and contributes to the ozone destruction in the stratosphere. Because of its stability and long atmospheric lifetime, even a small change in concentration of N₂O will have long-term

the level of local pollution. In our study, whilst we observed a significant change in N₂O levels in different sub-areas, interestingly we also observed a statistically significant difference (p<0.001) in N₂O concentrations between morning and afternoon sessions of the day in all sub-areas apart from the residential complex area (p = 0.03). In the cultivated land area, we found a significant change in N₂O levels in the afternoon session. This observation might be

attributed to the release of N_2O from the soil by an increase in soil microbial activity in the afternoon and also for use of different types of organic and inorganic fertilizers in the agricultural land as the samples were collected from such areas. On the other hand, in our study a higher level of N_2O was observed in the waste disposal land compared to the other sub-areas. This is possibly caused by the enhancement of biological processes of nitrification and denitrification of organic material by the different types of bacteria and fungus. Moreover, we also did not observe any significant changes of N_2O levels in the morning period between the traffic area and industrial sector, but N_2O concentration rises in the afternoon which is most likely a result of higher emission of anthropogenic sources in that period.

4. Conclusion

We have developed and tested a high-resolution *cw*-CRDS spectrometer coupled with a widely-tunable EC-QCL with MHF wavelength tuning capability working in the mid-IR spectral region of 7.5-8 μm and also for 5.2 μm for high-resolution measurements of trace gases. We have validated the system for direct quantitative estimation of $^{12}CH_4$ and $^{13}CH_4$ isotopologues of methane (CH_4) as well as N_2O without any sample pre-concentration unit. We have also demonstrated that the *cw*-CRDS sensor has the sufficient capability to measure the different isotopes of CH_4 and N_2O from various environments with ultra-high sensitivity in the levels of ppbv along with unprecedented molecular selectivity without overlapping any other trace molecular species. The high selectivity and sensitivity arise by probing the rotationally resolved absorption lines that have well-defined central frequency. In addition, recording the high-resolution ring-

down spectra at low pressures also eliminates the pressure broadening effects. Finally, the CRDS spectrometer can easily be adapted for monitoring several other isotopic species with mid-IR fundamental absorption bands such as SO_2 , HNO_3 and H_2O_2 with anticipated detection limits in the pptv range.

5. Relevant References Cited

- [1] "Cavity ring-down spectroscopy using an EC-QCL operating at 7.5 μm for direct monitoring of methane isotopes in air": A. Maity, M. Pal, G. D. Banik, S. Maithani and M. Pradhan. *Laser Physics Letters*, **14**, 115701 (2017).
- [2] "An EC-QCL based N_2O sensor at 5.2 μm using cavity ring-down spectroscopy for environmental applications": G. D. Banik, S. Som, A. Maity, M. Pal, S. Maithani, S. Mandal, C. Ghosh and M. Pradhan. *Analytical Methods*, **9**, 2315-2320 (2017).



Dr. Manik Pradhan is currently an Associate Professor at S. N. Bose National Centre for Basic Sciences, Kolkata, India. He obtained his PhD from the group of Professor Andrew Orr-Ewing in 2008 from the University of Bristol, England, having been awarded a prestigious Dorothy Hodgkin Postgraduate Fellowship. Subsequently, he moved to the University of Cambridge, England for his postdoctoral work (2008-2010) in the group of Professor Richard Lambert after receiving the Isaac Newton Trust Postdoctoral Fellowship from Trinity College, England. Hereafter, he came to work as a Postdoctoral Research Associate (2010-2011) in the group of Professor Richard Zare in Stanford University, USA. He also worked as a Visiting Research Assistant (2004-2005) at the Institute of Atomic and Molecular Sciences (IAMS), Academia Sinica, Taiwan.

Gas Phase Photo-oxidation of Selected Atmospherically Important VOCs

Aparajeo Chattopadhyay^b, Koushik Mondal^a and Piyali Chatterjee^a

^aDepartment of Physical Chemistry, Indian Association for the Cultivation of Science, 2A Raja S. C. Mullick Road, Jadaopur, Kolkata 700032, India, Email: pctc@iacs.res.in

^bChemical Processes & Instrument Development, Earth System Research Laboratory, NOAA ESRL Chemical Sciences Division, 325 Broadway R/CSD5 Boulder, CO 80305 USA

Abstract

Gas phase photo-oxidation studies of some atmospherically important volatile carbonyl compounds, carried out recently by our group, have been discussed here. All measurements were performed in simulated atmospheric environment (synthetic air, 1 bar pressure) upon exposure of 311 nm UV light, which is abundant in lower troposphere. Infrared spectroscopy has been employed to probe the photo-oxidation products. Formic acid is identified as a very common end product in all the studies. Quantum yields of production of this acid and several other important photoproducts have been measured. Reaction mechanisms have also been proposed to explain formation of the identified photoproducts. Different peroxy radicals are proposed as vital reaction intermediates, and the proposal has been authenticated with the aid of electronic structure calculations as well as reaction modeling. Using a simplified atmospheric chemical model based analysis it has been inferred that under tropospheric condition, the amount of formic acid expected to be produced by photo-oxidation process is in the range of several parts per trillion volumes (pptv). Therefore, we argue that this process might contribute significantly in the natural abundances of atmospheric formic acid.

1. Introduction

Photochemistry of volatile organic compounds (VOCs) plays an essential role in determining the chemical composition of the Earth's troposphere. These VOCs are emitted into the atmosphere as pollutants in significantly large amount, ~709 Tg/year, where fossil fuels alone contribute ~214 Tg to this total annual budget. Therefore, complete understanding of the ultimate fate of these pollutants in the environment is extremely important from the viewpoint of air quality control and environmental safety. The VOCs are removed from the atmosphere either by physical removal mechanism viz. dry deposition, wet deposition or by chemical transformation into other species. Under

atmospheric condition, the VOCs are oxidized by reactive species like hydroxyl radicals (HO), chlorine atoms (Cl), nitrate radicals (NO₃), ozone (O₃) etc. which are commonly known as atmospheric cleaning agents. However, the major chemical reaction involving the VOCs is found to be the photochemical degradation upon direct absorption of the ultraviolet (UV) radiation of sunlight.

Carbonyl compounds, particularly the linear and cyclic ketones, constitute a large part of the total VOCs present in the atmosphere. Moreover, these groups of compounds mostly absorb in the UV region that is prevalent in the troposphere.

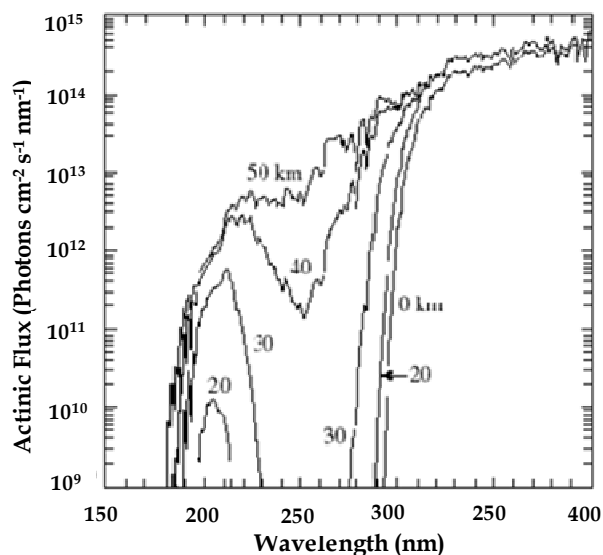


Figure 1: Solar actinic flux (for solar zenith angle of 30°) at different altitudes as a function of wavelengths (reported by W. B. DeMore et al. *Chemical Kinetics and Photochemical Data for Use in Stratospheric Modeling*. JPL Publication 97-4. Pasadena, Calif.: Jet Propulsion Lab, 1997.).

As shown in Figure 1, the intensity versus wavelength plots of solar UV at different altitudes clearly shows that the light of wavelength greater than 290 nm dominates the troposphere. And most of the carbonyls have strong absorption in this region of solar spectrum. Therefore, photo-degradation of these compounds under atmospheric condition has gained much research interest in recent years. The photochemical channels for the carbonyl compounds have been elucidated in the last century by Prof. G. W. Norrish and other researchers. It has been observed that the primary step of photochemistry of carbonyls involves α -cleavage (R 1.1) in which one of the C-C bonds adjacent to carbonyl group breaks and free radicals are formed. This reaction is also known as Norrish type-1 reaction.



The other important photochemical reactions were shown to be the γ -hydrogen transfer (Norrish type-2 reaction), different photo-isomerizations and internal rearrangements.

Although the vapor phase photochemistry of many carbonyls has been probed experimentally over the last couple decades, those studies are incomplete in the sense that some of the photo-products remained undetected due to lack of advanced probing methods. For example, methanol and formaldehyde were previously identified as the major products in photo-dissociation of acetone in presence of oxygen. However, in 1960s, Osborne et al.[1] first reported that formic acid is also produced by the same photochemical process. This claim was immediately rejected by Pearson[2], and in a long run of experiments employing the same experimental conditions the author could not detect formic acid in spite of using the same spectroscopic probing method. In later years, several reports appeared in the literature on photo-oxidation of acetone but production of formic acid was never experimentally verified although Gardner et al.[3] stated that formic acid is an expected product.

Production of formic acid by the photo-oxidation of different VOCs has been found to be a major source of the total atmospheric abundance of this acid. However, the annual atmospheric budget of formic acid, ~100-120 Tg, has been estimated to be several times larger compared to the known sources. Recently it has been suggested by Millet et al.[4] that photo-oxidation of carbonyls could be a potential missing source of atmospheric formic acid, although no quantitative data were available in this regard. Formic acid being one of the largest contributors to the atmospheric acidity and responsible in controlling many vital atmospheric reactions, it is essential to identify all possible atmospheric sources of this species.

In this report, a brief review has been presented regarding the photochemistry of selected atmospherically abundant carbonyls

under tropospheric conditions, which has been investigated by our group very recently. In synthetic air, photochemical reactions are initiated by shining with UV light of wavelength 311 nm, which is abundant in the troposphere, and the following reactions are probed by using FTIR spectroscopy. It is found that in photo-oxidation of these carbonyls, particularly acetone, cyclohexanone and cyclopentanone, formic acid is a major and common product. Quantum yield of formation of this carboxylic acid along with other photoproducts have been measured by varying the experimental conditions. Mechanisms have been proposed to explain formation of the identified photo-products including formic acid.

2. Experimental Methods

Photo-oxidation of VOCs was carried out in a cylindrical quartz cell of length 18 cm and inner diameter 3 cm. Two flat KBr windows were fitted at the two open ends of the cell. For identification of the reaction products and also to monitor the progress of the reaction at definite time intervals after switching the UV lamps on, a commercial FTIR spectrometer (IFS 66S, Bruker Optics) was employed. The reaction cell was placed directly into the sample compartment of the FTIR spectrometer, and three similar UV-B lamps of emission maximum at 311 nm (Philips TL 01, 20 W) were installed around the reaction cell as light sources to carry out the photolysis. The cell was connected with a turbo-molecular vacuum pump (Pfeiffer Vacuum) backed by a dry diaphragm pump for evacuation of the cell. The pressure of the reaction cell and the sample pressure taken in a separate mixing chamber were monitored by a high-pressure capacitive diaphragm gauge (CMR 361, Pfeiffer Vacuum). The sample introduction into the cell from the reservoir was controlled using a Swagelok precision metering valve. The cell temperature

was mentioned at around 30°C at the time of experiments by a temperature sensor with accuracy $\pm 1^\circ\text{C}$.

The FTIR spectrometer Tensor 27 (Bruker Optics) used to record spectra has a resolution of 0.25 cm^{-1} . The software for spectral data acquisition, OPUS version 7.0, was provided by the manufacturer of the spectrometer (Bruker Optics), and the same software was used for the purpose of displaying the recorded spectra. The reproducibility of the results have checked several times.

Spectroscopic-grade VOC sample was purchased from different reputed chemical companies. Before use, the procured compound was degassed by means of several freeze-pump-thaw cycles. The purity of nitrogen and oxygen gases used was $\sim 99.99\%$. The VOC was mixed with synthetic air and carried out our photo-oxidation experiments.

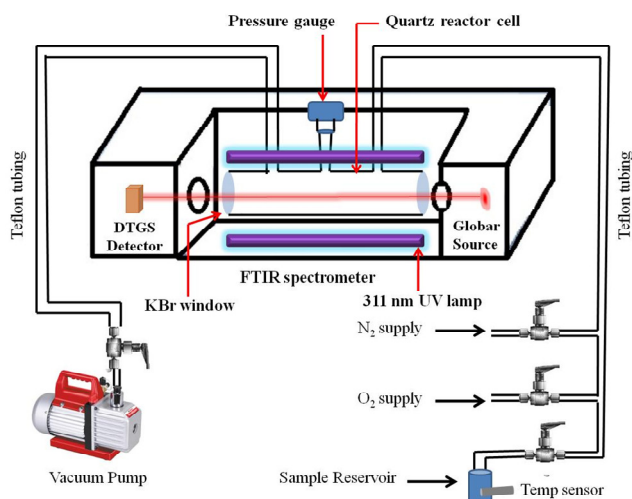


Figure 2: Schematic representation of experimental arrangement.

3. Photo-oxidation of acetone

Acetone is the smallest ketone and is one of the most abundant oxygenated hydrocarbons in the atmosphere. It has been found that $\sim 95\text{ Tg}$ of this VOC flows into the

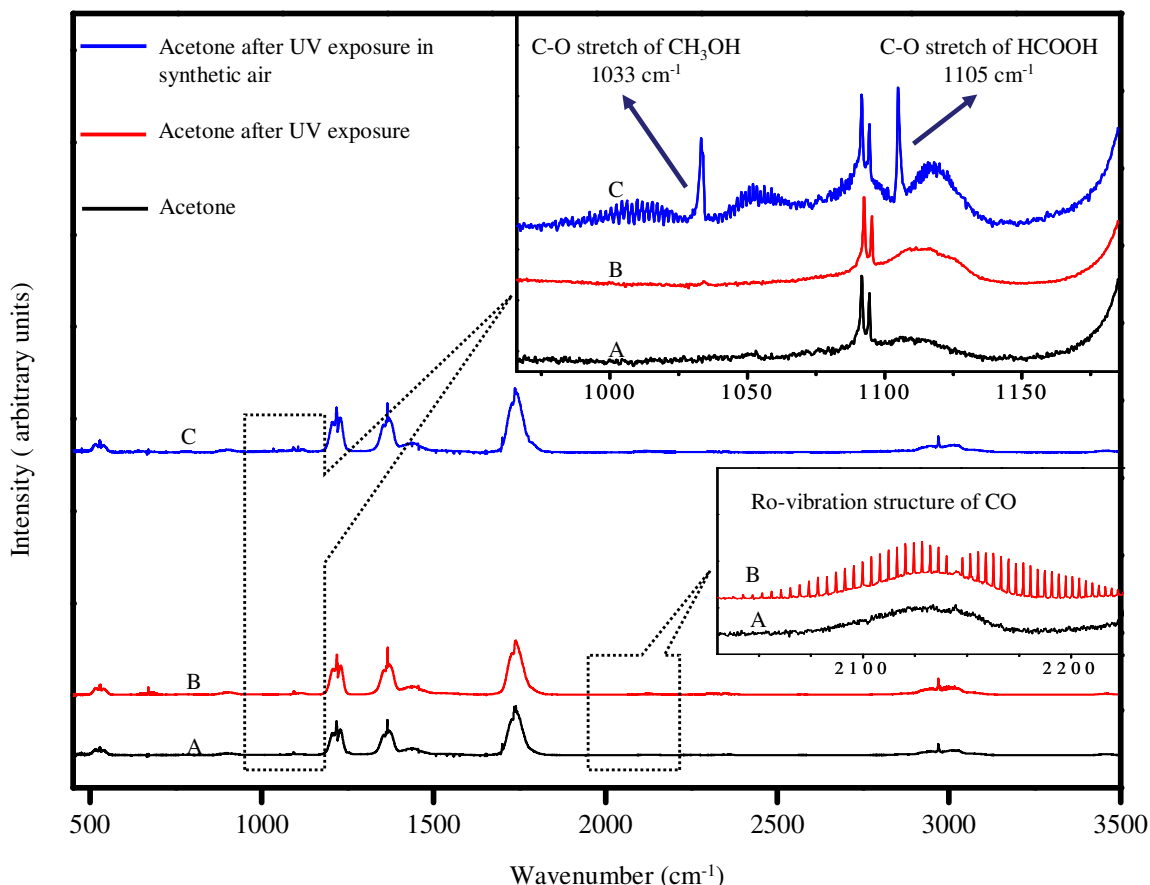


Figure 3: (A) FTIR spectra of acetone vapor diluted in N_2 at a total pressure of 300 mbar, (B) FTIR spectra recorded following UV photolysis (wavelength 311 nm) of the same reaction mixture for 180 min and (C) FTIR spectra of the photolyzed acetone in the synthetic air ($N_2:O_2 = 4:1$) gas mixture ($\lambda_{photo} = 311$ nm and exposure time 180 min). The insets display the rovibrational features of some photo-products.

atmosphere each year, and ~ 2 Tg of this budget is estimated to be contributed solely by human activities, e.g., industrial solvents and automobile exhaust. Now, the question is how this huge amount of acetone gets disintegrated under atmospheric condition. It was reported that a major portion $\sim 46\%$ of this total budget is degraded photochemically and $\sim 27\%$ is decomposed by reaction with OH radicals. We have investigated photo-dissociation of acetone under simulated atmospheric environment[5], i.e., acetone vapor was mixed with synthetic air ($N_2:O_2 = 4:1$) and the gas mixture was subjected to UV (311 nm) irradiation for 180 minutes. The progress of the photochemical reaction was monitored by recording FTIR spectra at a regular interval of time. A comparison of the

fingerprints segments of the FTIR spectra of acetone recorded before and after UV irradiation as well as in presence and in absence of synthetic air is shown in Figure 3. Upon light exposure, the most prominent signature of the reaction is found to be appearance of the typical rovibrational features of carbon monoxide (CO) with band centre ~ 2150 cm^{-1} . For the experiment performed in synthetic air (depicted in panel C), two new bands are observed around 1100 cm^{-1} . The band centred at 1105 cm^{-1} is identified as the C-O stretching fundamental of formic acid, while the other one at 1033 cm^{-1} is found to be the C-O stretching fundamental of methanol. These transitions along with the characteristic P, Q, and R branches are the unambiguous

signatures for production of formic acid and methanol. The rovibrational features around 2780 cm^{-1} corresponds to the aldehydic C-H stretching fundamental of formaldehyde. Carbon dioxide (CO_2) is also found to be a photo-oxidation product at this condition. The quantum yields of these photoproducts have been measured as displayed in Table 1.

Species	Quantum Yield
HCOOH	0.005
HCHO	0.0107
CH_3OH	0.017
CO	0.006

Table 1: The quantum yields of different photoproducts formed in 180 minutes UV exposure of 0.5 mbar of acetone diluted in synthetic air to 1bar total pressure.

For this purpose, the intensity of the photolysis light was measured by actinometric method where the quantum yield for CO production by UV photolysis at a wavelength similar to that reported by Herr et al.[6] was used as the reference data. The amount of reactant consumed or products formed has been estimated from FTIR spectra using corresponding absorption cross-section values (taken from the PNNL database) at specific probe wave numbers mentioned above.

To further elucidate the mechanism involved in photo-oxidation of acetone, we measured the variation of QY of all four major products with the time of UV irradiation (depicted in Figure 4). It is found that the QY of CO production remains unchanged during the first 60 minutes of irradiation, but those of CH_3OH , HCHO and HCOOH decrease slowly. Such a temporal behavior implies that the

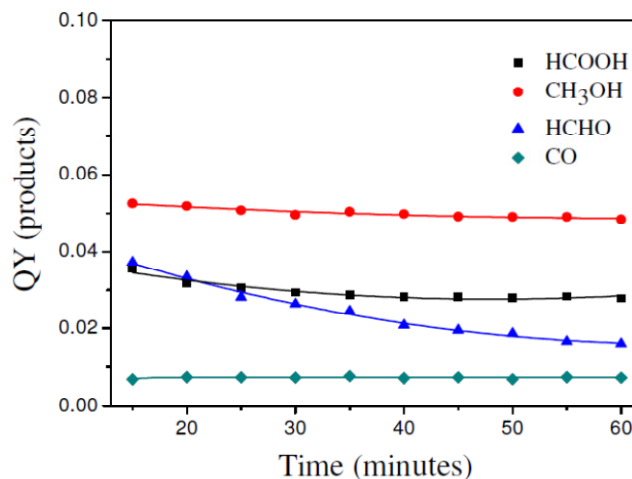


Figure 4: Variation of quantum yields (QY) of the major photoproducts with UV irradiation time.

process of photo-oxidation is complex and many primary and secondary reactions could be involved in the whole process of formic acid production. A complete list of all these reactions along with their respective rate parameters have been mentioned in Ref 5.

From the overall mechanism it appears that the formation of methyl (CH_3) and acetyl radical (CH_3CO) by α -cleavage of acetone is the initiation reaction step following absorption of a UV photon (311 nm). Since both the radicals have a strong affinity for oxygen, thus peroxyethyl (CH_3O_2) and peroxyacetyl (CH_3COO_2) radicals are formed which act as the precursors of methanol and formaldehyde. Under continuous UV exposure, formaldehyde is likely to undergo further dissociation and eventually led to formic acid production by several peroxy radical reactions. Methanol does not absorb this wavelength, but it can be further oxidized by HO_x radicals which can be generated under the reaction condition used in the present case. Based on this reaction mechanism, a reaction modeling has been performed using the computer program Acuchem, where all the above mentioned reaction channels and corresponding rate constants were supplied as input. As output,

this modeling provides the quantum yields and temporal profile with respect to different reactants and products. And the simulated results are found to be in good agreement with the experimental data. This unequivocally proves the reaction mechanism mentioned above.

A simple atmospheric reaction modeling has also been performed considering true atmospheric parameters to quantify the amount of formic acid that is expected to be produced in real atmosphere via this route of acetone photo-oxidation. Analysis reveals that although NO is known as a quencher of peroxy radicals which are the precursors of formic acid, but NO has a positive effect in production of formic acid under atmospheric condition. It has been estimated that ~ 1 pptv of formic acid is expected to be produced in real atmosphere from acetone photo-oxidation.

4. Photo-oxidation of other linear ketones

Along with acetone, several other linear ketones are also quite abundant in the troposphere. We have investigated photo-oxidation of three higher homologue of acetone viz. butanone, 2-pentanone and 3-pentanone. Figure 5 represents some selected parts of the FTIR spectrum of butanone diluted in O₂

before and after UV exposure. It is evident that similar to acetone in this case also CH₃OH, HCOOH and HCHO have been formed as major photo-oxidation products. Ethylene is produced as a minor photo-oxidation product. The same sets of products have been identified in case of photo-oxidation of 2-pentanone and 3-pentanone also. Yields of these products have been quantified and the results compared with that of acetone are depicted in Table 2.

Precursor compound	Partial pressure of precursor (mbar)	Concentration of the products formed (10 ¹⁵ molecules cm ⁻³)			
		HCOOH	CH ₃ OH	HCHO	CO
Butanone	2.8	2.27	5.11	0.68	4.20
2-pentanone	1.6	3.02	6.59	0.79	5.00
3-pentanone	2.4	3.27	5.91	0.80	5.17
acetone	4.5	0.96	2.73	0.35	2.61

Table 2: Concentration of different photo-oxidation products of butanone, 2-pentanone, 3-pentanone and acetone for 5 hours UV irradiation. In these experiments sample compounds are diluted in synthetic air up to total pressure of 1 bar.

It is evident that for all the higher chain linear ketones, yield of formic acid production is greater than that of acetone. This is primarily because of the fact that the photodissociation efficiency of acetone is much less compared to that of other ketones and this is evident from

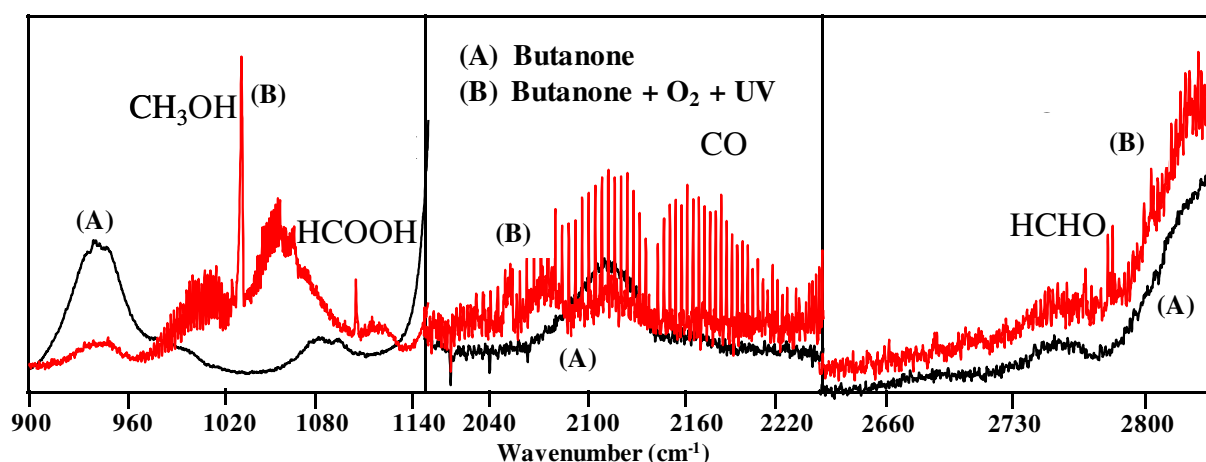


Figure 5: FTIR spectral identification of the photo-oxidation products of butanone.

the CO production yield. This comparative yield data suggest that similar to acetone, photo-oxidation of other linear ketones are also likely to contribute a major amount of formic acid production in the atmosphere.

5. Photo-oxidation of cyclic ketones

Cyclic ketones are the group of carbonyls that are important both from the basic chemistry and atmospheric chemistry point of views. Anthropogenic activities are the major atmospheric sources of the simple cyclic ketones e.g. cyclohexanone (CH), cyclopentanone (CP) and cyclobutanone (CB). The basic photochemistry and photodissociation dynamics of these cyclic ketones have been extensively investigated over the past couple of decades. However, no reports on photo-oxidation of these compounds under simulated atmospheric condition are available in the literature.

5A. Cyclohexanone (CH)

Cyclohexanone is emitted in the atmosphere as industrial wastes, mainly from the polymer industry. Although the overall atmospheric abundance of this compound is not well documented, some regional studies reveal that the atmospheric concentration of this species is nearly similar to that of acetone. A number of recent reports also showed that CH blended with synthetic Fischer-Tropsch

fuel generates less amount of soot on combustion, i.e., it has been recognized as a second generation fuel. From this perspective, the oxidative fate of this compound under tropospheric condition is an important issue.

Figure 6 depicts the major photo-oxidation products formed by photolysis of CH diluted in synthetic air as identified by using FTIR as the probing method. Formaldehyde (HCHO) has been characterized by its C-H stretching fundamentals bands around 2780 cm^{-1} and formic acid is probed at 1105 cm^{-1} corresponding to its C-O (single bond) stretching fundamental band. The infrared band at 949 cm^{-1} is assigned as the out-of-plane twisting C-H fundamental of ethylene (C_2H_4).

Similar to the case of acetone, here also, the QY for different photo-oxidation products have been measured and the results are displayed in Table 3. Thus, if photo-oxidation is carried out for duration of 360 minutes with our apparatus, it is estimated that CH is converted to 39.2% of CO, 10.7% of HCOOH, 16.5% of C_2H_4 and 1.2% of HCHO. The rest is likely to be converted to CO_2 , which we could not measure quantitatively with sufficient precision.

As described in details in Ref 7, the temporal behavior of accumulation of different photo-oxidation products within the reactor cell with duration of UV exposure was also monitored

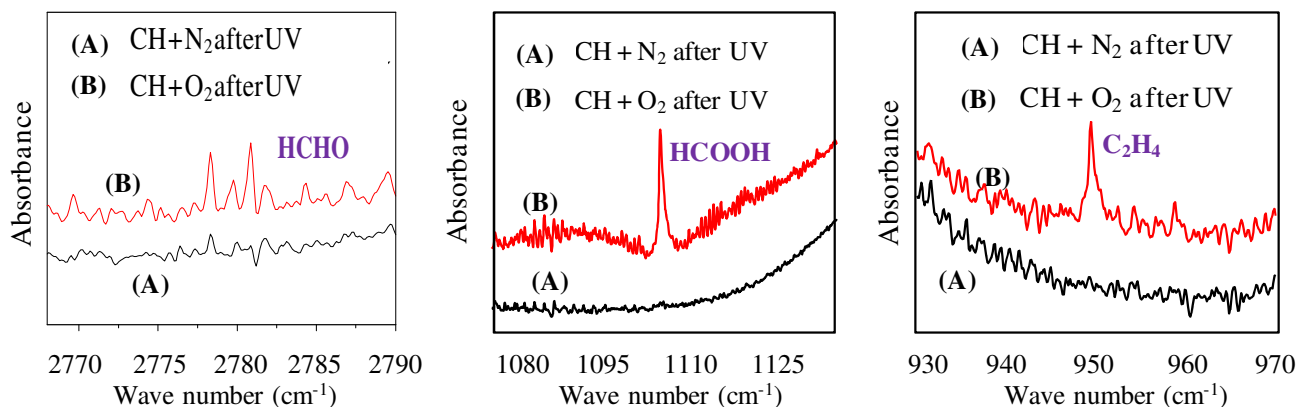


Figure 6: IR spectral features of different photo-oxidation products of CH.

Species	Absolute yield (molecules cm^{-3})	Quantum yield
HCHO	$3.83 \pm 2.0 \times 10^{14}$	0.0028 ± 0.002
C_2H_4	$5.34 \pm 0.10 \times 10^{15}$	0.0395 ± 0.001
HCOOH	$3.46 \pm 0.25 \times 10^{15}$	0.0256 ± 0.002
CO	$1.27 \pm 0.01 \times 10^{16}$	0.0940 ± 0.001

Table 3: Quantum yields and absolute yields of photo-oxidation products and CO upon UV exposure of CH for 6 hours. The measurements were carried out at 1 bar of total pressure in the reactor, where concentration of CH was kept at $9.19 \pm 0.1 \times 10^{16}$ molecules cm^{-3} . Intensity of light was maintained at 6.25×10^{12} quanta $\text{cm}^{-3} \text{s}^{-1}$.

using the same probing method. And a mechanism has been proposed for photo-oxidation of CH as shown in Figure 7.

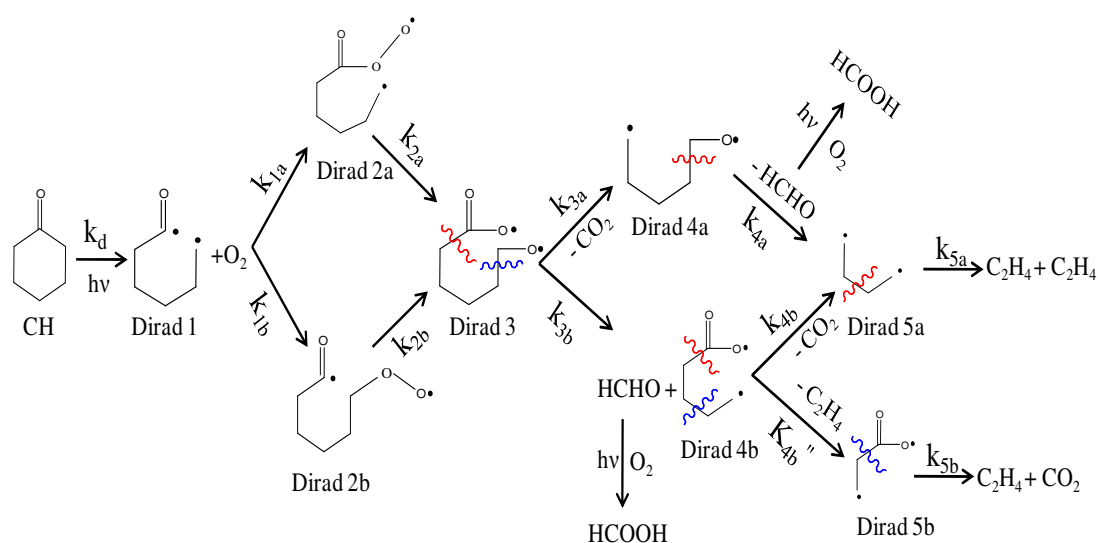


Figure 7: Suggested mechanism and definition of rate constants for different steps of CH photo-oxidation.

According to this mechanism, the Dirad 1 produced via α -cleavage process binds with oxygen at two possible sites to produce Dirad 2a and Dirad 2b, which upon further intramolecular rearrangement generate Dirad 3. Dirad 3 falls apart to Dirad 4a and Dirad 4b in two parallel channels via eliminations of CO_2 and formaldehyde, respectively.

Elimination of formaldehyde from Dirad 4a results in formation of Dirad 5a, which dissociates further into ethylene. Dirad 4b dissociates to produce ethylene and CO_2 via two sequential pathways that involve two intermediates, Dirad 5a and Dirad 5b, respectively. Formic acid is produced from formaldehyde by means of further photo-oxidation. The activation energy barriers for different reaction steps of the above mentioned mechanism have also been calculated using electronic structure theory method at DFT/B3LYP/6-311++G** level, and the results are summarized in Ref 7 and 8. The reaction mechanism has been further validated by performing reaction modeling which provides the calculated QYs for different photo-oxidation products and the simulated results experimental values.

5B. Cyclopentanone (CP)

However, the atmospheric abundance of CP is not well known but wastes from thermal power plants and coal industry are found to be the main sources of this compound in the atmosphere. Similar to CH, photo-oxidation of CP under atmospheric condition is

found to produce HCHO and HCOOH and in this case propene (C_3H_6) is formed as the hydrocarbon product. The QYs of these photo-products are presented in Table 4. In case of CP, the overall dissociation quantum yield has been estimated as 0.25 ± 0.03 .

Species	Absolute yield (molecules cm^{-3})	Quantum yield
HCHO	$4.15 \pm 2.0 \times 10^{14}$	0.0031 ± 0.002
HCOOH	$3.53 \pm 0.2 \times 10^{15}$	0.0261 ± 0.001
CO	$9.40 \pm 0.02 \times 10^{15}$	0.0696 ± 0.001

Table 4: Quantum yields and absolute yields of photo-oxidation products and CO upon UV exposure of CP for 6 hours. Initial concentration of CP was kept at $8.97 \pm 0.1 \times 10^{16}$ molecules cm^{-3} and other conditions were maintained similar to those for CH.

The mechanism for photo-oxidation of CP is proposed to be quite similar to that of CH where the diradical formation by α -cleavage has been considered to be the initial step. Interestingly, in this case also formic acid has been found to be one major photo-oxidation product.

5C. Cyclobutanone (CB)

Although, the atmospheric abundance of CB is not exactly known, but photo-oxidation of this compound under simulated atmospheric condition is found to provide some interesting results. In this case, the major photo-oxidation products are found to be formaldehyde, formic acid, along with that acetic acid is also observed as one of the products. The infrared spectral features for these photo-products are shown in Figure 8. The characteristic features of HCHO and HCOOH in mid-infrared have already been mentioned previously. Here, acetic acid (CH_3COOH) has been probed at

1183 cm^{-1} which corresponds to its C-O stretching fundamental band.

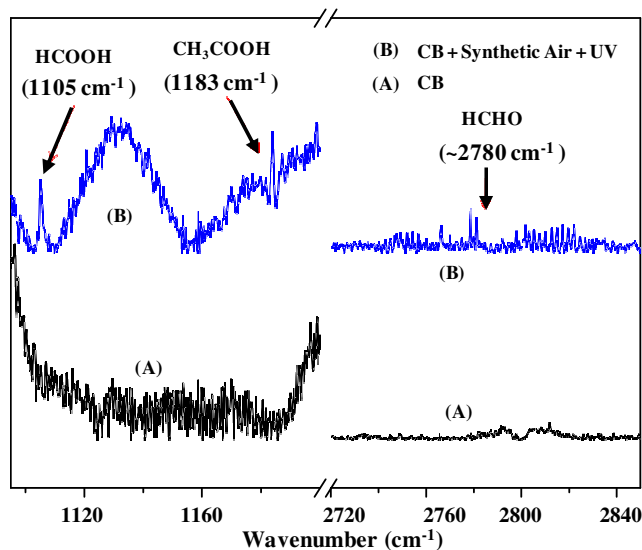


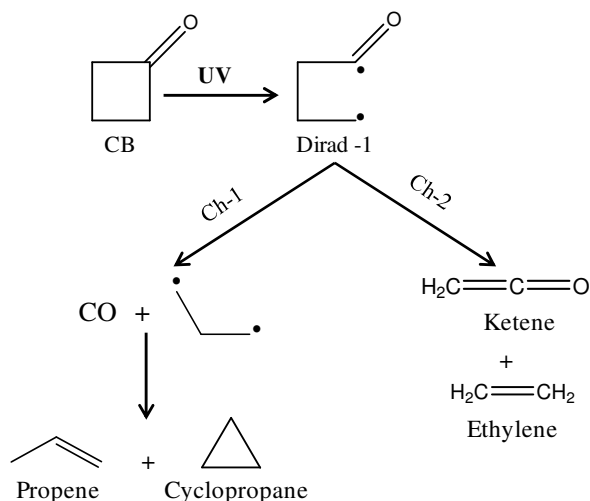
Figure 8: Infrared spectral identification of the photo-oxidation products of cyclobutanone.

The quantum yield values of these photo products for 5 hours of UV irradiation at 1 atm total pressure are listed in Table 5 below.

Species	Quantum yield
HCHO	0.0031 ± 0.002
HCOOH	0.0261 ± 0.001
CH_3COOH	0.0160 ± 0.004
CO	0.0696 ± 0.001

Table 5: Quantum yields and absolute yields of photo-oxidation products and CO upon UV exposure of CB for 5 hours.

It is seen from above table that the QYs for acidic products obtained from CB photo-oxidation are nearly the same as that for the other carbonyls. The proposed mechanism can be summarized as follows. It was previously reported that photolysis of CB produces propene, cyclopropane, ketene and ethylene following the reaction mechanism depicted in Scheme 1.



Scheme 1: Probable photochemical channels of cyclobutanone.

Ketene produced in the photodissociation of CB is likely to be the precursor of the photo-oxidation products. Recently, Vaida and co-workers have reported that ketene is hydrolyzed to produce acetic acid in presence of trace amount of water.



In presence of UV irradiation, ketene can further photo-dissociate to produce carbene (:CH₂). In presence of O₂, it is known that carbene produces HCHO. Whereby HCOOH is formed via photo-oxidation HCHO following the usual mechanism.



Moreover, photo-oxidation of CB has also been found to contribute to atmospheric acid production.

6. Conclusions

This report presents an overview of the vapor phase photo-oxidation of some atmospherically abundant carbonyl compounds under simulated tropospheric condition. Some linear (acetone, butanone, 2-pentanone and 3-pentanone) and cyclic (cyclohexanone, cyclopentanone and cyclobutanone) ketones

have been selected as the target systems. The sample vapor has been diluted with synthetic air (N₂:O₂ = 4:1) and the gas mixture was subjected to UV radiation of 311 nm wavelength which is abundant in the troposphere. Use of FTIR spectroscopy as the probing method reveals that formic acid is a major photo-oxidation product for all of these carbonyl compounds. The probable reaction mechanism in support of the formic acid formation is found to involve different peroxy radical reactions where the initial step has been considered to be the α-cleavage of the carbonyl leading to formation of a diradical. Quantum yields of different photoproducts have been measured in different experimental conditions. The proposed reaction mechanisms have been further authenticated by performing reaction modeling simulation study which yielded similar quantum yield values as obtained from the experiments. Photo-oxidation of higher chain linear ketones has been found to produce formic acid with higher yield as compared to that of acetone. Thus, these compounds are expected to contribute significantly in atmospheric formic acid production. Similar to acetone, the cyclic ketone CH has been found to contribute ~1 pptv of formic acid to the atmospheric production. Interestingly, for CB, acetic acid is also found to be one of the photo-oxidation products and it has been proposed that the acetic acid is formed by hydrolysis of ketene which has been identified as a photo-product of CB.

Acknowledgements

We acknowledge the co-authors of our published papers cited in the references. All the research work has been done under supervision of Prof. Tapas Chakraborty, Department of Physical Chemistry, IACS. We are sincerely grateful to Prof. Chakraborty for his encouragement and support.

7. References

1. Osborne, A. D.; Pitts, J. N.; Fowler, S. L. Investigation of the Photooxidation of Acetone at 3130 Å Using Infrared Analysis. *J. Phys. Chem.* 1961, **65**, 1622–1625.
2. Pearson, G. S. The Photooxidation of Acetone. *J. Phys. Chem.* 1963, **67**, 1686–1692.
3. Gardner, E. P.; Wijayaratne, R. D.; Calvert, J. G. Primary Quantum Yields of Photodecomposition of Acetone in Air under Tropospheric Conditions. *J. Phys. Chem.* 1984, **88**, 5069–5076.
4. Millet, D.B., Natural atmospheric acidity. *Nat. Geosci.* 2012, **5**, 8e9.
5. Chattopadhyay, A.; Chatterjee, P.; Chakraborty, T. Photo-oxidation of Acetone to Formic acid in Synthetic Air and Its Atmospheric Implication. *J. Phys. Chem. A* 2015, **119**, 8146-8155.
6. Herr, D. S.; Noyes, W. A. Photochemical Studies. XXXI. A Systematic Study of the Near Ultraviolet Photochemical Decomposition of Acetone. *J. Am. Chem. Soc.* 1940, **62**, 2052–2059.
7. Chattopadhyay, A.; Mondal, K.; Samanta, M.; Chakraborty, T. Photooxidation of Cyclohexanone in Simulated Atmosphere: A Potential Source of Atmospheric Formic Acid. *Atmos. Environ.* 2017, **157**, 125-134.
8. Chattopadhyay, A.; Mondal, K.; Samanta, M.; Chakraborty, T. Photoisomerization of a Small Cyclic Ketone in the Vapor Phase. *Chem. Phys. Lett.* 2017, **675**, 104-110.



Dr. Aparajeo Chattopadhyay obtained his M. Sc. degree in Chemistry from University of Calcutta, in 2011. He did his Ph.D. research under supervision of Prof. T. Chakraborty at IACS, Kolkata and got his degree in 2018. Presently he is working as a postdoctoral fellow under Prof. James Burkholder at NOAA ESRL Chemical Sciences Division. His research interest is gas phase photochemistry relevant to atmospheric processes.



Mr. Koushik Mondal obtained his M. Sc. degree in Chemistry from Banaras Hindu University in 2015. Presently, he is doing Ph.D. under supervision of Prof. T. Chakraborty in Indian Association for the Cultivation of Science (2015-continued). His research interest is investigation of atmospheric fate of some long chain VOCs, specially ketones, through FTIR spectroscopy.



Ms. Piyali Chatterjee obtained her M. Sc. degree in Chemistry from Jadavpur University, Kolkata in 2012. She joined as a Ph.D. scholar under the supervision of Prof. T. Chakraborty in Indian Association for the Cultivation of Science, Kolkata, India as a DST INSPIRE fellow. Her research interest is mass spectrometric investigation of photochemical processes in molecules and small molecular clusters, particularly those involving proton or hydrogen transfers.

Role of volatile organic air pollutants in lower atmospheric chemistry, their sources and health concerns

Dipanjali Majumdar*

**National Environmental Engineering research Institute, Kolkata Zonal Centre
i-8, Sector C, EKDP, Eastern Metropolitan Bypass, Kolkata 700107
E mail: ds_majumdar@neeri.res.in, dipanjalisom@gmail.com*

Abstract

Volatile organic compounds (VOCs) are part of the large hydrocarbon family, a vast array of aliphatic, aromatic hydrocarbons, their halogenated derivatives, alcohols, ketones and aldehydes. VOCs have a property of conversion into vapour or gas without any chemical change. They are highly reactive hydrocarbons and participate in atmospheric photochemical reactions. Some of them have negligible photochemical activity; however, they play an important role as heat trapping gases in the atmosphere. VOC of both primary and secondary origin in ambient air have immense importance as they have direct as well as indirect effects on climate change, ecology and human health.

Role of VOCs in lower atmospheric chemistry

VOCs has two fold impact in tropospheric chemistry. In presence of oxides of nitrogen and sunlight, VOCs form ozone, one of the most important short lived climate forcers (SLCF). Also, photochemical reactions of VOCs in presence oxide of nitrogen (NO_x) and ozone give rise to secondary aerosol (SOA) which are another environmental and health concern.

The oxidation of complex organic molecules leads to the fragmentation, production of a range of reactive free radicals and more stable smaller molecules such as carbonyls. In the atmosphere, aldehydes are formed in situ as oxidation products of many hydrocarbons. In synergy, a fraction of the aldehydes is rapidly removed by photolysis and by reaction with $\text{OH}\cdot$. The competition between photochemical formation and removal may result in a net production or a net loss of aldehydes. In one of our study (Dutta et. al., 2009), mixing ratios of 15 carbonyls and BTEX (benzene, toluene, ethyl benzene, xylenes) were measured for the first time in ambient air of Kolkata, India. The study was undertaken at three sites and their photochemical reactivity was evaluated. Day and night-time samples were collected on a weekly basis.

Formaldehyde was the most abundant carbonyl (mean concentration ranging between $14.07 \mu\text{gm}^{-3}$ to $26.12 \mu\text{gm}^{-3}$ over the three sites) followed by acetaldehyde ($7.60\text{--}18.67 \mu\text{gm}^{-3}$) and acetone ($4.43\text{--}10.34 \mu\text{gm}^{-3}$). Among the high molecular weight aldehydes, nonanal showed the highest concentration. Concentrations of the high molecular weight aldehydes were found to be much less than C1–C3 carbonyls but their contribution to local photochemistry might be important due to their faster reactions with the hydroxyl radical. Based on OH reactivity, concentrations were scaled to formaldehyde equivalents. The contribution of xylenes and high molecular weight carbonyls were significantly increased vis-à-vis their respective low molecular weight components. The contribution of C4–C10 aldehydes to the total $\text{OH}\cdot$ reactivity was 18.9% and that of xylenes was found to be 34.3%. It was found that the scaled concentration of NO_x and carbonyls was up by 3.84 and 1.25 times respectively but down by about 25% in the case of aromatics. This is because of the fact that among the aromatic hydrocarbons studied, only xylenes are more reactive than formaldehyde towards $\text{OH}\cdot$ and very high concentration of benzene and toluene in Kolkata pushed the scaled concentration of

total aromatics down. The overall contribution of aromatic hydrocarbons (scaled concentration) as an OH sink was found to be comparable to NO_2 and 1.9 times higher than the carbonyls. The formation of carbonyls from the hydrocarbons is thus a more dominant pathway than their loss process through reaction with $\text{OH}\cdot$ as reported earlier in the captive air experiments.

In Kolkata, the average ambient levels of carbonyls were quite high and were comparable to studies in other countries where gasohol is used as fuel. In general, average daytime carbonyl concentration was higher than at night, though not significantly different. The C1/C2 and C2/C3 ratios indicate that the principal source of carbonyls in Kolkata is anthropogenic. The level of BTEX in Kolkata was also very high compared to other cities mainly due to use of gasoline containing relatively higher concentrations of aromatics (3% benzene during the study period) coupled with high traffic density, insufficient road space and inadequate emission control strategy. Photochemical reactivity of BTEX towards OH was found to be twice as much as the carbonyls and the relatively higher concentration of formaldehyde is attributed to its formation from aromatic hydrocarbons by reaction with $\text{OH}\cdot$ in addition to the primary emissions. In the prevailing level of carbonyls and BTEX, they pose both cancer risk and non-cancer hazard for the general population as estimated at all three sites.

In another study (Talapatraet. et. al., 2014), ozone has been monitored hourly every month in residential, industrial, traffic intersections and petrol pumps in an urban area of Kolkata along with eight hourly non-oxygenated VOCs, carbonyls and NO_x . It is observed that high NO_2 levels coincide with low ozone values. NO_x being both precursor and titrant to ozone bears a negative correlation with ozone. Instantaneous photochemical ozone formation, $\text{P}(\text{O}_3)$; computed as the O_3 production rate as a function of NO_2 concentration; was found to be negative from 06 pm to 06 am during all seasons. This behaviour may occur because, in

addition to NO_2 , $\text{P}(\text{O}_3)$ is also dependent on VOC reactivity, sunlight, and radical precursors. Urban Airshed Model (UAM-V) has been used to simulate ozone for 24 hours on 14th of January 2008 in Kolkata urban Area. UAM-V uses an updated "Carbon-Bond IV" chemical mechanism to simulate the photochemical reactions between NO_x and ozone. Hourly values for the wind field and the vertical diffusivity are used to calculate transport and turbulent diffusion. Temperature, pressure, water vapour, cloud cover and precipitation for all grid points within the computational domain were provided. Modelling domain was selected as Kolkata Metropolitan Area that includes all the twelve monitoring locations was divided into 13×15 1km square grids. The input to the model was VOCs emission at twelve monitoring locations. Model-predicted hourly surface concentrations of Ozone were obtained for the entire simulation period at the grid cells corresponding to the monitoring locations. Apart from ozone formaldehyde, acetaldehyde, toluene and xylene were also predicted using the model. Results of predicted ground level ozone as well as other VOCs have been in agreement with observed concentrations. We concluded from the study that the urban area of Kolkata is characterised by low NO_x and high VOCs in general except in pockets of industrial activity and traffic intersections. Vehicular pollution and fossil fuel burning emissions from industries and non-point sources in Kolkata are major sources of air pollution. Ozone formation in urban areas of Kolkata is in general insensitive to changes of VOC concentrations. In industrial areas and close to traffic intersections ozone formations becomes insensitive to NO_x concentrations. Though observed ambient ozone levels are not very high, in order to accommodate urban development, policies on fuel use are required to avoid ozone episodes. For authorities to legislate suitable and efficient regulations and measures to counter the worsening air quality, information on the present levels of both primary and secondary pollutants is vital.

Ozone-forming potential of the oxygenated VOCs indicates that the altered characteristics of anthropogenic activities specific to the festival season also have a significant effect on the formation of secondary pollutants such as ozone (Majumdar et al., 2015). In case of the event of Diwali night, the VOCs sources were studied using principal component analysis. The effect of activities typical to the event of Diwali night, especially the extensive use of pyrotechnics, was clearly evident in the principal component analysis as the third major source, with 14.6% variance, on the night of the event, after vehicular emission and fossil fuel combustion. This study indicates that unregulated anthropogenic activities during the festival period in Kolkata metropolitan city contribute to a considerable extent towards elevated oxygenated and non-oxygenated volatile organic compounds in ambient air. Especially, the display of fireworks has marked impact on these organic pollutants. This study finding emphasizes that it is required to generate awareness among the community and also some regulations are required in place to minimizing these uncontrolled emissions and subsequent secondary pollutant formation.

Assessment of ozone-forming potential of the landfill due to NMVOC emission shows that carbonyl VOCs play a more important role than non-carbonyl VOCs for tropospheric ozone formation (Majumdar et al., 2014).

Short-lived climate pollutants (SLCPs)

These pollutants have short atmospheric lifetimes varying from days to a couple of decades. For slowing the rate of climate change over the next few decades and for protecting the vulnerable ecosystems and sensitive regions as well as the sensitive human population it is extremely important to reduce the SLCPs. These pollutants are more local/regional in nature than long-lived GHGs. Reducing SLCPs can lead to immediate climate benefits as the Earth's climate system responds quickly to reductions in these pollutants. Reducing SLCPs may be particularly beneficial for the protection of regions more sensitive to

climate change like the Arctic and the Himalayan glaciers. The so-called climate "tipping point" may be deferred by slowing the rate of warming which will also be abetted by reduction of SLCPs.

Apart from being a precursor to SLCP, i.e., ozone, a few VOCs have global warming potential of their own. In more than a yearlong study (Majumdar et al., 2011) of the city air in Kolkata, India at different seasons in three different sites, the seasonal mean benzene and toluene concentrations varied between 13.8–72.0 $\mu\text{g}/\text{m}^3$ and 21.0–83.2 $\mu\text{g}/\text{m}^3$ respectively along all the sites. The contribution of Kolkata metropolitan city towards global warming due to the environmental emission of BTEX has been estimated as 1.9×10^5 tons of carbon dioxide equivalent per year which is about 1.1% of yearly direct CO_2 emission the city.

Sources of tropospheric VOCs

There are a number of sources responsible for the emission of aromatic and oxygenated VOCs in airshed urban agglomerations of the world as also in Kolkata metropolitan city. A detailed level IV emission inventory as per the United States Environmental Protection Agency (USEPA) definition for evaporative VOC emissions in the metro cities of India namely Delhi, Mumbai, Chennai, and Kolkata was performed (Srivastava and Som 2008). The vehicular evaporative emissions are found to be the largest contributor to the total evaporative emissions of hydrocarbons followed by evaporative losses related to petrol loading and unloading activities. Besides vehicle-related activities, other major sources contributing to evaporative emissions of hydrocarbons are a surface coating, dry cleaning, graphical art applications, printing (newspaper and computer), and the use of consumer products. Various specific preventive measures were recommended for reducing the emissions.

EPA's CMB 8.2 is a widely used receptor model for source apportionment of particulate matter as well as VOCs. In one of our study (Majumdar (née Som) et al. 2009) the model was employed to find out the percentage

contribution of various sources in three receptor sites of Kolkata. The observation for target VOC species was undertaken for one year. Vehicle exhaust was found to be the dominant source contributor in all samples across all season but contribution never exceeded 50%. There are other important sources contributing significantly toward the VOC emission such as Coal combustion, attributed as the second largest source contributing 12-38%. Pesticide application and wood combustion were found also to be significant sources contributing 4-19% and 3-10% respectively. CALINE 4 dispersion model (in an inverse way) were used successively for estimating the contribution of the vehicular exhaust emission toward a few target pollutant (BTEX) level and then to calculate the total emission factor for the vehicles passing through the road adjacent to the three sites in a typical urban area. The category-wise vehicular emission factor was calculated using the measured vehicular composition during sampling. The high emission factor values in Kolkata may be due to the higher average age of the vehicular fleet along with poor maintenance, old technology, bad road condition, and a slow average vehicular speed. This procedure enabled us to estimate the real-time emission factor of vehicles from roadside measurement with sufficient reliability.

CMB 8.2 receptor model was also used in estimating the source contribution for aromatic and oxygenated VOCs in five city refuelling stations. The principal source of BTEX was vehicular exhaust coming from adjacent roads. Significant amounts of benzene were contributed by fugitive emission and refuelling. 1,3,5-Trimethylbenzene was mostly released during refuelling. Automobile painting and repair work contributed toluene, isomers of xylene, most of the acetone and some methylethylketone (MEK). Degreasing operations in the garages released the significant amount of MEK along with some toluene and 1,3,5-trimethylbenzene. Automobiles entering the refuelling stations emit exhausts, which contributed towards VOC emission levels. Among these, gasoline driven

vehicles not fitted with catalytic converters acted as significant source towards BTEX level, 1,3,5-trimethylbenzene and some oxygenated VOCs like formaldehyde, acetaldehyde and benzaldehyde.

Primary emission of Tropospheric VOCs can also originate from industrial sources (Srivastava and Som, 2007), Household solid fuel burning (Verma et al., 2018), Open dumping of Municipal solid wastes (Majumdar and Srivastava, 2012; Majumdar et al., 2014) and even from unregulated anthropogenic activity related to festival season such as display of pyro techniques (Majumdar et al. 2015).

VOCs in microenvironment

Volatile organic compounds (VOCs) are important indoor air pollutants due to their high volatility, mobility in the vapour phase and ability to penetrate the structure. Moreover, they are ubiquitous and numerous. USEPA Clean Air Act Amendments has identified 189 chemicals as hazardous air pollutants and nearly 100 of them are VOCs.

In one of our studies (Majumdar et al., 2012) VOCs were measured in indoor and outdoor air at 80 randomly selected public and private office buildings and residences representing middle and high income group in across the urban areas of Mumbai and Kolkata. Forty VOCs were detected indoors in Mumbai and forty four in Kolkata. Nearly one fourth of the VOCs identified are classified as HAPs. Fourteen VOCs were found both in Mumbai and Kolkata indoors. In Mumbai, fifteen VOCs were found in all the sites studied and ten VOCs were found in all the sites in Kolkata. Indoor total VOC concentrations ranged from 0.901 $\mu\text{g}/\text{m}^3$ to 4477 $\mu\text{g}/\text{m}^3$.

The prevailing level of BTEX in urban residences studied in Kolkata was found to be quite high (Majumdar (née Som) et al. 2012). The indoor level was significantly dependent on the type of fuel used and the extent of ventilation but not due to the location of the residence or kitchen placement inside the residences. The average indoor to outdoor concentration ratios for BTEX > 1 indicated the

presence of indoor sources along with infiltration of outdoor air.

Commuter's exposure was also studied in that passenger cars in Kolkata (Som et. al., 2007). Gasoline driven passenger cars without catalytic converters have higher level of BTEX, inside and immediate outside the car, than vehicles with catalytic converters. In-vehicle BTEX level also reduces when benzene content in petrol reduces from 3% to >1%. The study gives a very good real time account of reducing the effect of pollutant emission on imposing of control options.

VOCs and health concerns

Health risk of exposure to VOCs, even at lower levels are well established and are reported to affect liver, kidney, hematopoietic system, central nervous system, reproductive system, respiratory and cardiovascular system and also have skin and allergic effects, genotoxic and carcinogenic effects. In particular, benzene has been classified as a confirmed human carcinogen (A1) by American Conference on Governmental Industrial Hygienists (ACGIH), and International Agency for Research on Cancer (IARC). We deduced a derivation for estimation of body burden from urinary metabolite concentration using PBPK model (Majumdar et. al., 2015). Estimation of the internal dose or body burden of benzene in the human subject has been made for the first time by the measurement of t,t-MA as a urinary metabolite using physiologically based pharmacokinetic (PBPK) model as a tool. The weight adjusted total body burden of benzene was estimated to be 17.6, 11.1 and 5.0 $\mu\text{g kg}^{-1}$ of body weight for petrol pump workers, drivers and the environmentally exposed control group, respectively using this method. We computed the carcinogenic risk using both the estimated internal benzene body burden and external exposure values using a conventional method. Our study result shows that internal dose or body burden is not proportional to the level of exposure rather have a non-linear relationship. At a higher exposure level such as for occupational

exposure of petrol pump workers and drivers, the conventionally estimated risk is higher than risk estimated from internal body burden. Likewise, for environmental exposure, the conventional risk estimation predict lower level than estimated in our study. This emphasizes the importance of body burden and to consider it as a key parameter while estimating health risk at the varying level of exposure.

Estimation of cancer risk from selected hazardous pollutants among studied VOCs were performed in various set up such as in ambient (Majumdar et. al., 2011), Residential indoor (Majumdar et. al, 2012), occupational exposure for car drivers and petrol pump attendants (Majumdar (nee Som) 2008; Majumdar et al., 2015), dumpsite workers of Dhapa in Kolkata (Majumdar et. al., 2012) and Deonar & Malad in Mumbai (Majumdar and Srivastava 2012). It was found that in every case the estimated carcinogenic risk is appreciably higher than the acceptable risk of one in a million.

References:

- Majumdar (née Som) D., Mukherjee A. K. and Sen S. 2009. Apportionment of sources to determine vehicular emission factors of BTEX in Kolkata, India. *Water Air and Soil Pollution*. 201:379-388.
- Majumdar (née Som) D., Dutta C., Mukherjee A. K. and Sen S.. 2008. Source apportionment of VOCs at the petrol pumps in Kolkata, India; their occupational exposure to the workers and assessment of associated health risk. *Transportation Research Part D*, 13 (2008) 524-530.
- Majumdar (nee' Som), D., Mukherjee A. K., Mukhopadhyaya K. and Sen S. 2012. Variability of BTEX in the residential indoor air of Kolkata Metropolitan City. *Indoor and Built Environment*. 2012; 21; 3:374-380.
- Majumdar (nee' Som), D., Srivastava A., 2010. Emission Inventory of evaporative emissions of VOCs in Four metro cities In India. *Environmental Monitoring and assessment*. 160(1),

Page 315.

Majumdar (nee' Som) D., Mukherjee A. K. and Sen S. 2011, BTEX in ambient air of a metropolitan city. *Journal of environmental protection.*, 2, 11-20.

Majumdar D, Ray S, Chakraborty S, Rao PS, Akolkar AB, Chowdhury M, Srivastava A. 2014. Emission, speciation, and evaluation of impacts of non-methane volatile organic compounds from open dump site. *Journal of the Air & Waste Management Association* 64 (7), 834-845.

Majumdar D. and Srivastava A. 2012. Volatile Organic Compound Emissions from Municipal Solid Waste Disposal Sites: A Case Study of Mumbai, India *Journal of the Air & Waste Management Association* (2012). 62:4, 398-407.

Majumdar D., Chakraborti R. & Srivastava A. 2012. Indoor air quality in Offices and residences in urban areas of India-Mumbai & Kolkata. *Research journal of Chemistry and environment* 16(3); 74-78.

Majumdar D., Dutta C., Sen S. 2016. Inhalation exposure or body burden? Better way of estimating risk - an application of PBPK model. *Environmental Toxicology and Pharmacology.* 41, 54-61.

Majumdar D., Rao P. S., Chakraborty B. D., Srivastava A. 2015. Effects of unregulated anthropogenic activities on mixing ratios of volatile organic air pollutants-A case study. *Journal of the Air & Waste Management Association.* 65(9): 1094-1103.

Som D., Dutta C., Chatterjee A., Mallick D., Jana T. K., Sen S. 2007. Studies on commuters' exposure to BTEX in passenger cars in Kolkata, India. *Science of the Total Environment*; 372 (2007) 426-432.

Srivastava Anjali and Som Dipanjali. 2007. Hazardous Air Pollutants in industrial area of Mumbai-India. *Chemosphere*, 69(3); (2007), 458-468.

Talapatra A., Majumdar D. and Srivastava A. 2014 Distribution of ozone over urban Kolkata: observed vs UAM-V prediction. *Journal of Ozone Science and Engineering.* 36(2); 181-190.

Verma M., Pervez S., Majumdar D., Chakraborty

R. & Pervez Y. F. 2018 Emission estimation of aromatic and halogenated VOCs from household solid fuel burning practices. *International Journal of Environmental Science and Technology.* Accepted (online first August 2018).



Dr. (Mrs.) Dipanjali Majumdar is an eminent scientist at CSIR-National Environmental Engineering Research Institute. Her research interest mainly includes analytical chemistry, air pollution and volatile organic compounds. She is serving as a guest lecturer in Department of Chemistry, University of Calcutta, since 2013. She is also member of different Environmental Organizations.

Developing a dual channel receptor for Cu²⁺ and F⁻ by structural modification: a comparative review

Arghyadeep Bhattacharyya, Subhash Chandra Makhil, Subhajit Saha and Nikhil Guchhait*

Department of Chemistry, University of Calcutta, 92, A.P.C. Road, Kolkata-700009, India

Email: nguchhait@yahoo.com

Abstract

In the current review article, we focused on how gradual structural modification resulted in an efficient dual channel receptor for Cu²⁺ and F⁻ ions. We discussed three compounds, namely (E)-BIS-N¹-((1H-pyrrol-2-yl) methylene)-pyridine-2, 6-carbohydrazide (**1**), (12E, 13E)-2-((naphthalen-1-yl) methylene)-1-(1-(2-hydroxynaphthalen-6-yl) ethylidene) hydrazine (**AH**) and 1-[(2-Hydroxy-1, 2-diphenyl-ethyl)-hydrazonomethyl]-naphthalen-2-ol (**2**) respectively. Compound **1** acts as a colorimetric Cu²⁺ sensor. **AH** serves as an F⁻ sensor by displaying a sharp color change from yellow to orange. Finally, compound **2** serves as a fluorogenic sensor for Cu²⁺ and a chromogenic sensor for F⁻. The rationale behind the modification and its consequences shall be discussed in the current article.

1. Introduction

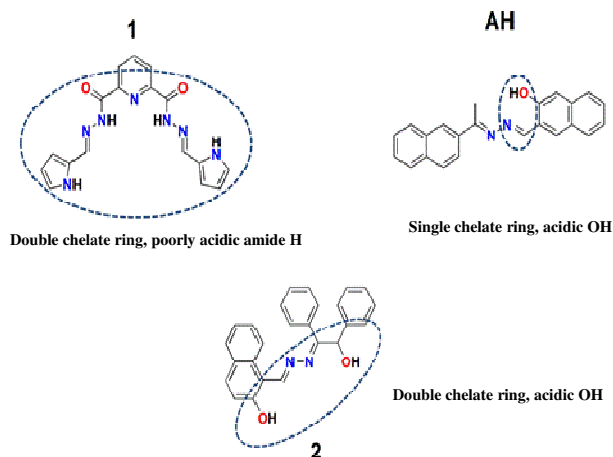
Complexes derived from transition metals have always drawn attention to the chemist fraternity owing to their manifold properties: pharmaceutical, magnetic and electrical properties to name a few.¹ The biological catalysts in the form of enzymes have transition metals in their active centre² and thus the indispensability of transition metals in sustenance of life processes can be envisaged. However, this very important class of metals also acts as one of the major pollutants present. Among the transition metals, copper stands out due to its 'omnipresence' in every organism from crustaceans to mammals. Being the third most abundant metal after Iron and Zinc, Copper is responsible for proper functioning of the human body due to its presence in various important enzymes such as amine oxidases, ceruloplasmin, Hephaestin, Lysyl oxidase and Superoxide dismutase (along with zinc)³ and catalyzes the formation of hemoglobin, although it is not a part of hemoglobin. On the other hand, a slight excess in the intake of copper turns out to be detrimental for the living body. Free copper ions in a live cell catalyze the formation of reactive oxygen species (ROS) that can damage lipids, nucleic acids, and proteins.⁴ Years of extensive research has hinted at the fact that cellular toxicity of Cu²⁺ is responsible for Alzheimer's

disease⁵, Indian childhood cirrhosis (ICC)⁶, prion disease⁷ and Menkes and Wilson diseases.^{8,9} The limit of copper uptake is set at ~30 μM by the World Health Organization (WHO).

Among the various anions in the environment as well as biological systems, the halogen family plays the perfect anionic analogue to the transition metals in terms of importance and utility, so much so that their role as pollutants is by no means lesser. The importance of fluoride in particular far exceeds its members in the halogen family due to its role in the treatment of dental caries¹⁰ and preventing osteoporosis.^{11,12} Due to its quick absorption and slow excretion from the body, an excess of fluoride opens up an array of pathological conditions, fluorosis^{13,14} being the most deadly, followed by urolithiasis and osteosarcoma.¹⁵ Thus, there is need for cheap, easy to handle and selective sensors for recognition of Cu²⁺ and F⁻. Although there are various literature reports for selective, sensitive detection of Cu²⁺ and F⁻ separately by conventional methods such as colorimetry and fluorimetry¹⁶⁻¹⁹, reports of simultaneous detection conveniently are somewhat less known. Furthermore, detection through the same response mechanism, say a color change²⁰ somewhat reduces the tidiness

involved with recognizing the aforesaid analytes when they are present together.

At this juncture, our group engaged in designing a probe that would be able to detect Cu^{2+} and F^- simultaneously. In this endeavor, we designed probes from very cheap starting materials which looked very promising theoretically. However, the goal of a dual sensor was not achieved. We started with (E)-BIS-N'-((1H-pyrrol-2-yl) methylene)-pyridine-2, 6-carbohydrazide (**1**) (Scheme 1). **1** constituted of multiple N, O donors which are known to show affinity towards Cu^{2+} as well as amide protons, which are expected to undergo H-bonding with basic anion like F^- .²¹ However, **1** showed only colorimetric response towards Cu^{2+} by showing a sharp color change.²² Furthermore, no fluorogenic detection was observed. Followed by **1**, we designed compound (12E, 13E)-2-((naphthalen-1-yl) methylene)-1-(1-(2-hydroxynaphthalen-6-yl) ethylidene) hydrazine (AH), adoublenaphthalene hydrazine derivative (Scheme 1). Since naphthalene containing compounds were observed to be strong fluorogenic sensors for Cu^{2+} ,¹⁶ it was expected that AH would behave as a fluorogenic sensor for Cu^{2+} . Apart from that, AH was also equipped with a phenolic -OH moiety, thereby opening up the possibility of H-bonding mediated sensing of anion(s). However, this time also, our expectations were not fulfilled as AH showed exclusive colorimetric detection of F^- with no selectivity towards Cu^{2+} .²³ Finally, we synthesized 1-[(2-Hydroxy-1, 2-diphenyl-ethyl)-hydrazonomethyl]-naphthalen-2-ol (**2**), a naphthalene benzoin conjugate. **2** constituted of naphthalene as the signalling fluorophore unit, whereas an acidic -OH group was also present for H-bonding interaction with anion(s). Compound **2** acted as a dual channel sensor for Cu^{2+} and F^- by showing fluorogenic and chromogenic selectivity respectively for the cation and the anion.²⁴ Hence, by gradually tuning the structure of receptors, we could devise a dual channel receptor for Cu^{2+} and F^- . In the current work, we shall hence discuss how and why such tuning lead to the development of a dual channel probe.



Scheme 1: Structures of compounds with their advantages and limitations.

2. Materials and methods

Reagents

All starting materials were purchased from SRL and used without further purification. All solvents used were of spectroscopic grade and purchased from Spectrochem. Metal perchlorate salts and tetrabutylammonium salts of anions were purchased from Merck and used as received.

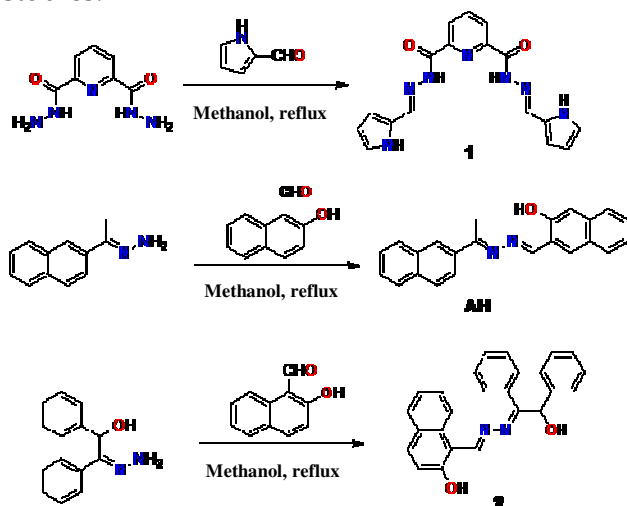
Apparatus

Steady state electronic absorption and fluorescence spectra were recorded on a Hitachi UV-Vis (Model U-3501) spectrophotometer and Perkin Elmer LS55 Fluorimeter, respectively. Time correlated single photon counting (TCSPC) technique has been used to measure time resolved emission using Horiba Jobin Yvon Fluorocube-01-NL fluorimeter. ^1H NMR spectra were recorded on a Bruker Advance 300 spectrometer, where chemical shifts (δ in ppm) were determined with respect to Tetramethylsilane (TMS) as the internal standard. The single crystals of AH and **2** were mounted on a Bruker-AXS SMART APEX II diffractometer equipped with a graphite monochromator and $\text{Mo K}\alpha$ ($\lambda = 0.71073 \text{ \AA}$) radiation. In each case, the crystal was placed 60 mm from the CCD and 360 frames were measured with a counting time of 5 s. The structure was solved using the Patterson method using SHELXS 97. Subsequent difference Fourier synthesis and least-square refinement revealed the positions of the remaining non-hydrogen atoms. Non-hydrogen atoms were refined with

independent anisotropic displacement parameters. Hydrogen atoms were placed in idealized positions and their displacement parameters were fixed to be 1.2 times larger than those of the attached non-hydrogen atoms. Successful convergence was indicated by the maximum shift/error of 0.001 for the last cycle of the least squares refinement. Absorption corrections were carried out using SADABS program. All calculations were carried out using SHELXS 97, PLATON 99, ORTEP-32 and WinGX system Ver-1.64.²⁵ Theoretical calculations were performed using Gaussian 09 package.²⁶

3. Results and discussions

Compounds **1**, **AH** and **2** were synthesized as shown in Scheme 2 and characterized using XRD, NMR, IR and ESI-MS studies.²²⁻²⁴



Scheme 2: Synthetic outline of compounds **1**, **AH** and **2**.

Naked eye and spectral responses

For checking the optical response of receptor **1** towards metal ions, the receptor was dissolved in aqueous methanol mixture (methanol: water 3:7) and perchlorate salts of transition metals dissolved in deionised water were added (2 equiv.) to it. To our delight, the receptor instantaneously showed a sharp change from light yellow to brown by addition of Cu (II) only (Fig. 1), indicating a likely interaction between **1** and copper. The sharp color change can be attributed to a possible intramolecular charge transfer due to complexation with copper. Under similar conditions, no addition of

other metals, including those commonly available in water, showed any significant color change. The selective color change for Cu²⁺ is a probable outcome of judicious balance between N and O donor center, for which Cu²⁺ shows a particular affinity as well as the matching of ionic radius of Cu²⁺ with the cavity size of receptor **1**. To further check the selectivity of receptor **1** towards Cu (II) ion, 10 equivalent of 0.1 mM aqueous solution of transition metals in the form of perchlorate salts were added to 10 μM solution of receptor **1** in aqueous methanol (methanol: water 3:7, v:v) and absorption spectra were recorded using UV-Vis spectrophotometer. The selectivity of sensor **1** towards Cu (II) was satisfyingly ensured with the generation of a new red shifted peak at ~392 nm with two shoulders at ~375 and ~416 nm respectively, whereas receptor **1** furnished a strong peak at ~330 nm ($\pi \rightarrow \pi^*$ transition), followed by a weak shoulder at 260 nm respectively. However, addition of other metals (10 equivalents, 0.1mM aqueous solution) produced too small a change in the absorbance to take into account and thus the response for Cu²⁺ was much greater than any other metal ions (Fig. 1a). The interaction of **1** with Cu²⁺, though already indicated from optical color change, could now be rationalized to be the result of complexation between **1** and Cu²⁺ due to the aforesaid spectral change and the selectivity of compound **1** towards copper can be firmly concluded.

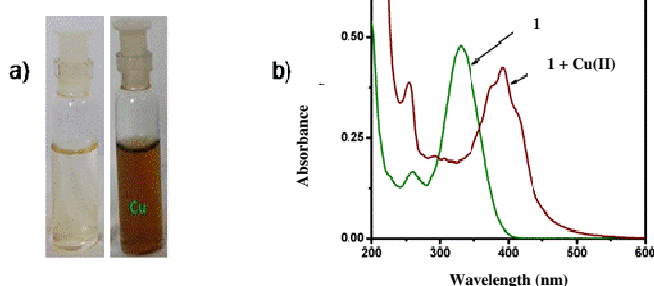


Fig. 1 (a) Color change of **1** in presence of Cu²⁺, (b) Absorption spectral response of **1** towards Cu²⁺.

However, there was no response upon addition of anions. This could be due to the high water fraction in the solvent system. The ESI-MS analysis of **1**-Cu²⁺ complex showed that a 1:2 type complexation has occurred between **1** and Cu²⁺. The high value of the binding constant also supported the affinity of **1** towards Cu²⁺ (Table

1). Theoretical modeling²² of **1** as also its Cu²⁺ complex showed sufficient lowering of HOMO-LUMO gap in the latter, indicating stabilization which was in accord with the observed red shift in the absorption profile of **1** upon adding Cu²⁺.

For compound **AH**, to an acetonitrile solution of the same (30 μM), aqueous acetonitrile (acetonitrile: water=8:2, v: v) solution of anions as their Tetrabutylammonium salts (15 equivalents) were separately added in glass vials. An instant orange coloration occurred only upon addition of fluoride (Fig. 2a). At this stage, it could be stated that **AH** can selectively detect F⁻ in aqueous acetonitrile solution perceived by a

Table 1. Important data for **1**, **AH** and **2**.

Probe (reference)	1 (22)	AH (23)	2 (24)
Mode of Cu ²⁺ detection	Colorimetry	-	Fluorimetry
Mode of F ⁻ detection	-	Colorimetry	Colorimetry
L.O.D of Cu ²⁺	4.0 nM	-	0.9 μM
L.O.D of F ⁻	-	1.31 μM	1.0 μM
K _b for Cu ²⁺	6.25×10 ¹² M ⁻²	-	1.03×10 ² M ⁻¹
K _b for F ⁻	-	6.617×10 ³ M ⁻¹	1.232×10 ³ M ⁻¹
Stoichiometry of binding with Cu ²⁺	1:2	-	1:1
Stoichiometry of binding with F ⁻	-	1:1	1:1

sharp color change. Additionally, to fulfil the major criterion for selectivity of **AH** towards F⁻ as far as 'naked-eye' color change is concerned, the response of the same in a mixture of competing anions was examined. Satisfyingly, a color change from pale yellow to orange yellow was observed upon addition of a solution of fluoride along with other anions having comparable basicity, i.e. AcO⁻, H₂PO₄⁻ and HSO₄⁻ (Fig. 2a). However, the extent of color change was curtailed to somehow which can be easily rationalized by considering the role of dilution when all other anions are present. **AH** can thus successfully detect F⁻ in aqueous acetonitrile. NMR titration studies²³ showed that the phenolic -OH is deprotonated in presence of F⁻. The binding constant between **AH** and F⁻ was calculated to be 6.617×10³ M⁻¹ from Benesi Hildebrand method. The lowering of HOMO-LUMO gap in the anion of **AH** occurred as evident from theoretical calculation.²³

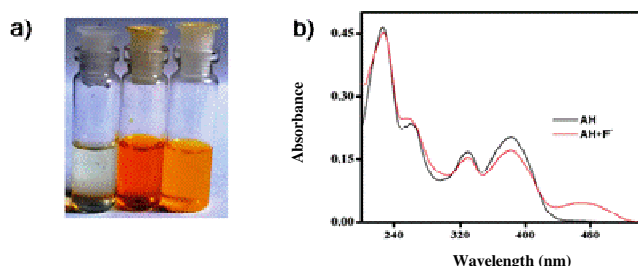


Fig. 2 (a) Color change of **AH** in presence of F⁻ and a mixture of anions (b) Absorption spectral change of **AH** upon addition of F⁻.

To a solution of receptor **2** (20 μM) in acetonitrile, metal perchlorate salts as their aqueous solution were added (10 equivalents). The aforesaid addition afforded a change in color from colourless to bright yellow in presence of Cu²⁺ ion. However, the addition of other transition metals also resulted in a similar change in color, the intensity, however, curtailed to some extent, rendering **2** as an inefficient optical probe in presence of multiple analytes. From the change in colour for copper, an affinity of **2** for preferential complexation with Cu²⁺ over other relevant metal ions and proceeded on to perform a UV-Vis titration was inferred. The UV-Vis spectrum of **2** furnished two distinguishable peaks at ~324 nm and ~373 nm respectively. Addition of other metal ions as

their aqueous solutions affected a slight variation in the absorbance value of the aforesaid two peaks, whereas addition of copper resulted in a weakly red shifted ill-resolved peak at ~ 390 nm. The observed red shift, however, may be attributed to a possible intramolecular charge transfer due to complexation with copper. To explore possibilities of **2** for being a sensor for Cu^{2+} , the next best alternative in the form of fluorescence spectroscopy was sorted too. The observations were promising as weakly fluorescent **2** (emission maxima at ~ 491 nm) experienced a remarkable increment in fluorescence intensity (~ 50 times) upon addition of 10 equivalents of Cu^{2+} , whereas addition of other metals produced no such increment (Fig. 3a). Under UV light, a bright green color was also observed. As receptor **2** has a phenolic $-\text{OH}$ group attached *ortho* to imine functionality the acidity of the former could be enhanced. Taking queue of this realization, we attempted to check the response of the aforesaid receptor towards anions. Tetrabutylammonium salts of anions in aqueous acetonitrile (1:9, v/v) were added separately to acetonitrile solution of the receptor. An instant and sharp change in color (Fig. 3b) was observed for fluoride (pale yellow to orange red) whereas little change was observed for other anions, even for anions with comparable basicity such as acetate and dihydrogenphosphate. Thus, apart from being an efficient 'turn-on' sensor for Cu^{2+} , receptor **2** holds an equal importance for 'naked eye' detection of F^- . The addition of F^- to a $10 \mu\text{M}$ acetonitrile solution of **2** afforded a broad hump at ~ 466 nm indicating **2** generated a new species upon addition of F^- .

The mechanism²⁴ of detection of Cu^{2+} by **2** was assigned to be Chelation Induced Enhancement of Fluorescence (CHEF) from TCSPC studies. From ^1H NMR studies²⁴ it was observed that the phenolic $-\text{OH}$ was deprotonated in presence of F^- with simultaneous H-bonding with the aliphatic OH in **2**. To our advantage, there was no effect on the emission aptitude of **2** and more importantly, the response mode of Cu^{2+} as well as F^- was devoid of any interference from each other.

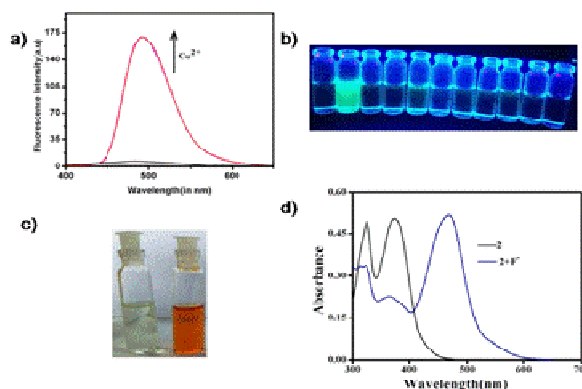


Fig. 3 (a) Emission enhancement of **2** upon adding Cu^{2+} , (b) Color under UV-light in presence of Cu^{2+} , (c) Naked eye color change upon addition of F^- , (d) Absorption spectral change on presence of F^- .

Practical applications of **1**, **AH** and **2**

The practical utility of each of **1**, **AH** and **2** were explored (Fig. 4). **1** showed prominent color change in the solid state²² upon treating with Cu^{2+} . **AH** neatly detected F^- in the solid state as well as in commercial toothpaste sample.²³ Finally, **2** could detect Cu^{2+} in **MDA-MB-468** cells owing to its fluorogenic response. Fluorogenic recognition was also achieved in the solid state. The detection of F^- in toothpaste sample as well as in solid state was also successful.²⁴

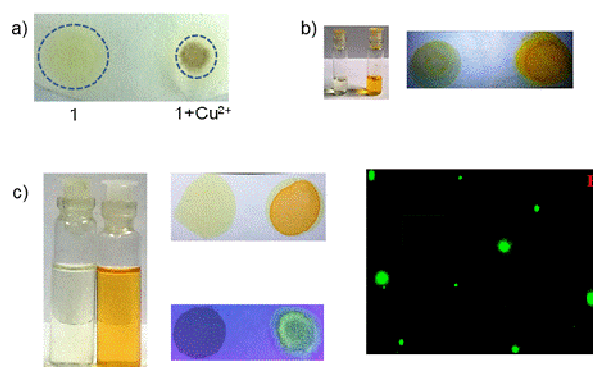
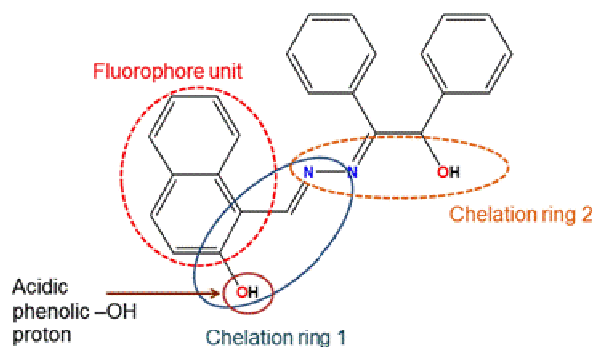


Fig. 4 (a) Change in color of paper strip coated with **1** upon addition of Cu^{2+} , (b) (left) Change in color of paper strip coated with **AH** upon addition of F^- - (right) Change in color of paper strip coated with **AH** upon addition of F^- , (c) change in color of **2** upon adding F^- ; solid state recognition of Cu^{2+} and F^- ; fluorescence microscopic image of **MDA-MB-468** cells treated with Cu^{2+} followed by **2**.

Justification of **2** being a dual sensor

We tried to explain why **2** acted as a dual channel sensor as also the failure of **1** and **AH** to perform so. The principal reason could be due to the structural features of the probes under consideration. To begin with, **1** is equipped with two chelate rings, each ring comprising of multiple N, O donors to assist in strong binding of **1** with Cu^{2+} . However, due to presence of weak fluorophores in the form of pyrole and pyridine as also due to quenching property of paramagnetic Cu^{2+} , no fluorescence signal could be observed. Although two amide protons were present, no response towards anion(s) was found. This could mainly be due to two reasons: (i) presence of electron rich pyrole and pyridine moiety sufficiently reduces the acidity of the amide protons. (ii) Large water fraction in the solvent system in which the cation detection experiments were performed. On the other hand, the phenolic $-\text{OH}$ proton in **AH** is considerably acidic owing to the strong $-I$ effect of the two naphthalene rings. The extensive delocalization enjoyed by **AH** upon deprotonation stood out to be the driving force behind the sensing mechanism. This also proved to be the reason for no fluorogenic response from **AH** even in the presence of a sufficiently strong fluorophore naphthalene. Since **AH** enjoys tremendous stabilization due to delocalization after formation of its anion in the ground state, increment of S_0 - S_1 gap occurs, thereby leading to no fluorogenic response. However, as far as metal detection was concerned, presence of a single six member ligand cavity was probably not enough to affect efficient metal sensing. Thus, from the failure of the above two compounds, the natural conclusion is introduction of at least two chelation spheres along with a sufficiently acidic proton attached to electronegative atom like N or O are the necessary prerequisites for devising a successful dual sensor. Now, to introduce dual channel response, a sufficiently strong fluorophore must be present along with the aforementioned

requisites. In compound **2**, all the conditions were maintained (Scheme 3). As can be seen from Scheme 3 two chelate rings are present, one offered by the benzoin moiety whereas the latter comes from the naphthalene moiety. Furthermore, since the crystal structures of **AH**²⁴ and **2**²⁵ were obtained, the distance between the O atom and H atom in the phenolic $-\text{OH}$ group was checked for both. In both the cases, the bond distances were 0.835 Å in each case. Thus, **2** would evidently behave as an anion sensor owing the acidity of the phenolic $-\text{OH}$ proton. The Cu^{2+} mediated increment in fluorescence intensity was due to the structural rigidity imparted in **2** post complexation with Cu^{2+} , thereby triggering the emission of the naphthalene unit. Hence, judicious structural modification enabled **2** to act as a dual channel sensor for Cu^{2+} and F^- .



Scheme 3: Structural features of **2**.

4. Conclusions

In this brief review, we focused on three ion selective synthesized probes **1**, **AH** and **2**. **1** and **2** individually acted as colorimetric sensors for Cu^{2+} and F^- respectively. **2** contained structural advantages of both **AH** and hence acted as a dual channel sensor for Cu^{2+} and F^- .

Acknowledgements

AB and SM would like to thank CSIR and UGC for granting fellowships. NG thanks DST, India (Project No. EMR/2016/004788) and CSIR, India (Project No. 01(2920)/18/EMP-II) for financial support.

Notes and references

- S. Rafique, M. Idrees, A. Nasim, H. Akbar and A. Athar, *Biotech. Mol. Biol. Rev.*, 2010, **5**, 38-45.
- J. J. R. Fraústo da Silva and R. J. P. Williams, Oxford University Press, New York, 2001.
- K.D. Karlin, *Science*, 1993, **261**, 701-708.
- D. Strausak, J.F.B. Mercer, H.H. Dieter, W. Stremmel and G. Multhaup, *Brain Res. Bull.*, 2001, **55**, 175-185.
- K. J. Barnham, C. L. Masters and A. I. Bush, *Nat. Rev. Drug Discovery*, 2004, **3**, 205-214.
- M. S. Tanner, *Am. J. Clin. Nutr.*, 1998, **67**, 1074S-1081S.
- R.L. Sheng, P. F. Wang, Y. H. Gao, Y. Wu and W. M. Liu, *Org. Lett.*, 2008, **10**, 5015-5018.
- D. Strausak, J. F. B. Mercer, H. H. Dieter, W. Stremmel and G. Multhaup, *Brain Res. Bull.*, 2001, **55**, 175-185.
- S. M. Azevedo, M. G. Cardoso, N. E. Pereira, C. F. S. Ribeiro, V. F. Silva and F. C. Aguiar, *Ciência e Agrotecnologia Lavras.*, 2003, **27**, 618-624.
- S. Matsuo, K.I. Kiyomiya and M. Kurebe, *Arch. Toxicol.*, 1998, **72**, 798-806.
- M. Kleerekoper, *Endocrinol. Metab. Clin. North Am.*, 1998, **27**, 441-452.
- D. Brianc, *Rev. Rhum. Engl. Ed.*, 1997, **64**, 78-81.
- A. Wiseman, Springer-Verlag, Berlin 1970.
- J. A. Weatherall, Springer-Verlag, Berlin 1969.
- A. Hesse, R. Muller, H. J. Schneider and F. Taubert, *Urologe A.*, 1978, **17**, 207-210.
- A. Ganguly, B. K. Paul, S. Ghosh, S. Kar and N. Guchhait, *Analyst*, 2013, **138**, 6532-654.
- A. Ganguly, S. Ghosh, S. Kar and N. Guchhait, *Spectrochim. Acta Part A.*, 2015, **143**, 72-80.
- S. Ghosh, M. A. Alam, A. Ganguly, S. Dalapati and N. Guchhait, *Inorg. Chim. Acta.*, 2015, **429**, 39-45.
- K. K. Upadhyay, R. K. Mishra, V Kumar and P. K. R. Chowdhury, *Talanta.*, 2010, **82**, 312-318.
- T. G. Jo, Y. J. Na, J. J. Lee, M. M. Lee, S. Y. Lee and C. Kim, *New J. Chem.*, 2015, **39**, 2580-2587.
- S. Ghosh, A. Ganguly, A. Bhattacharyya, M. A. Alam and N. Guchhait, *RSC Adv.*, 2016, **6**, 67693-67700.
- A. Bhattacharyya, S Ghosh and N Guchhait, *RSC Advances*, 2016, **6**, 28194-28199.
- A. Bhattacharyya, S. C. Makhal, S Ghosh and N Guchhait, *Spectrochim. Acta Part A.*, 2018, **198**, 107-114.
- A. Bhattacharyya, S Ghosh, S. C. Makhal, N Guchhait, *J. Photochem. Photobiol. A.*, 2018, **353**, 488-498.
- (a) G. M. Sheldrick, SHELXS 97, Program for Structure Solution, University of Göttingen, Germany, 1997; (b) G. M. Sheldrick, SHELXL 97, Program for Crystal Structure Refinement, University of Göttingen, Germany, 1997
- M.J. Frisch, et al., GAUSSIAN 03, Revision D.01, Gaussian, Inc., Wallingford, CT, 2004.

	<p>Arghyadeep Bhattacharyya received his B.Sc. (Hons) and M.Sc. in chemistry from Calcutta University. Now he is working in the Department of Chemistry, University of Calcutta as a Ph.D. student under the supervision of Prof. Nikhil Guchhait. He is interested on designing of new selective ions sensors.</p>
	<p>Subhash Chandra Makhal received his B.Sc. (Hons) and M.Sc. in chemistry from Calcutta University. Presently, he is working under Prof. Nikhil Guchhait at Calcutta University and his research interest is laser spectroscopy of charge transfer molecular systems in jet cooled molecular beam.</p>
	<p>Subhajit Saha did his B.Sc. (Hons) from Calcutta University and M.Sc. from NIT Durgapur. Presently working as CSIR JRF under Prof. Nikhil Guchhait in the Department of Chemistry, University of Calcutta.</p>
	<p>Nikhil Guchhait did his doctoral research under Prof. Mihir Chowdhury at Indian Association for the Cultivation of Science, Jadavpur. Presently, as a faculty member in the Department of Chemistry, University of Calcutta he is working in the field of photochemistry of some self designed molecular systems. His interest also includes laser spectroscopy of aromatic molecules in supersonic jet cooled molecular beam.</p>

Carbonic Acid Isomerization and Decomposition Chemistry of Potential Atmospheric Significance

Sourav Ghoshal and Montu K. Hazra*

Chemical Sciences Division, Saha Institute of Nuclear Physics, Homi Bhabha National Institute, 1/AF Bidhannagar, Kolkata-700 064, India

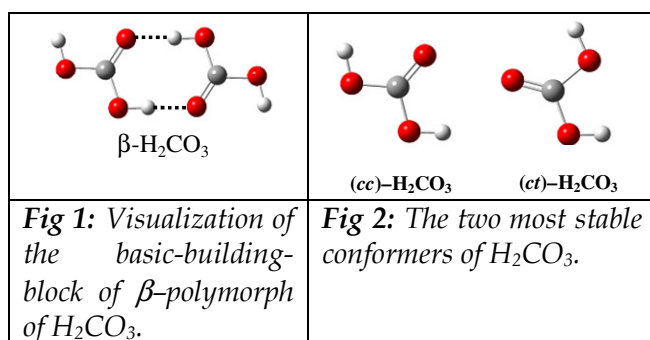
*Correspondence to: h.montu@saha.ac.in

Carbonic acid (H_2CO_3), a small molecule of six atoms involving three elements in the periodic table, belongs right at the interface between inorganic and organic chemistry. Over the last few decades, the H_2CO_3 molecule, an elusive species of atmospheric and/or environmental significance that exists both in the solid and gas-phase, has been the subject matter to various theoretical and experimental research groups. This is because of its importance in many fields including chemistry, biology, marine-chemistry, geochemistry, medicine, and especially in astrobiology relevant to the searching of possible life on Mars. The dissociation of the H_2CO_3 molecule ($\text{H}_2\text{CO}_3 \rightleftharpoons \text{H}^+ + \text{HCO}_3^-$) regulates the blood pH and acidification of the oceans. Similarly, the decomposition of the H_2CO_3 molecule into its constituents CO_2 and H_2O molecules ($\text{H}_2\text{CO}_3 \rightarrow \text{CO}_2 + \text{H}_2\text{O}$) is known to have an important role for the CO_2 transport in biological systems as well as in the global carbon cycle.

The H_2CO_3 molecule has been synthesized in various experimental conditions in the laboratory similar to those encountered in the extraterrestrial space.

Moreover, this molecule has been characterized by means of its microwave, matrix isolated infrared and mass spectra. Nevertheless, it is surprising that the detection of the H_2CO_3 molecule has not been possible yet in the Earth's atmosphere, and hunt for the free/isolated H_2CO_3 molecule, which has a half-life of ~ 0.18 million years, has become challenging not only in the Earth's atmosphere but also on Mars. It is hoped that one day, in near future, it will be detected as scientists achieve success in measuring the infrared spectra of the vapor phase H_2CO_3 resulting from its β -polymorph via the sublimation at cold temperatures. Given that there is an extensive scientific literature of the H_2CO_3 molecule, we note, however, that few important and fundamental questions, especially, about the isomerization and loss or instability of the H_2CO_3 molecule in its source, Earth's atmosphere and outer space including Mars and Venus need to be answered.

In the past, it was not known as the primary mechanism by which the H_2CO_3 molecule is decomposed, especially, in its source where its concentration becomes at the highest levels. Similarly, the matrix isolated infrared (IR) and Raman spectroscopy of the crystalline β - H_2CO_3 polymorph, which is only the distinct H_2CO_3 polymorph to date, suggest that the most possible basic-building-block of the β - H_2CO_3 polymorph consists of only and exclusively the most stable (*cc*)-conformer (Fig. 1 and 2). The sublimation of this crystalline H_2CO_3 polymorph at cold temperature (230-260K) results in both the most stable (*cc*)- H_2CO_3 and the second most stable (*ct*)- H_2CO_3 conformers in vapor phase with the



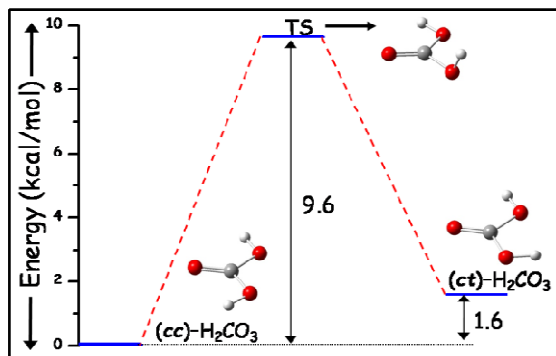


Fig 3: Isomerization Pathway via internal rotation of OH group

(cc)-H₂CO₃ conformer being as the major species (Fig. 2). Nevertheless, it was not known the possible mechanism by which the (cc)-H₂CO₃ → (ct)-H₂CO₃ conformational isomerization occurs during the sublimation of crystalline H₂CO₃ polymorph at cold temperature (230-260 K).

Hence, we highlight here our recent research works that provide the most possible answers of the abovementioned questions in the vast literature of carbonic acid. Below, to keep the presentation simple, the study of (cc)-H₂CO₃ → (ct)-H₂CO₃ conformational isomerization that occurs during the sublimation of crystalline H₂CO₃ polymorph at cold temperature has been highlighted first; and then the studies about the decomposition or loss of H₂CO₃ molecule.

In the past, the internal rotation of one of the two OH functional group present in the H₂CO₃ molecule was considered as the effective mechanism (Fig. 3) to explain the isomerization/interconversion between the two most stable conformers of carbonic acid [(cc)-H₂CO₃ → (ct)-H₂CO₃]. The barrier height for this isomerization reaction via the internal rotation of one of the two OH functional group present in the (cc)-H₂CO₃ conformer is ~9.5 kcal/mol. Hence, this rotation is expected to be hindered process, especially, during the sublimation of

crystalline H₂CO₃ polymorph at cold environment.

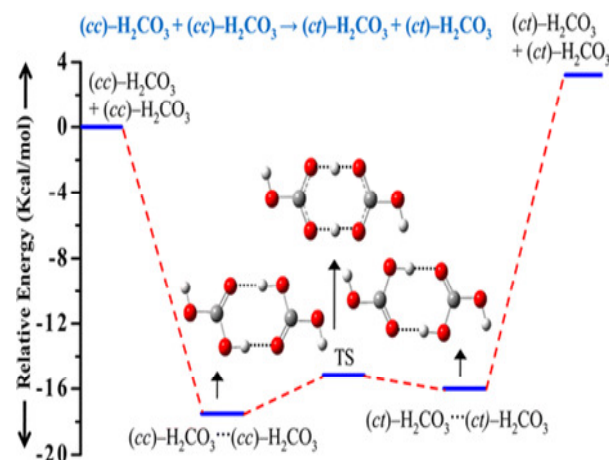


Fig 4: Potential energy profile for the autocatalytic isomerization reaction between two most stable H₂CO₃ conformers.

Recently, we have investigated the energetics of the carbonic acid-assisted (cc)-H₂CO₃ → (ct)-H₂CO₃ isomerization mechanism [(cc)-H₂CO₃ + (cc)-H₂CO₃ → (ct)-H₂CO₃ + (ct)-H₂CO₃] in the vapor phase.¹ The results of this study specifically and strongly suggest that double hydrogen transfer within the eight-membered cyclic doubly hydrogen-bonded (H-bonded) ring interface of the H₂CO₃ homodimer formed between two (cc)-conformers is ultimately the starting mechanism for the isomerization of the (cc)-conformer to its (ct)-conformer, especially, during the sublimation of the H₂CO₃ polymorph, which results in the vapor phase concentration of the (cc)-conformer at highest levels.¹ For the visualization of reaction energetics as well as the mechanism, the potential energy profile for the (cc)-H₂CO₃-assisted (cc)-H₂CO₃ → (ct)-H₂CO₃ isomerization reaction is shown in the Fig. 4.

It has been mentioned earlier that the H₂CO₃ molecule has been characterized in laboratory via the Matrix isolated Infrared spectroscopy.

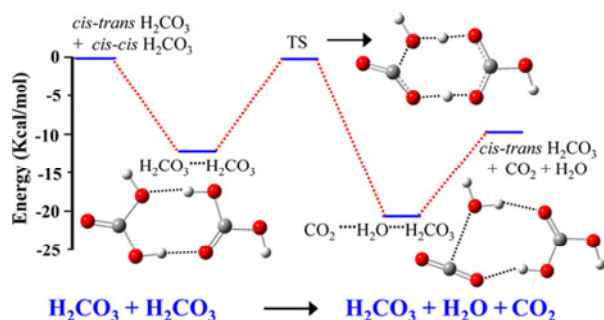


Fig 5: Potential energy profile for the autocatalytic decomposition reaction of H_2CO_3 molecule.

It is seen from this study that vapor-phase of H_2CO_3 molecule is unstable even in the water restricted environment, where vapor-phase of H_2CO_3 molecule decomposes into its constituents $\text{CO}_2 + \text{H}_2\text{O}$ molecules. To explore the mechanism for the decomposition of vapor-phase H_2CO_3 molecule in water restricted environment, we study the decomposition of H_2CO_3 molecule in presence of another H_2CO_3 molecule.² We perform the high level of calculation investigating the energetics of the $\text{H}_2\text{CO}_3 \rightarrow \text{CO}_2 + \text{H}_2\text{O}$ decomposition reaction in presence of another H_2CO_3 molecule (Fig. 5).

It is seen from the calculations that the effective barrier, defined as the difference between the zero-point vibrational energy (ZPE) corrected energy of the transition state and the total energy of the isolated starting reactants in terms of bimolecular encounters, is nearly zero for the H_2CO_3 -assisted $\text{H}_2\text{CO}_3 \rightarrow \text{CO}_2 + \text{H}_2\text{O}$ decomposition reaction, as mentioned above. Therefore, we conclude that H_2CO_3 -assisted $\text{H}_2\text{CO}_3 \rightarrow \text{CO}_2 + \text{H}_2\text{O}$ decomposition reaction is the primary mechanism for the decomposition of the vapor-phase H_2CO_3 molecules in its source or water restricted environment, especially, when the concentrations of the H_2CO_3 reaches its height levels.²

Given this, we again note, however, that the abovementioned mechanism is not expected to be the primary decomposition mechanism in the Earth's atmosphere or in the

surroundings away from the source points of H_2CO_3 . This follows as the probability of bimolecular collisions between two H_2CO_3 molecules is expected to significantly fall off due to dilution of H_2CO_3 concentration resulting from the presence of various other species away from the source. Therefore, we explore the instability of H_2CO_3 molecule in the Earth's atmosphere, especially, in presence of water monomer (H_2O), dimer [$(\text{H}_2\text{O})_2$] formic acid (FA $\equiv \text{HCOOH}$), acetic acid (AA $\equiv \text{CH}_3\text{COOH}$), sulfuric acid (SA $\equiv \text{H}_2\text{SO}_4$), hydroperoxide radical (OOH).³ It is seen from our study that the H_2CO_3 is an unstable molecule in the presence of H_2O and carboxylic acids (especially the FA and AA) detected in the Earth's atmosphere.³ In contrary, although the catalytic efficiencies of FA, AA and SA upon the $\text{H}_2\text{CO}_3 \rightarrow \text{CO}_2 + \text{H}_2\text{O}$ decomposition reaction are similar to each other, but nevertheless, SA, because of its low concentration, does not play a significant role in the $\text{H}_2\text{CO}_3 \rightarrow \text{CO}_2 + \text{H}_2\text{O}$ decomposition reaction in the 0 to 15 km altitude range of the Earth's atmosphere, especially, where the H_2CO_3 molecule is expected to be present. For the visualization purpose, and for an example, we present the FA-assisted H_2CO_3 decomposition ($\text{H}_2\text{CO}_3 + \text{FA} \rightarrow \text{CO}_2 + \text{H}_2\text{O} + \text{FA}$) reaction mechanism in Fig 6.

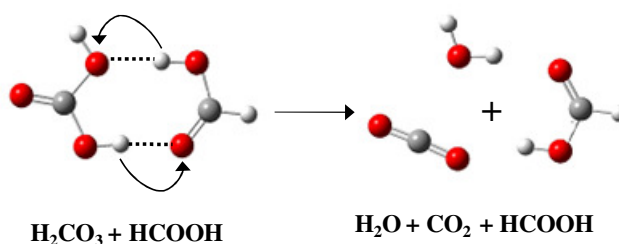


Fig 6: Mechanism of HCOOH -assisted H_2CO_3 decomposition reaction in the Earth's atmosphere.

In addition, the hydroxyl (OH) radical is known as the atmospheric detergent due to its high reactivity towards the hydrogen atom of the pollutant molecules present in the Earth's atmosphere. It is well known that many

oxygenated hydrocarbons and acids present in the Earth's atmosphere react more-or-less rapidly with the OH radical. Therefore, we also investigate both the energetics and kinetics of the OH radical-initiated H_2CO_3 degradation ($\text{H}_2\text{CO}_3 + \text{OH}^\bullet \rightarrow \text{HCO}_3^\bullet + \text{H}_2\text{O}$) reaction in the gas-phase, especially, to understand the atmospheric loss of the H_2CO_3 molecule in the presence of OH radical detected in the Earth's atmosphere.⁴

It is seen from the comparison of the reaction rates of abovementioned reactions that although the atmospheric concentration of the OH radical is substantially lower than the concentrations of the H_2O , formic acid (FA) and acetic acid (AA) in the Earth's atmosphere, nevertheless, the OH radical-initiated H_2CO_3 degradation reaction via proton-coupled electron transfer (PCET) mechanism (Fig. 7) has significant impact, especially towards the loss of the H_2CO_3 molecule in the Earth's atmosphere.⁴

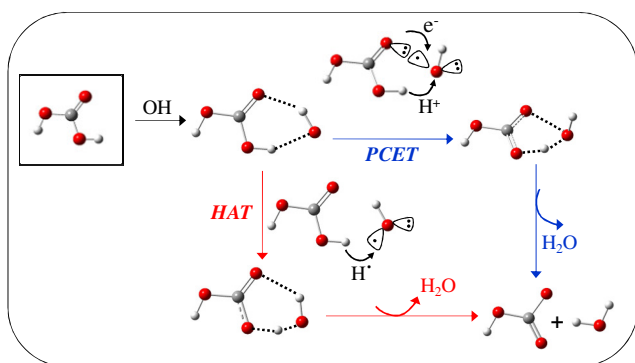


Fig 7: The proton-coupled electron transfer (PCET) and hydrogen atom transfer (HAT) mechanisms of the OH radical-initiated H_2CO_3 degradation reactions.

In summary and conclusion, the isomerization at cold sublimation temperature and decomposition of H_2CO_3 molecule occur potentially in presence of another H_2CO_3 molecule, especially, at the source points of H_2CO_3 .¹⁻² However, as the probability of bimolecular collisions between two H_2CO_3 molecules is expected to significantly fall off

due to dilution of H_2CO_3 concentration resulting from the presence of various other atmospheric species, the water and carboxylic acids-assisted $\text{H}_2\text{CO}_3 \rightarrow \text{CO}_2 + \text{H}_2\text{O}$ decompositions and the OH radical-initiated H_2CO_3 degradation have significant impact, especially, to interpret the loss or instability of the H_2CO_3 molecule in the Earth's atmosphere.²⁻⁴ In addition, we have paid attention to consider the potential impact of the H_2CO_3 decomposition and degradation reactions only in the Earth's atmosphere,¹⁻⁴ and not in the outer space including Mars or Venus, where especially the H_2CO_3 degradation in the presence of OH radical and the sulfuric acid (SA)-assisted H_2CO_3 decomposition may have much more potential impacts in comparison to that we found in the Earth's atmosphere.

Acknowledgement:

Financial Support from SINP and BARD Project (PIC No: 12-R&D-SIN-5.04-0103), Department of Atomic Energy, Government of India, is Gratefully Acknowledged

References:

1. Ghoshal, S.; Hazra, M. K. Autocatalytic Isomerizations of the Two Most Stable Conformers of Carbonic Acid in Vapor Phase: Double Hydrogen Transfer in Carbonic Acid Homodimers. *J. Phys. Chem. A* **2014**, *118*, 4620–4630.
2. Ghoshal, S.; Hazra, M. K. New Mechanism for Autocatalytic Decomposition of H_2CO_3 in the Vapor Phase. *J. Phys. Chem. A* **2014**, *118*, 2385–2392.
3. Ghoshal, S.; Hazra, M. K. $\text{H}_2\text{CO}_3 \rightarrow \text{CO}_2 + \text{H}_2\text{O}$ Decomposition in the Presence of H_2O , HCOOH , CH_3COOH , H_2SO_4 and HO_2 Radical: Instability of the Gas-

Phase H_2CO_3 Molecule in the Troposphere and Lower Stratosphere. *RSC Adv.* **2015**, 5, 17623–17635.

4. Ghoshal, S.; Hazra, M. K. Impact of OH Radical-Initiated H_2CO_3 Degradation in the Earth's Atmosphere via Proton-Coupled Electron Transfer Mechanism. *J. Phys. Chem. A.* **2016**, 120, 562-575.



Dr. Montu K Hazra received his B. Sc. (Chemistry Honours) from Shyamsundar College, Burdwan, in 1998 and M. Sc. University of Kalyani, in 2000. He did his Ph.D in 2008 from IIT, Kanpur under the supervision of Prof. Tapas Chakraborty. He did his Postdoctoral Research from University of California-San Diego during 2008- 2011). He has joined the Saha Institute of Nuclear Physics as an Assistant Professor and currently working in that position. His research interest is molecular beam spectroscopy.



Mr. Sourav Ghoshal is presently working as a Ph.D. student under supervision of Dr. Montu K Hazra Saha Institute of Nuclear Physics.

Cl Atom Radical Initiated Photo-Oxidation Reaction Kinetics of Alkyl Esters

Ramya Cheramangalath Balan and Rajakumar Balla

Department of Chemistry, Indian Institute of Technology Madras, Chennai-600036, India

1. Introduction

Hydrocarbons are volatile organic compounds (VOCs), which are getting emitted into the Earth's atmosphere from various biogenic and anthropogenic sources including vehicular emissions, industrial wastage, air pollution, agriculture etc (Kesselmeier *et al.*, 1999; Piccot *et al.*, 1992). On global scale VOCs emission from biogenic sources (mostly by vegetation) dominate over those from anthropogenic sources by a factor of ~10, whereas in urban areas anthropogenic VOCs often dominate (Guenther *et al.*, 1995). The VOCs released into the atmosphere, can be removed from the Earth's atmosphere by the physical processes of wet and dry deposition, and are transformed by the chemical processes of photolysis (at $\lambda > 290$ nm), reaction with atmospheric oxidants such as hydroxyl (OH) radical, nitrate (NO₃) radicals, Cl atom and O₃ molecule (Atkinson *et al.*, 1994, 1995) results in the formation of series of organic oxidation products in the atmosphere. The reactions of VOCs with oxidants will lead to the formation of photochemical smog, secondary organic aerosols (SOAs), acid rain and fog (Went, 1960; Rasmussen, 1972; Trainer *et al.*, 1987; Pandis *et al.*, 1991; Fehsenfeld *et al.*, 1992; Jacob and Wofsy, 1998). The formed SOAs are detrimental to human health as well as the ecological systems, and it can also act as cloud condensation nuclei distressing cloud properties leads to the imbalance in the hydrological cycle in the atmosphere (Zhang *et al.*, 2004).

The studies on atmospheric chemistry of VOCs are very much demanding in the present era to address the global environmental issues which are formed by release of VOCs into the Earth's atmosphere

such as toxic and carcinogenic human health effects and development of the global greenhouse effect, stratospheric ozone depletion, tropospheric ozone formation etc. It is now a well-documented fact that these VOCs are having dramatic effects on the air quality and global climate change (Ravishankara, 2003). The understanding of these processes is necessary for modelling atmospheric changes like stratospheric ozone depletion, recovery of the ozone layer, improvement in the regional air quality and the global climate change (Read *et al.*, 2007). Hence, a detailed description of VOCs and their reactivity with atmospheric oxidants needs to be understood. Therefore, it is required to know the kinetics through either experimental measurements or reliable computational methods for the reactions of VOCs with tropospheric oxidants such as OH radicals or Cl atoms, as well as the degradation pathways to estimate the fate and harmful effects of VOCs in the Earth's atmosphere.

2. Experimental

Relative rate experimental method was used to measure the kinetic parameters for the proposed reactions. In this method, the loss of the reactant to the oxidizing species (OH radical and Cl atoms) relative to a reference compound, whose rate coefficients is well known, will be followed. The rate coefficients were determined using standard relative rate expression, given below.

$$\ln \left\{ \frac{[\text{sample}]_0}{[\text{sample}]_t} \right\} = \frac{k_{\text{sample}}}{k_{\text{reference}}} \ln \left\{ \frac{[\text{reference}]_0}{[\text{reference}]_t} \right\}$$

where, [sample]₀, [sample]_t are the concentrations of the sample at times '0' and 't' respectively and [reference]₀, [reference]_t are the concentrations of the reference compounds

at times '0' and 't' respectively, k_{sample} and $k_{\text{reference}}$ are the rate coefficients for the reactions of sample and reference compounds with oxidising species. Plot of $\ln([\text{sample}]_0/[\text{sample}]_t)$ versus $\ln([\text{reference}]_0/[\text{reference}]_t)$ gives a straight line with zero intercept and slope gives the ratio of $k_{\text{sample}}/k_{\text{reference}}$. A schematic diagram of the experimental setup used for the relative rate experiments is shown in Figure 1. The experimental set up shown in Figure 2 mainly consists of (1) a temperature-regulated double walled Pyrex reaction chamber, (2) Excimer laser (KrF, Coherent Complex Pro) to produce 248 nm light as photolysis source to generate OH radical/Cl atom from $\text{H}_2\text{O}_2/(\text{COCl})_2$ precursors and (3) a Gas Chromatography (GC) used to monitor the concentrations of test molecules and reference compounds before and after the photolysis (4) GC-MS and GC-IR to analyse the formed products during the reactions.

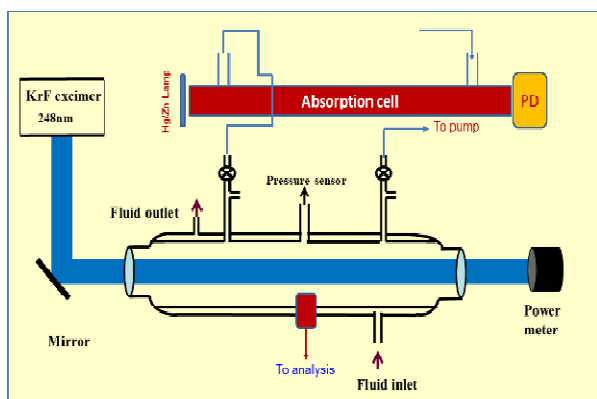


Figure 1: Schematic experimental setup used to carry out the kinetic experiments.



Figure 2: Relative Rate experimental setup designed and established in the laboratory to carry out the experiments.

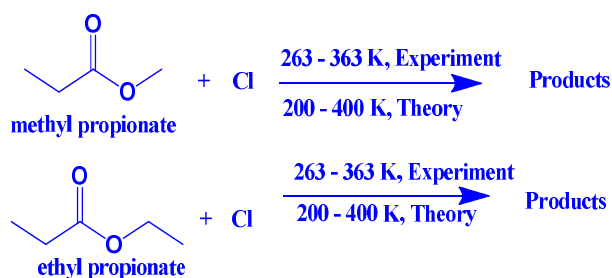
3. Computational

Temperature dependent rate coefficients were computed for the studied reactions over the temperature range of 200-400K using CVT and CTST in combination with CCD(T), M062X, BH&HLYP, B3LYP and MP2 level of theories with cc-pVDZ, 6-311++G(d,p), 6-31G+(d,p) and 6-31G(d,p) basis sets (Truhlar *et al.*,1984). Tunnelling corrections were included in the rate coefficient calculations. The following general approach was used in CVT/SCT to calculate the temperature dependent rate coefficients.

$$k^{GT}(T, s) = \sigma \frac{k_B T}{h} \left(\frac{Q^{GT}(T, S)}{\phi^R(T)} \right) \exp \left(\frac{-V_{MEP}(s)}{k_B T} \right)$$

$$k^{CVT}(T) = \min_s k^{GT}(T, s) = k^{GT}[T, s^{CVT}(T)]$$

where k^{CVT} is the rate coefficient from CVT and k^{GT} is the generalized rate coefficient. T is the temperature (in Kelvin), k_B is the Boltzmann constant, h is Planck's constant, σ is the reaction path degeneracy, ϕ^R and Q^{GT} are the partition functions of a generalized reactant at 's' and transition state respectively. s^{CVT} is the reaction coordinate of the canonical variational transition state dividing surface. $V_{MEP}(s)$ is the potential energy of generalized TS at 's'. The corrected tunnelling rate coefficients ($k^{CVT/SCT}(T)$) were obtained by multiplying a temperature dependent transmission coefficient $K^{CVT/SCT}(T)$ with CVT rate coefficient.



$$k^{CVT/SCT}(T) = K^{CVT/SCT}(T) k^{CVT}(T)$$

4. Results and Discussions

Cl atom reaction with methyl propionate and ethyl propionate

Temperature dependent rate coefficients were measured using relative rate method with ethane and ethylene as reference compounds (Atkinson *et al.*, 2001; Coquet *et al.*, 2000) and calculated using DFT methods for the reactions of Cl atoms with methyl and ethyl propionate. The measured and calculated rate coefficients at 298K for the reactions of Cl atoms with methyl and ethyl propionate are $(2.42 \pm 0.44) \times 10^{-11} \text{ cm}^3 \text{ molecule}^{-1} \text{ s}^{-1}$, $(3.76 \pm 0.35) \times 10^{-11} \text{ cm}^3 \text{ molecule}^{-1} \text{ s}^{-1}$, $1.73 \times 10^{-11} \text{ cm}^3 \text{ molecule}^{-1} \text{ s}^{-1}$ and $1.67 \times 10^{-11} \text{ cm}^3 \text{ molecule}^{-1} \text{ s}^{-1}$ respectively which are in very good agreement with reported rate coefficients (Notario *et al.*, 1998; Andersen *et al.*, 2011; Cavalli *et al.*, 2000).

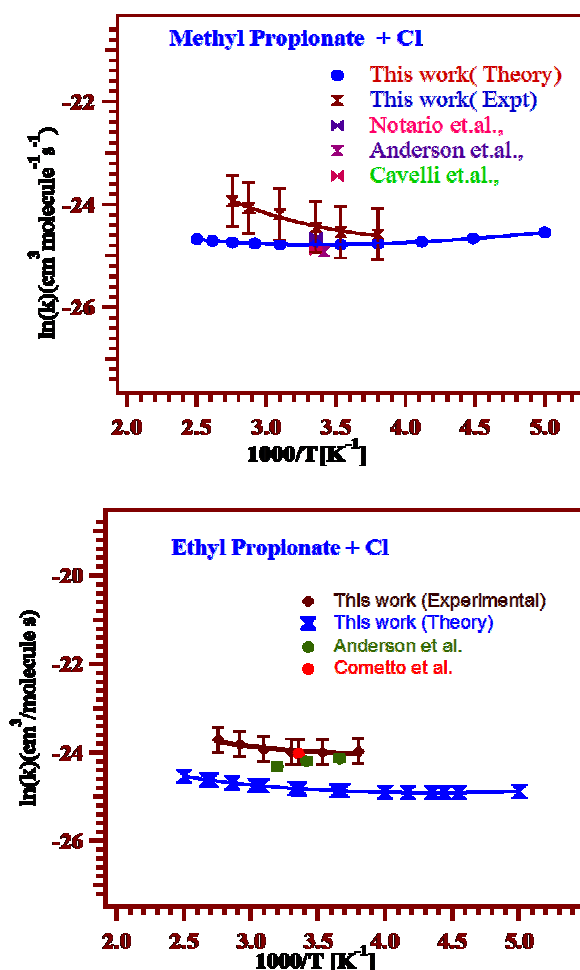


Figure 3: Arrhenius plots for the reactions of Cl atoms with methyl propionate and ethyl propionate.

The measured and calculated rate coefficients were used to fit the data and corresponding the Arrhenius plots are given in Figure 3. Product analysis was carried out and based on observed products, the probable atmospheric degradation mechanism for both test molecules was proposed and are shown in Figure 4.

Product Analysis Methyl propionate

To provide more evidence for the reaction mechanism, the product analysis was carried out by using GC-MS (7890B-5977A MSD) as well as GC-IR (7890B-is50) as analytical tools. HP-PLOT'Q' column was used with helium as carrier gas. The temperature of the oven was varied between 40-200 °C and was programmed to increase the temperature at the rate of 5 °C min⁻¹. A flow rate of the carrier gas was maintained at 1.2 ML min⁻¹. The products identified are CO₂, CH₂=C=O, acetaldehyde, acetic acid, methyl acetate, methyl pyruvate, chloroacetic acid, chloroform, acetaldehyde, HCl and methyl formate. A plausible reaction mechanism was derived based on the observed products and is depicted below. When Cl atom abstracts alpha hydrogen from MP (-CH₂- position), CH₃C•HC(O)OCH₃ radical is formed. On further reacting with oxygen, it forms corresponding peroxy radical. This peroxy radical further undergoes rearrangement to form acetaldehyde along with CO₂. It can also eliminate •HO₂ radical, which leads to the formation of methyl acrylate. The formed methyl acrylate further decomposes in presence of O₂ leading to the formation of ketene (CH₂=C=O) and CO. On the other hand, the formed peroxy radical (CH₃C(OO•)HC(O)OCH₃) recombines in the presence of oxygen to form methyl pyruvate. Methyl pyruvate on further decomposition forms acetaldehyde, CO₂, chloroform, HCl and methyl formate. In presence of Cl and O₂, acetaldehyde will form chloroacetic acid, acetic acid, HCl, CO₂ and chloroform.

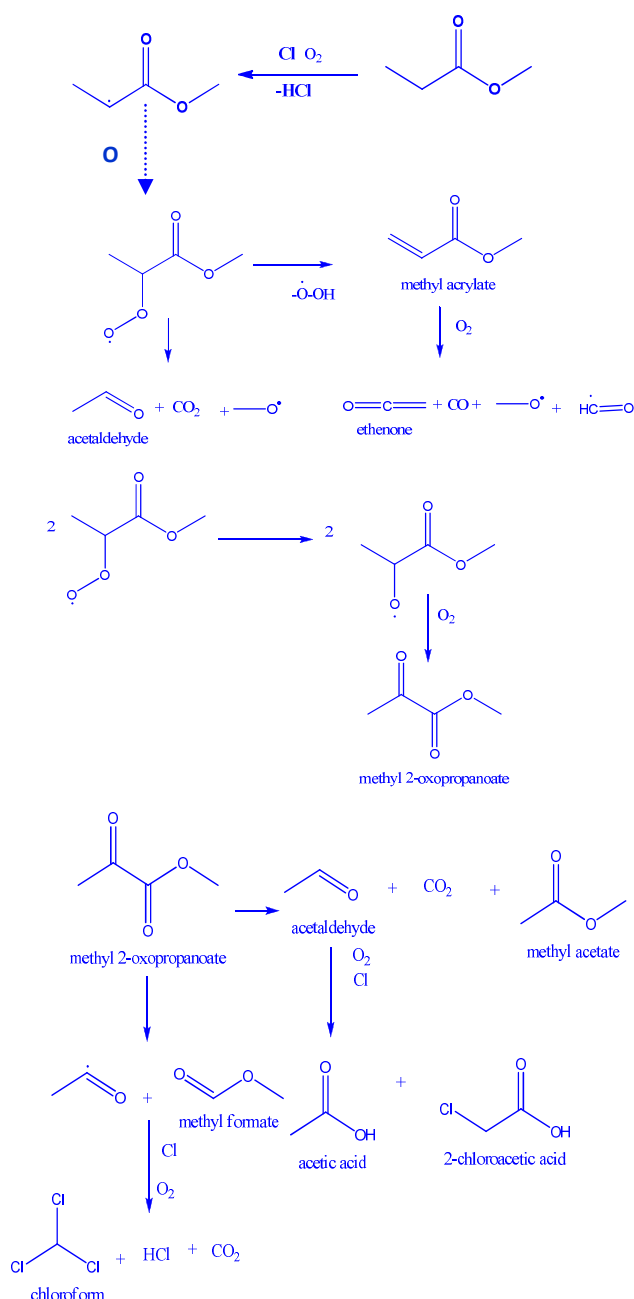


Figure 4: Proposed degradation mechanism for the reaction of methyl propionate with Cl atoms based on the obtained products via GC-MS and GC-IR analysis.

Ethyl propionate

The products identified in the present investigation are vinyl propionate, propionic acid, acetone, acetaldehyde, CO₂ and HCl. Propionic acid is an important atmospheric trace gas, as it contributes to increasing the

acidity of the atmosphere. A plausible reaction mechanism was proposed based on the observed products and is shown in Figure 5. When Cl abstracts alpha hydrogen from EP (-CH₂- position via TS4), C₂H₅C(O)OC•H₂CH₃ radical is formed along with HCl. On further reacting with oxygen, it forms corresponding peroxy radical (C₂H₅C(O)OCOO•H₂CH₃ [i.e., RO₂•]). This peroxy radical (RO₂•) will eliminate •HO₂ radical, which leads to the formation of vinyl propionate. On the other hand, the peroxy radical (RO₂•) recombines in the presence of oxygen to form (C₂H₅C(O)OCO•H₂CH₃ [i.e., RO•]). This RO• will undergo further rearrangements, fragmentation and re-combination reactions and leads to the formation of various products (propionic acid, acetaldehyde, CO₂ and acetone). Another possible channel is the H-abstraction from the -CH₂ group via TS3 which leads to the formation of CH₃C•HC(O)OCH₂CH₃. In the presence of oxygen, this radical would also form the corresponding peroxy radical and leads to the formation of acetaldehyde and carbon dioxide as further products, as identified in our analysis.

The obtained temperature dependent rate coefficients for the studied reactions are

$$k_{\text{methyl propionate}+\text{Cl, Expt}(263-363\text{K})} = [(3.25 \pm 1.23) \times 10^{-16}] T^2 \exp[-(33 \pm 4)/T] \text{ cm}^3 \text{ molecule}^{-1} \text{ s}^{-1}$$

$$k_{\text{methyl propionate}+\text{Cl, Theory}(200-400\text{K})} = (7.22 \times 10^{-16}) T^{1.5} \exp(466/T) \text{ cm}^3 \text{ molecule}^{-1} \text{ s}^{-1}$$

$$k_{\text{ethyl propionate}+\text{Cl, Expt}(263-363\text{K})} = [(6.88 \pm 1.65) \times 10^{-24}] T^{4.5} \exp[(1108 \pm 87)/T] \text{ cm}^3 \text{ molecule}^{-1} \text{ s}^{-1}$$

$$k_{\text{ethyl propionate}+\text{Cl, Theory}(200-400\text{K})} = (6.73 \times 10^{-19}) T^{2.74} \exp[(571)/T] \text{ cm}^3 \text{ molecule}^{-1} \text{ s}^{-1}$$

There is an increase in the rate coefficient with an increase in carbon number which indicates that reactivity increases by insertion of an electron donating group (-CH₂) (Atkinson *et al.*, 2003). The cumulative lifetimes of methyl propionate and ethyl propionate were estimated to be a few hours; hence, these

compounds will be degraded within a few hours as soon as they are released into the atmosphere. Therefore, their impact on global warming is insignificant.

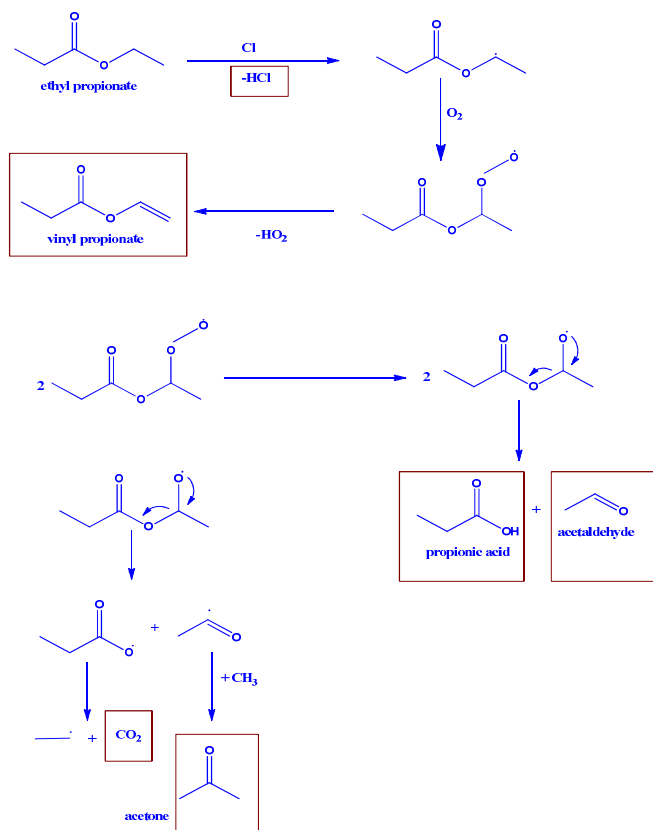


Figure 5: Proposed degradation mechanism for the reaction of ethyl propionate with Cl atoms based on the obtained products via GC-MS and GC-IR analysis.

Summary

The temperature dependent rate coefficients for the reactions of Cl atoms with methyl propionate and ethyl propionate were measured using relative rate method and calculated using dual level direct dynamics over the temperature range of 200-400K and are in good agreement with reported rate coefficients at 298 K. The rate coefficient for the reaction is observed to be increasing with increasing carbon number, due to the availability of more H-abstraction channels. The product analysis was carried out for both

the molecules methyl acrylate was obtained as major products in the case of methyl propionate and propionic acid was obtained as the major product in the case of ethyl propionate. The calculated atmospheric lifetimes for both the molecules suggest that these esters are mainly degraded by OH radical reactions under ambient conditions but in the marine boundary layer, Cl atom reactions compete with OH, NO₃ radicals and O₃ reactions.

References

- Andersen, V.F., Berhanu, T.A., Nilsson, E.J., Jørgensen, S., Nielsen, O.J., Wallington, T.J. and Johnson, M.S., (2011) Atmospheric chemistry of two biodiesel model compounds: methyl propionate and ethyl acetate. *J. Phys. Chem. A*, 115, 8906-8919.
- Anderson, R.S., Huang, L., Iannone, R. and Rudolph, J., (2007) Measurements of the ¹²C/¹³C kinetic isotope effects in the gas-phase reactions of light alkanes with chlorine atoms. *J. Phys. Chem. A*, 111, 495-504.
- Atkinson, R. and Arey, J., (2003) Atmospheric Degradation of Volatile Organic Compounds. *Chem. Rev.*, 103, 4605-4638
- Atkinson, R., (1994) Gas-phase tropospheric chemistry of organic compounds. *J. Phys. Chem. Ref. Data*, Monograph 2, 1-216.
- Atkinson, R., (1995) Gas phase tropospheric chemistry of organic compounds. In: Hester, R.E., Harrison, R.M. (Eds.). *Volatile Organic Compounds in the Atmosphere*, Issues in Environmental Science and Technology, 4, The Royal Society of Chemistry, Cambridge, UK, 65-89.
- Atkinson, R., Baulch, D.L., Cox, R.A., Crowley, J.N., Hampson Jr, R.F., Kerr, J.A., Rossi, M.J. and Troe, J., (2001) Summary of evaluated kinetic and photochemical data for atmospheric chemistry. IUPAC

- Subcommittee on gas kinetic data evaluation for atmospheric chemistry, 1-56.
- Cavalli, F., Barnes, I., Becker, K.H. and Wallington, T.J.,(2000) Atmospheric oxidation mechanism of methyl propionate. *J. Phys. Chem. A*.104, 11310-11317.
- Coquet, S. and Ariya, P.A.,(2000) Kinetics of the gas-phase reactions of Cl atom with selected C₂-C₅ unsaturated hydrocarbons at 283 < T < 323 K. *Int. J. Chem. Kinet.* 32, 478-484.
- Fehsenfeld, F. C., Calvert, J., Fall, R., Goldan, P., Guenther, A. B., Hewitt, C. N., Lamb, B., Liu, S., Trainer, M., Westberg, H. and Zimmerman, P., (1992) Emissions of volatile organic compounds from vegetation and implications for atmospheric chemistry, *Glob. Biogeochem. Cycles*, 6, 389-430.
- Guenther, A., Geron, C., Pierce, T., Lamb, B., Harley, P. and Fall, R., (2000) Natural emissions of non-methane volatile organic compounds, carbon monoxide, and oxides of nitrogen from North America. *Atmos. Environ.* 34, 2205-2230.
- Jacob, D. and Wofsy, S., (1998) Photochemistry of biogenic emissions over the Amazon forest. *J. Geophys. Res.* 93, 1477-1486.
- Kesselmeier, J. and Staudt, M., (1999) Biogenic volatile organic compounds (VOC): an overview on emission, physiology and ecology. *J. atmos. Chem.* 33, 23-88.
- Krampf, F. and Paulson, S. E., (1998) On the uncertainties in the rate coefficients for OH reactions with hydrocarbons, and the rate coefficients of the 1,3,5-trimethylbenzene and m-xylene reactions with OH radicals in the gas phase. *J Phys Chem A*102, 2685-2690.
- Notario, A., Le Bras, G. and Mellouki, A.,(1998) Absolute rate constants for the reactions of Cl atoms with a series of esters. *J. Phys. Chem. A.* 102, 3112-3117.
- Orlando, J. J., Tyndall, G.S., Apel, E.C., Riemer, D.D. and Paulson, S.E., (2003) Mechanisms of the reaction of Cl atoms with a series of unsaturated hydrocarbons under atmospheric conditions. *Int. J. Chem. Kinet.*35, 334-353.
- Pandis, S. N., Paulson, S. E., Seinfeld, J. H. and Flagan, R. C., (1991) Aerosol formation in the photooxidation of isoprene and β -pinene. *Atmos. Environ.*, 25, 997-1008.
- Piccot, S.D., Watson, J.J. and Jones, J.W., (1992) A global inventory of volatile organic compound emissions from anthropogenic sources. *J. Geophys. Res. Atmos.* 97, 9897-9912.
- Rasmussen, R. A., (1972) What do the hydrocarbons from trees contribute to air pollution, *J. Air Pollut. Control Assoc.* 22, 537-543.
- Ravishankara, A.R., (2003) Introduction: Atmospheric Chemistry- Long-Term Issues. *Chem. Rev.*,103, 4505-4507.
- Read, K.A.; Lewis, A.C., Salmon, R.A.; Jones, A.; Bauguitte, S. (2007) OH and halogen atom influence on the variability of non-methane hydrocarbons in the Antarctic boundary layer. *Tellus*, 59, 22-38
- Singh, H. B., Thakur, A. N., Chen, Y. E. and Kanakidou, M., (1996) Tetrachloroethylene as an indicator of low Cl atom in the troposphere. *Geophys. Res. Lett.* 23, 1529-1532.
- Sprengnether, M. M., Demerjian, K. L., Dransfield, T. J., Clarke, J. S., Anderson, J.G., Donahue, N. M.,(2009) Rate constants of nine C₆-C₉ alkanes with OH from 230 to 379 K: chemical Tracers for [OH]. *J Phys Chem A.* 113, 5030-5038.

Trainer, M., Hsie, E. Y., Mcken, S. A., Tallamraju, R., Parrish, D. D., Fehsenfeld, F.C. and Liu, S. C., (1987) Impact of natural hydrocarbons on hydroxyl and peroxy radicals at a remote site, *J. Geophys. Res.* 92, 11,879-11,894.

Truhlar, G. and Garrett, B. C., (1984) Variational Transition State Theory. *Annu. Rev. Phys. Chem.* 35, 159-189.

Went, F. W., (1960) Blue hazes in the atmosphere. *Nature*, 197, 64-643.

Yujing, M. and Mellouki, A., (2001) Temperature dependence for the rate constants of the reaction of OH radicals with selected alcohols. *Chem. Phys. Lett.*, 333, 63-68.

Zhang, R., Suh, I., Zhao, J., Zhang, D., Fortner, E. C., Tie, X., Molina, L. T. and Molina, M. J., (2004) Atmospheric new particle formation enhanced by organic acids. *Science*, 304, 1487-1490.



Professor B. Rajakumar had obtained B.Sc from Sri Durgaprasad Sharaf college of arts and applied sciences, Sriram Nagar, Garividi of Vizianagaram District of Andhra Pradesh. Studied M.Sc in Chemistry in the School of Chemistry, Andhra University Visakhapatnam and obtained his PhD in 2002 under the supervision of Prof. E. Arunan. Further, pursued research in the area of the atmospheric chemistry and physics as a postdoctoral researcher under the leadership of the famous scientist Prof. Dr A. R. Ravishankara at the National Oceanic and Atmospheric Administration (NOAA), Boulder, Colorado, U. S. A. Returned to India in 2006 and joined the Department of Chemistry at the Indian Institute of Technology Madras as an Assistant Professor and currently working as a Professor.



Ramya Balan received her B.Sc. (M.P.C) in 2006 from Little Flower College Guruvayur (University of Calicut), Kerala and M.Sc. in chemistry from Sree Narayana College Nattika (University of Calicut) in 2009. Now she is working in the Department of Chemistry, IIT Madras as a PhD student under the supervision of Prof. B. Rajakumar. She is interested in studying the kinetics and dynamics of the compounds of atmospheric interest by using experimental techniques such as CRDS and LIF as well as computational methods.

Morpholine: In Gas Phase and Interface

Sumana SenGupta*, Ankur Saha, Awadhesh Kumar*, and P.D. Naik

Radiation and Photochemistry Division, Bhabha Atomic Research Centre, Mumbai – 400 085, INDIA.

Email: sumansg@barc.gov.in, awadesh@barc.gov.in

Abstract

The complete knowledge of the atmospheric reactions of morpholine (a polyfunctional cyclic compound with considerable toxicity) in terms of reaction kinetics, photodissociation dynamics, and absorption on air-water interface, is important because it is regularly released in the environment through its various usage. Kinetics investigation of reaction of OH radical with morpholine, using LP-LIF technique in the temperature range of 298-363 K revealed high value of rate constants ($k(298) = (8.0 \pm 0.1) \times 10^{-11} \text{ cm}^3 \text{ molecule}^{-1} \text{ s}^{-1}$). The rate constant decreases with temperature in the range studied, with the approximate dependence given by $k(T) = (1.1 \pm 0.1) \times 10^{-11} \exp[(590 \pm 20)/T] \text{ cm}^3 \text{ molecule}^{-1} \text{ s}^{-1}$. Theoretical studies show that pre-reactive complexes, 5-7 kcal mol⁻¹ lower in energy as compared with the reactants, are formed because of H-bond interaction between OH and the N/O atom of morpholine. The dynamics study of photodissociation of morpholine at 193 nm using LP-LIF, lead to detection of OH radical, in spite of its absence in morpholine's structure. The results implied presence of an energy barrier in the reaction mechanism involving at least two different pathways, both through initial ring opening, followed by intramolecular rearrangement, and then further bond dissociation to eventually expel OH radical. The structure and orientation of interfacial morpholine molecules have been studied, In order to understand its interfacial behaviour in aqueous phase, using vibrational sum-frequency generation (VSFG) spectroscopy at SSP and PPP polarizations for CH (2800-3000 cm⁻¹) and the OH (3000-3750 cm⁻¹) stretch regions at the air-liquid/solution interfaces. The results indicated presence of morpholine molecules at the interfaces with net polar orientation. In pure morpholine, the most predominant conformation of molecules is equatorial chair, but in aqueous solution, contribution from axial chair/twist boat conformer seems to increase. The net polar orientation of water molecules also increases on addition of morpholine. The VSFG spectra were also measured in the presence of 300 mM HCl, which showed indications of protonation of the interfacial morpholine molecules.

1. Introduction

Morpholine and its derivatives are regularly used in the synthesis of numerous pesticides, chemicals and drugs, as solvents and as anticorrosive agents in boiler water, particularly in nuclear power reactors [1]. Morpholine itself is used widely in medical field to treat pain, inflammation, migraine, emesis and fungal infection. This group of compounds, however, is toxic and mutagenic, which is readily absorbed through skin. Under environmental and physiological conditions, N-nitrosomorpholine, a proven animal carcinogen, is formed by the reaction of solutions of nitrite, or gaseous nitrogen oxides, with dilute solutions of morpholine [2]. The volatility of morpholine is comparable to water and it is also completely miscible in water.

Human and environmental exposure to morpholine arises from industrial emissions and effluents as well as directly from some of its usages, which lead to the release of morpholine into the environment through volatilization in the atmosphere as well as dissolution in the aqueous phase. Structurally, morpholine is a polyfunctional compound, a secondary amine, and an ether. As a means to understand the fate of morpholine in the atmosphere, we have measured the kinetic parameters of the OH radical reaction with morpholine in the gas phase within the temperature range 298-363 K, as well as photodissociation of morpholine molecule at 193 nm. The results helped us to understand the effect of the heteroatoms, as well as ring

structure on the behaviour of heterocyclic molecules in the atmosphere.

Morpholine may also be absorbed in the air-water surface in the atmosphere due to its high solubility. Its effect on the aqueous surface is expected to depend on its structure and orientation. Morpholine is known to have a number of conformations in the ground state which are quite close in stabilisation energy. We have measured vibrational spectra of interfacial morpholine molecules at the air-morpholine and air-solution interfaces, employing the Vibrational Sum-Frequency Generation (VSFG) Spectroscopy. We have measured VSFG spectra of its dilute aqueous solution (10-60 mM concentration) in the CH (2800-3000 cm^{-1}) and the OH (3000-3750 cm^{-1}) stretch regions. The water droplets in the atmosphere, mostly in cloud and aerosol, is known to have acidic surface [3]. In order to understand the behaviour of morpholine in similar environments, we have also investigated the influence of HCl addition on the spectral features of morpholine vibrational frequency on air-solution interface. Sum-frequency generation (SFG) have been developed as very effective surface selective techniques for probing chemical bonding, structure, and molecular interaction at the interfaces in a interface specific, sensitive and selective way. As these processes are forbidden under the electric-dipole approximation in the bulk of media having inversion symmetry, they can specifically probe any interface accessible by light without any interference from the bulk phases [4].

2. Methods and methodologies

2.1 Gas-phase Studies

The set-up for the dynamic and kinetic studies is described in detail in our previous publications [5]. The reactor employed for both gas-phase kinetic and dynamic studies was a double-walled pyrex glass cell fitted with MgF_2 windows at Brewster angle to facilitate passage of the pump and the probe laser beams, which intersect at right angle at the center and pass through the exit window. The pressure inside

the reactor was measured by a capacitance manometer, kept at the base of the reactor. For the dynamics studies, the pump laser was the 193 nm output (ArF mode) and in the kinetics study, hydroxyl radicals were generated by photolysis of H_2O_2 at 248 nm output (KrF mode) of the same excimer laser (Lambda Physik, Model Compex-102, fluorine version) and probing of the products was done with a seeded Nd:YAG pumped dye laser (bandwidth = 0.07 cm^{-1}), having doubling and mixing modules (Quantel, TDL 90). The fluorescence of OH from the intersection volume of the pump and the probe beams was collected by a lens (diameter= 38 mm, focal length= 50 mm) and detected by a PMT, kept orthogonal to both of the laser beams, after passing through a band-pass filter ($\lambda_{\text{center}} = 310 \text{ nm}$, $\text{fwhm} = 10 \text{ nm}$, $\%T = 10\%$) to remove the scattering from the photolysis laser. For both kinetics and dynamics, LIF signal was integrated by a boxcar, averaged for 30 laser shots, and fed into an interface for A/D conversion. Both the pump and the probe laser intensities were measured by photodiodes, and the values were used to normalize the LIF intensities with respect to laser intensity fluctuations. For photodissociation dynamics studies, all the LIF measurements were carried out at $\sim 100 \text{ mTorr}$ pressure of morpholine and at the time delay of 50 ns between the photolysis and the probe lasers.

For temperature dependent kinetic studies, to obtain the temporal profile of OH concentration, the delay between the pump and the probe laser pulses was varied from zero to $\sim 5 \text{ ms}$, in steps of a few microseconds, with the help of a delay generator. The probe pulse excites the $P_1(2)$ line in the (0,0) band of the ($A^2\Sigma$, $V' = 0$) \leftarrow ($X^2\Pi$, $V'' = 0$) transition of the OH radical. The temperature of the cell was maintained by circulating water through the outer jacket from a thermostated bath, which was measured by inserting a Chromel-Alumel thermocouple.

The gaseous reaction mixture for the kinetic studies consisted of the precursor molecule H_2O_2 , the reactant morpholine, and

the buffer gas He. Both H₂O₂ and morpholine, diluted by helium gas, were flown from two separate reservoir flasks (5 L) having Teflon stopcocks. These mixtures, along with He from a cylinder, were flowed into the reactor via calibrated mass flow controllers (MFC) and premixed before entering the reaction cell. The rate of flow of the H₂O₂/He mixture into the reaction cell was kept constant at 25 SCCM in all cases and the total pressure inside the reaction cell was kept nearly constant (52 Torr). The rates of flow of morpholine-He mixture and pure He were adjusted at different ratios, keeping the total flow rate of these two together always at 25 SCCM, to obtain different sample concentrations in the reaction cell. The temperature of the reaction cell was varied in the range of 298-363 K by circulating water through the outer jacket from a thermostated bath. The flow velocity of the experimental mixture was kept to be 15 cm/s to make sure that a fresh gas mixture is seen by each photolysis laser pulse (20 Hz). The number densities of H₂O₂, OH generated, and morpholine inside the reaction cell were kept to be about 10¹⁴, 10¹⁰, and 10¹⁴ molecules cm⁻³, respectively, to maintain a pseudo-first-order condition with [reactant] > [OH]. The number density of morpholine in the reaction volume was calculated from the flow rates and the total pressure in the cell for each experiment.

2.2 Interface Studies

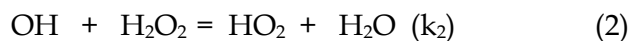
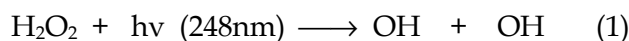
Vibrational Sum-Frequency Generation (VSFG) is a non-linear optical technique that selectively probes the vibrational spectra of molecules present exclusively at the interface [3]. This is primarily a three-wave mixing process with two input beams (IR and visible) and the third signal beam. The visible beam with 30 picosecond temporal width is fixed at 532 nm, and it is generated by frequency doubling of the fundamental output of a Nd:YAG laser (PL2241B, Ekspla, Lithuania). The other input beam is tunable in IR frequency region of 2.3-10.0 μm spectral range, generated in a difference frequency generator (DFG) by mixing the output of an optical parametric generator (OPG) with the

fundamental output (1064 nm) of the Nd:YAG laser in a silver thiogallate (AgGaS₂) crystal. The OPG (PG401, Ekspla) was pumped by the third harmonic (355 nm) beam of the Nd:YAG laser, using lithium triborate (LiB₃O₅) as a non-linear crystal. The angles of incidence were kept at 55° and 60° for the IR and visible laser beams, respectively. The SFG signal is generated at the frequency, ω_{SFG}, which is the sum of the visible (ω_{VIS}) and IR (ω_{IR}) input frequencies. The reflected IR and visible beams were blocked, and the SFG signal beam was separated and detected with a photomultiplier tube (PMT) after spatial, polarization and spectral filtering. Signal was collected at two different polarization schemes (*SSP* and *PPP*) for the CH (2750-3000 cm⁻¹) and OH (3000-3750 cm⁻¹) vibrational stretching regions. Each scan was obtained with a step size of 2 or 4 cm⁻¹ for the CH and OH spectral regions, respectively, and an average of 60 laser shots per point in each spectrum.

3. Results and discussions

3.1 OH Kinetics with Morpholine

The LIF intensity from OH radicals, generated by photolysis of H₂O₂ at 248 nm (reaction (1)), decreases with time because of their reaction with H₂O₂, in addition to the reaction with the reactant, that is, morpholine (C₄H₉NO). The diffusion of OH radicals from the detection zone also contributes to the decrease in the observed LIF intensity. The various processes are given as follows, where k₂, k₃, and k₄ are the rate constants for reactions 2, 3, and diffusion process 4, respectively.



$$-d[\text{OH}]/dt = [\text{OH}](k_2[\text{H}_2\text{O}_2] + k_3[\text{C}_4\text{H}_9\text{NO}] + k_4) \quad (5)$$

$$[\text{OH}]_t = [\text{OH}]_0 \exp\{-(k' + k_3[\text{C}_4\text{H}_9\text{NO}])t\} \quad (6)$$

Because $[\text{H}_2\text{O}_2]$ and $[\text{C}_4\text{H}_9\text{NO}]$ are almost constants during the decay of OH, the concentration of OH at any time, $[\text{OH}]_t$ is given by the first-order kinetics equation (Eqn. (6)) where $[\text{OH}]_0$ is the initial concentration of OH radicals and k' is $(k_2[\text{H}_2\text{O}_2] + k_4)$, the pseudo-first-order rate constant in the absence of morpholine (blank). Therefore, by varying $[\text{C}_4\text{H}_9\text{NO}]$, the bimolecular rate constant, k_3 , can be obtained. Typical decay profiles of logarithmic LIF intensities, obtained at different concentrations of morpholine at room temperature, exhibit good linearity with time. From the slope of each of these plots, the values of the pseudo-first-order rate constants, $k' + k_3 [\text{C}_4\text{H}_9\text{NO}]$, are obtained. We determined the bimolecular rate constant for reaction (3) at room temperature, $k_3(298)$, to be $(8.0 \pm 0.1) \times 10^{-11} \text{ cm}^3 \text{ molecule}^{-1} \text{ s}^{-1}$ by plotting these slopes against $[\text{C}_4\text{H}_9\text{NO}]$, as shown in Figure 1.

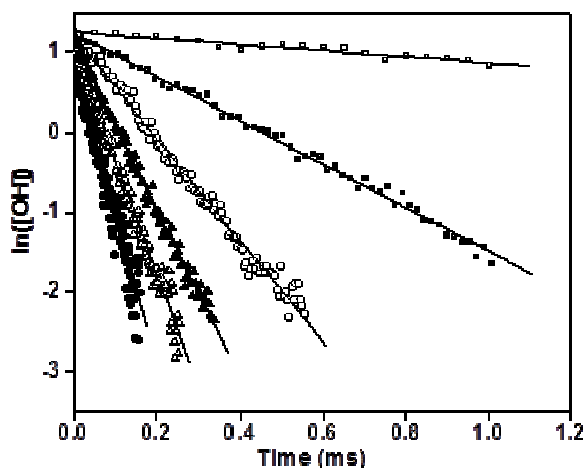


Figure 1. Typical profiles of OH radical decay with time at room temperature with increasing concentration of morpholine as follows: (A) 0; (B) 3.2×10^{13} ; (C) 8.1×10^{13} ; (D) 1.3×10^{14} ; (E) 1.8×10^{14} ; and (F) $2.3 \times 10^{14} \text{ molecules cm}^{-3}$. Time for reaching maximum concentration of OH (formation time) is neglected. The least-squares linear fits are shown as solid lines.

Any contribution to this rate constant from secondary reactions involving photolysis products of morpholine may be neglected here because our gas chromatography measurements, after irradiation of morpholine at 248 nm, did not show any depletion,

indicating the absence of photodissociation of morpholine at this wavelength. The values of the bimolecular rate constants ($k_3(T)$) at different temperatures and under experimental conditions are given in Table 1. The Arrhenius plot, where variation of $\ln(k_3(T))$ is plotted against inverse of temperature, is shown in Figure 2. The plot shows negative temperature dependence, with a slight curvature. The points can be still fitted reasonably well to a straight line, with a pre-exponential factor of $(1.1 \pm 0.1) \times 10^{-11} \text{ cm}^3 \text{ molecule}^{-1} \text{ s}^{-1}$ and activation energy (E_a/R) of $(-590 \pm 20) \text{ K}$ in the temperature range studied.

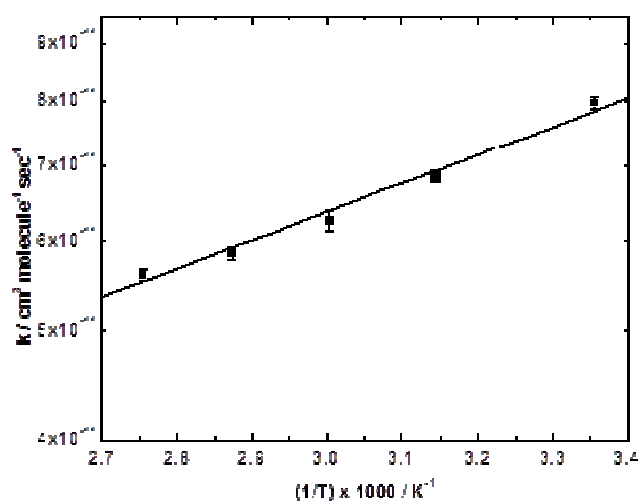


Figure 2. Arrhenius plots of the average value of OH reaction rate constants ($k_3(T)$).

The reaction of OH radicals with saturated molecules, like morpholine, is expected to be dominated by hydrogen abstraction. There are three different types of hydrogen atoms in this molecule, namely, hydrogen attached to (i) N-atom, (ii) C-atoms adjacent (α) to N-atom, and (iii) C-atoms α to O-atom. Consequently, different reaction channels, involving abstraction of these H atoms, are possible in morpholine. We have performed detailed ab initio studies using Gaussian 92 package [6] on the structures and energies of morpholine and that of the pre-reactive complexes and the TSs, involved in the different hydrogen abstraction channels, in order to understand the pathways of these. The geometries of the equilibrium structures of morpholine and the products, pre-reactive

complexes with OH, and the TS structures, were optimized at PMP2/6-311+G(d,p) level, and their energies were calculated at the MP2 level using the same basis sets. However, different conformers of morpholine were optimized at the MP2/aug-cc-pvdz level of theory (Figure 3). Our calculations show that the equatorial chair form of morpholine with H atom on nitrogen in the equatorial position, is the most stable form in the ground-state. The next most stable conformer was the axial chair form, just 1kcal/mol higher in energy. The least stable was the twisted boat form, at 7.6 kcal/mol due to high steric interaction (Figure 3). Even though the direct abstraction channels cannot be ruled out, the channels through pre-reactive complexes are considered to be predominant because of the observation of negative activation energy.

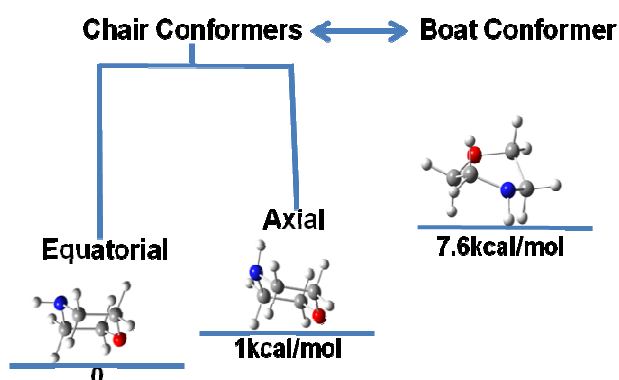


Figure 3. Different conformers of morpholine optimized at MP2/aug-cc-pvdz level of theory: (A) equatorial chair form; (B) axial chair form; (C) twist boat form.

Our calculations showed the existence of two types of pre-reactive complexes, namely, N-adduct (M1) and O-adduct (M2) as shown in Figure (4). In M1, the H atom of OH interacts with the N atom, and in M2, the H atom interacts with the O atom of the molecule. In the case of M2, the O atom of the OH moiety is away from the ring, which retains its structure, whereas in the case of M1, it is placed symmetrically above the ring. In M1, the distance between the H atom of OH and the N atom of the ring is 1.89 Å, whereas in M2, the corresponding distance to the O atom of the

ring is 1.86 Å, suggesting H-bond type interaction. The stabilization energies in both of these complexes are on the order of 5-7 kcal mol⁻¹, and the N-adduct is found to be more stable. The stabilization energy is almost similar to that of the previous calculations in the case of amino acids [7,8].

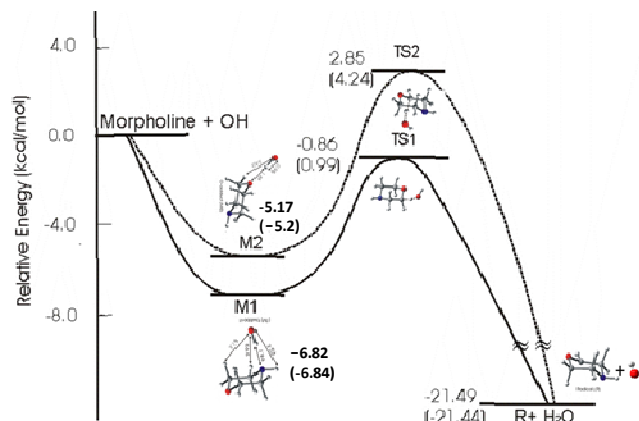


Figure 4. Schematic energy diagram of H abstraction reaction of OH radical with morpholine. Geometry optimization and calculation of energies are done at the PMP2(MP2)/6-311+G(d,p) level. The MP2 energies in kcal mol⁻¹ are shown in parentheses.

The pre-reactive complexes, M1 and M2, can subsequently undergo the H abstraction reaction. However, we could optimize only the TS structures involving the abstraction of the H-atom attached to the carbon atom α to oxygen atom in both of the pre-reactive complexes, shown in Figure 4 as TS1 and TS2 for M1 and M2, respectively. The difficulty in localizing additional TS could be due to the lack of a clear dividing energy barrier between all possible TSs. In TS1, the OH moiety, which was closer to N-atom in the pre-reactive complex, has moved away, and its O-atom has come closer to the H atom α to morpholine oxygen atom. The OH moiety in M2 rotates such that the O atom is closer to the H atom α to O atom in TS2. Therefore, it is observed that in both of the TSs, the O atom of the O-H group is closer to the H atom α to the O atom of the ring, the axial H-atom in TS1, and the equatorial H-atom in TS2. The distance between the H-atom to be abstracted and the

O-atom of OH is 1.37 Å in TS1 and 1.33 Å in TS2. The distances between the H-atom of the OH and the N (TS1) and O (TS2) atoms are 2.22 and 2.54 Å, respectively. Both of these TSs were found to lead to the same radical, R, as shown in Figure 4, even though the axial H-atom is removed from TS1 and equatorial H-atom is removed from TS2. The products are 21 kcal mol⁻¹ lower in energy as compared with the reactants. Previous calculations on morpholine radicals have shown that the radical formed by abstraction of H-atom α to N-atom is more stable (by 4.0 kcal mol⁻¹) than the one formed by abstraction of H-atom α to the O-atom [10]. The theoretically calculated bond dissociation energy of C-H bond α to N-atom is found to be 92.0 kcal mol⁻¹, close to the experimental value of 94.0 kcal mol⁻¹[11]. The dissociation energy of N-H bond in secondary amines is also reported to be 95 kcal mol⁻¹[11], similar to that of the C-H bond α to N atom. Therefore, abstraction of H-atom attached to N-atom and that attached to C-atom α to N-atom, seems to be equally probable energetically, although the latter is considered to be dominating[11]. However, in the present case, which involves pre-reactive complex, the bond dissociation energy may not be the only factor in deciding the probability of bond dissociation process. The absence of pressure dependence of the room-temperature rate constant in the total pressure of 35-75 Torr range suggests that the pre-reactive complexes are collisionally stabilized before the subsequent abstraction reaction. Similar temperature and pressure dependence and experimentally observed pre-exponential factors are reported in many reactions of OH radicals with oxygenates such as acetaldehyde [12], but the activation energies are less negative (positive in the case of trioxane), as compared with that for morpholine observed in this work. Therefore, the presence of the N-atom in morpholine is found to have a profound effect on its reaction with the OH radical. The rate constants observed for morpholine, which is a secondary amine, are marginally higher than those reported for secondary amines [7,8], and the activation energy is more negative. The

theoretically computed overall rate constant at room temperature for all possible pathways, in the case of amino acids, such as serine, is very close to that observed here for morpholine. As previously mentioned, the relative energy of pre-reactive complex and TSs computed for the amino acids was found to be similar to that of morpholine. Therefore, it can be seen that the formation of pre-reactive complexes, negative activation energy, and very high rate constants are common features of OH radical reactions with amines, more prominent than that in the case of oxygen compounds.

3.2 Dynamics of Morpholine Photodissociation

The OH radical was detected among the photoproducts, by its rotationally resolved LIF spectrum. Figure 5 shows a part of the (0,0) band of the A² Σ^+ -X ² Π system of OH. No signal was observed from the (1,1) band of the same system. The rotational lines have been assigned following the assignments made by Dieke and Crosswhite [13]. After the intensities

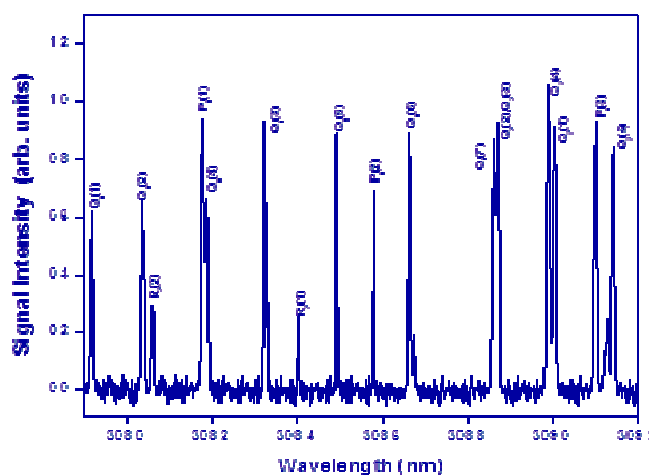


Figure 5. Portion of the LIF excitation spectrum of A² Σ^+ -X ² Π transition of the OH radical formed by photolysis of morpholine (about 100 mTorr) at 193.

of the rotational lines were normalized with respect to the photolysis and the probe laser intensities, pressure of the sample inside the reaction cell, and Einstein's coefficients B_{ij} [14], a plot of the natural log of the normalized intensities of individual lines (P_{ij}) versus the energies of rotational levels (e_{ij}), could be fitted

to a straight line. This shows that the rotational levels of the nascent OH radical have completely equilibrated during the dissociation process. From the slope of the Boltzmann's line, the average rotational energy of the OH radical was calculated to be 1.0 ± 0.02 kcal/mol. From the Doppler bandwidth of the rotational lines, translational energy of the OH fragment was calculated to be $E_{CM,T} = 19.6 \pm 0.8$ kcal/mol. The ratio of the intensities of $P_1(Q_1)$ and $P_2(Q_2)$ lines, respectively, was found to be less than unity for all the values of N studied, which suggests that $2\Pi_{1/2}$ level is

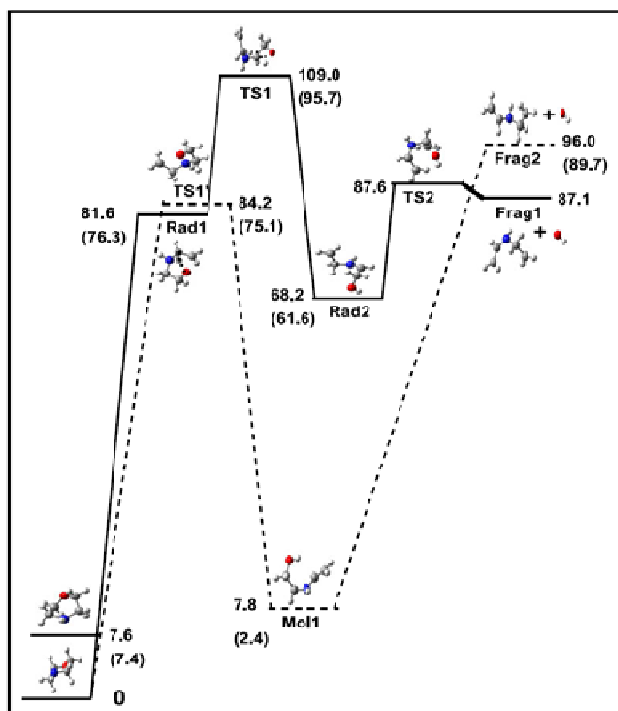


Figure 6. Potential energy curves of the different OH formation channels. The geometry is optimized at B3LYP/6-311+G(d,p) level of theory and the energies are calculated at MP4(SDQ) and B3LYP level of theory using the same basis sets. The last step of the triplet channel is optimized at HF/6-311+G(d,p) level. All energies are given in kcal/mol unit.

preferentially populated at all the rotational numbers. The Λ -doublet splitting arises due to the interaction between orbital angular momentum and nuclear rotation, and this interaction is of different magnitude for two Λ -

doublet states, $2\Pi^+(A')$ and $2\Pi^-(A')$. A typical plot of the relative intensities of the P lines and the Q lines vs. N shows that both the states are equally populated at all the rotational levels, as the ratio lies close to unity.

The partitioning of energy is mainly dependent on the nature of the transition state on the dissociative potential energy surface. Hence, from the distribution of the available energy among the different degrees of freedom of the products, valuable information about the mechanism of the reaction can be obtained. A quantitative examination of the available energy distribution can be done by two limiting models, the impulsive (applicable in the case of dissociation over a repulsive surface) and the statistical (mostly applicable in the case of dissociation without an exit barrier) models. We have estimated the energy distribution of the reaction under study by both of the above two models, and the partitioning obtained is tabulated in Table 2. On comparing the experimental partitioning with those obtained from the limiting models, it is clear that none of the models can actually explain the observed results. Since OH is not formed by a primary process, and a number of intermediate steps are present between the reactant and the products, this type of discrepancy is expected. The experimental results show that a large fraction of the available energy ($\sim 35\%$) is partitioned to the relative kinetic energy of the fragments, which suggests the presence of a considerable exit barrier in the reaction channel.

Theoretical calculations for the formation of OH radical from morpholine were carried out using GAUSSIAN 92 package [6]. All the geometry optimizations were done at B3LYP level of theory, using 6-311+G(d,p) basis sets, whereas the potential energy of each molecular species was calculated at MP4 (SDQ) and B3LYP level of theories, using the same basis sets. In Figure 6, the potential energy surface is schematically represented by indicating the energy of each species. The energy value outside parentheses is obtained, using MP4(SDQ)/6-311+G(d,p) level of theory, and that within the parentheses, is obtained at

B3LYP/6-311+G(d,p) level. Both the boat and the chair conformations of the morpholine molecule are found to be stable, with the latter more stable by 7.6 (7.4) kcal/mol, as expected for cyclic saturated compounds. Theoretical studies indicate that the first step of dissociation of morpholine can be cleavage of either a C-O bond or a C-N bond. The cleavage of the C-O bond will lead to formation of a triplet biradical, represented as Rad1 in Figure 6. This biradical undergoes intramolecular rearrangement, involving the transfer of an H atom from a C atom to the O atom, followed by C-O bond breaking. All the intermediates and the products involved in this pathway are triplets; hence, this pathway is referred as the triplet pathway, and represented by the solid lines in Figure 6.

In an alternative pathway, the C-O bond breaking and H migration from a C atom to the O atom are concerted. This step generates a stable molecule, which is an open-chain alcoholic isomer of morpholine marked as Mol1 in Figure 6. This stable molecule is in singlet spin state, and hence we refer this pathway as the singlet pathway, in our discussions. Energized Mol1 can lead to OH formation by a direct scission of the C-OH bond. This singlet pathway is shown by the broken lines in the Figure 6. The C-N bond is weaker than the C-O bond by about 4 kcal/mol, but, to generate OH radical, the C-O bond has to be broken only after C-N bond is cleaved. Hence the energy requirement of the OH pathways via the C-N bond cleavage is higher. Therefore, the contribution of the pathway, which starts with C-N bond to the overall OH formation, is negligible. The major channels are thought to start with the C-O bond cleavage.

In our theoretical calculations, a small energy barrier (0.5 kcal/mol) could be located in the Triplet pathway, but none in the Singlet pathway. Since the reaction channels involve

multiple steps, some of which require high-activation energy, the effect of those barriers will manifest in the overall energy distribution of the reaction, even though the last product-forming step itself may not have a high-activation barrier. Thus, the dissociation dynamics of morpholine at 193 nm was found to be quite similar to other cyclic ethers [15-17].

3.3. Morpholine on Interface: VSG Studies

3.3.1. Pure Liquid Morpholine

The VSG spectra of pure liquid morpholine at room temperature in both SSP and PPP polarizations were recorded. Since morpholine molecule has only CH₂ groups, the region between 2700-3000 cm⁻¹ (Figure 7) exhibits generally the CH₂ stretching vibrations. From Figure 6, we can see seven vibrational resonances in the SSP(PPP) spectrum at 2791(2793), 2826(2826), 2855(2857), 2872(2876), 2916(2918), 2942(2946) and 2969(2969) cm⁻¹, and these are listed in Table 3.

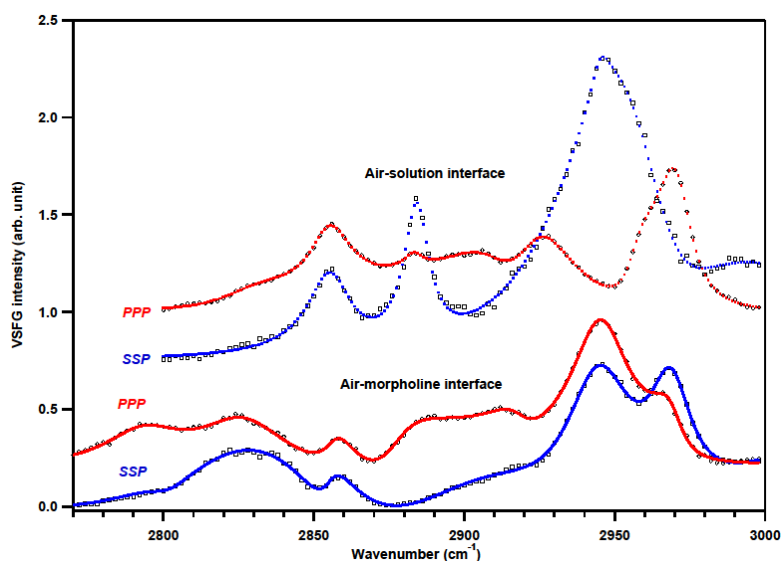


Figure 7. CH stretching frequencies in VSG spectra at air-morpholine and air-solution interfaces with SSP and PPP polarizations. Solid and dotted lines are fit to the experimental data.

These resonances in the two polarizations have different relative amplitudes, but similar frequencies, as expected. Based on the polarization selection rules and nature of these bands in Raman

spectra, these stretching modes can be assigned either symmetric or asymmetric vibrational modes. Based on the comparison between VSFG spectra and the Raman spectra, the VSFG frequencies at 2791, 2826, 2855, 2942 and 2969 cm^{-1} can be assigned to symmetric stretching modes. On the other hand, vibrational bands at 2872 and 2916 cm^{-1} are expected to be asymmetric. In our VSFG measurements, negligibly small signal is observed in the region of 3000-3900 cm^{-1} SSP polarization (Figure 8(A)). However, a weak and broad feature in the region of 3000-3850 cm^{-1} is observed in the PPP polarization (Figure 8(B)). This suggests that, probably, the net orientation of most of the N–H bonds along the surface normal is either negligible or non-existent. The two conformers of morpholine, however, cannot be distinguished at the interface by their N–H stretching peak.

VSFG spectra of very dilute solution of morpholine, in the concentration range of 10 mM to 60 mM in both SSP and PPP polarization combinations, and found that the VSFG intensities of morpholine solutions are greater than that of neat morpholine, and the difference between the spectra in SSP and PPP polarizations are higher with respect to that in neat liquid morpholine (Figure 7). VSFG intensities of the CH_2 stretch frequencies increase with increasing bulk concentration of morpholine solution. The increase in SFG signal intensity with increasing concentration can be attributed to the increase in the surface concentration of morpholine molecules as the bulk concentration increases. In the SSP spectra, instead of seven vibrational bands as observed for liquid morpholine, only five bands were observed at 2854, 2883, 2926, 2945 and 2969 cm^{-1} for the solution. In solution, two bands at lower frequencies disappear, and

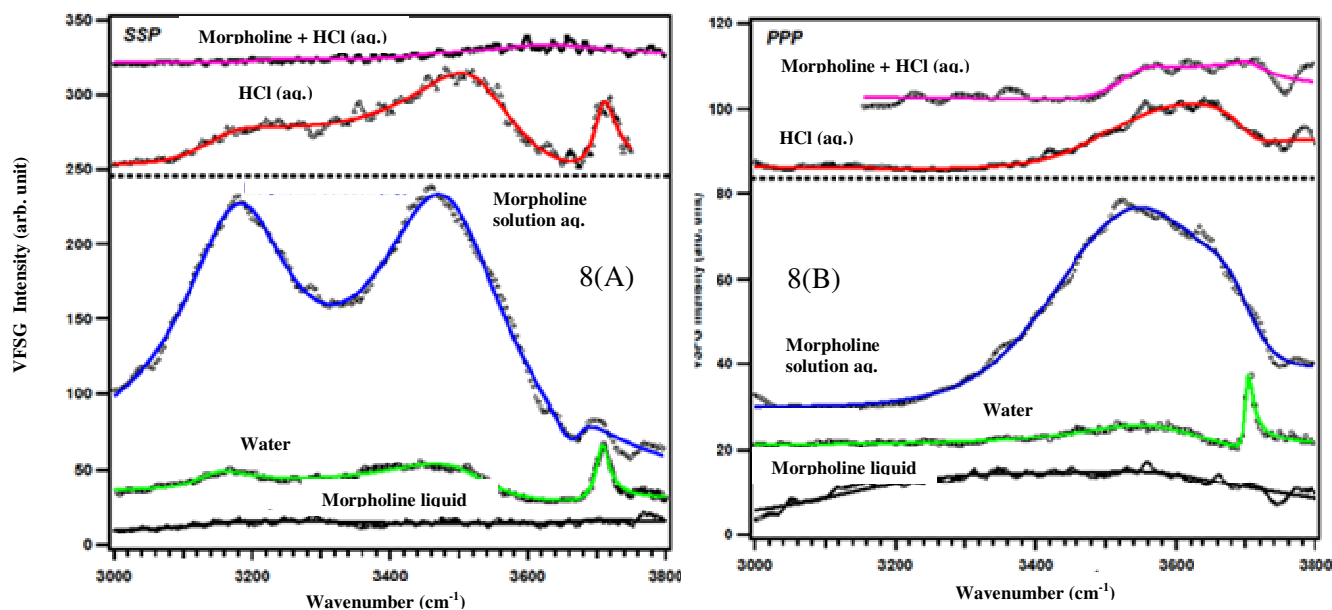


Figure 8. Comparison of OH stretching bands in VSFG spectra of air-water, air-morpholine, air-morpholine solution, air-HCl solution, and air- (morpholine + HCl) solution interfaces for SSP (A) and PPP (B) polarizations.

3.3.2. VSFG Spectra of Morpholine Aqueous Solution

Morpholine is readily soluble in water, and forms hydrogen bonds through both its N–H centre and O-centre in presence of highly polar H_2O molecules. We studied the

others have enhanced VSFG intensities. Moreover, some stretch frequencies are shifted to higher wavenumbers. VSFG spectrum of morpholine at the air-solution in the PPP polarization, also shows that some peaks vanish and others get modified (Figure (7)). The band at 2793 cm^{-1} due to equatorial chair conformer at the air-morpholine interface

vanishes at the air-solution interface, and the band at 2876 is blue-shifted to 2882 cm^{-1} .

Based on the above spectral results we can suggest that there is a significant change in the conformation and orientation of morpholine molecules at the air-solution interface in comparison to that at the air-morpholine interface. The changed conformation can be due to different relative composition of equatorial and axial chair form or due to that of chair and boat/twisted boat form of morpholine. In general, the calculated CH_2 stretch frequencies for the axial chair form are observed at higher wavenumbers than that for the equatorial chair form of morpholine [18, 19]. Probably the axial chair form is more abundant than equatorial chair at the air-morpholine interface, and its relative abundance is still higher at the air-solution interfaces. These conclusions can be supported by the presence of vibrational bands 2791 and 2826 cm^{-1} (belonging to the equatorial chair conformer of morpholine) in VSG spectra with the *SSP* polarization at the air-morpholine interface, but absence of these bands at the air-solution interface (depicted in Figure 7). A higher fraction of the axial chair conformer at the air-solution interface can explain the enhanced intensity of the bands at 2945 cm^{-1} [19]. Additionally, morpholine molecules might have a boat/twisted boat structure at the air-solution interface. Unlike the chair conformers, boat conformer has both the polar centres, the NH bond and the O-atom, oriented to the same side of the planar CCCC ring backbone as can be seen from its optimized structure (shown in Figure 3). Hence, on the surface, if lying flat, this conformer can have the unique energetically favourable alignment where both the polar parts stay inside the polar environment of bulk water, and the non-polar CH bonds remain directed into the air. This alignment can have extra stabilization because of the polar-polar interaction of the water-NH/water-O regions, and can avoid the polar-non polar interaction for the water-CH region.

A typical spectrum of morpholine solution (40 mM) in comparison to pure water

and liquid morpholine is shown in Figure 8(A and B). In the *SSP* polarization as seen in Figure 8(A), both the OH stretch modes due to hydrogen bonded water molecules at 3250 and 3450 cm^{-1} in the VSG spectra get enhanced in the presence of morpholine, due to polar orientation of interfacial water molecules induced by hydrogen bonded interaction between morpholine and water molecules. The sharp peak at $\sim 3700 \text{ cm}^{-1}$ is drastically reduced. Thus most of the free OH bonds on the surface of water are engaged in hydrogen bonding with the morpholine molecules. In the *PPP* spectrum of the 10-60 mM solution of morpholine (Figure 8(B)), a single broad peak at 3555 cm^{-1} is observed. This peak is around 20 cm^{-1} blue shifted compared to the typical peak at 3530 cm^{-1} of pure water. Intensity of this peak increases with increasing bulk concentration of morpholine, indicating the role of increased surface concentration. This frequency also falls in the range of 3520-3650 cm^{-1} , which includes OH stretching in an asymmetric environment [18], antisymmetric OH stretching [19], and water molecules with fewer hydrogen bonds, that give prominent OH stretches in cluster studies [20-22]. Polarization dependent symmetry analysis attributed this broad 3550 cm^{-1} peak to the other OH group of the same water molecule with the "free OH" group at the top-most layer of the air/-water interface [23]. High intensity peak in this region again justifies our inference drawn from the *SSP* spectrum of morpholine solution, that is, the morpholine molecules get hydrogen bonded to the "free OH" group of the water molecules at the interface and increase their net orientation. On the other hand, the disappearance of the "free OH" peak at 3700 cm^{-1} at all polarizations indicates that on the topmost surface, almost all interfacial water molecules are hydrogen bonded to morpholine molecules, leaving no free OH.

These two observations together suggest that the morpholine molecules on the topmost surface engage the water molecules in hydrogen bonding where the O atom of H_2O molecule can donate proton to both the N-atom

and the O-atom of the morpholine molecule, and can accept proton from its N–H bond.

3.3.3. Effect of HCl

Most of the atmospheric reactions at the interface happens on the surface of aerosol droplets, which is known to be acidic compared to bulk water due to accumulation of H_3O^+ ions on the surface [3]. Multiple reports are available which discuss the effect of acid on the surface structure of water. Baldelli et al. [20] carried out a detailed study on effect of HCl addition on water surface, with HCl concentration varying from 0.01 to 0.22 mole fraction. In presence of HCl, which completely ionizes in aqueous environment, both morpholine and water molecules are capable of getting protonated. To understand how the orientation and structure of morpholine and water molecules change at the air-solution interface in presence of acid, we studied the effect of acid addition to morpholine solutions of different concentrations. 300 μl of concentrated HCl was added to 10 ml volume of morpholine solution with concentrations of 10, 20, 30, 40, 50 and 60 mM and allowed to equilibrate for 12 hours. The concentration of acid in these solutions was around 300 mM.

In the SSP spectrum (Figure 9(A)), the peak at 2851 cm^{-1} remains unchanged in all concentrations of morpholine, but the peak at 2880 cm^{-1} loses its intensity as morpholine concentration increases. As the morpholine concentration increases, however, in the SSP spectrum, a new peak builds up at 2932 cm^{-1} , and the peak at 2953 cm^{-1} slowly loses its

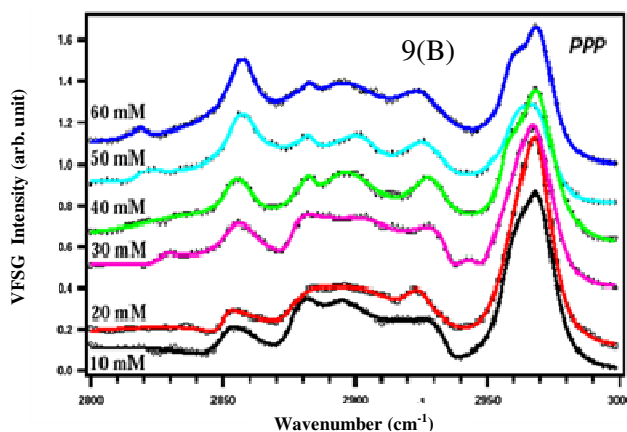
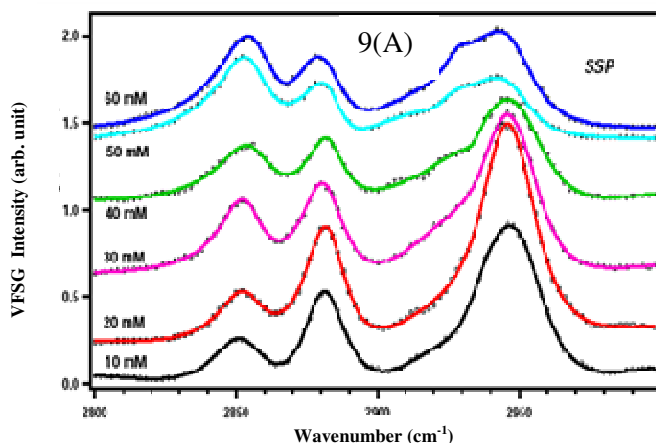


Figure 9. CH stretching frequency region in the VSG spectra of air-HCl solution interface at different morpholine concentrations with SSP (A) and PPP (B) polarizations. Solid lines are fit to the experimental data.

intensity. In the PPP spectrum (Figure 9 (B)), the peak at 2851 cm^{-1} increases with increasing morpholine concentration but the peaks at 2877 , 2894 and 2933 cm^{-1} follow the opposite trend. The vibrational band observed at 2956 cm^{-1} at the air-solution interface is not seen at lower concentrations on addition of HCl, but with increasing morpholine concentration, it starts building up. However, the peak at 2971 cm^{-1} at the air-solution interface remains unchanged on addition of HCl and its intensity remains independent of morpholine concentration in presence of HCl. Earlier it was observed that the peak positions in the Raman spectrum of CH_2 vibrational modes of morpholine changes significantly by addition of dilute acid [21]. These changes were attributed to two probable effects, protonation of the N-H group, and change in the relative concentrations of different conformers due to favourable interactions with the surrounding environment. Both of these effects may also be responsible for the change in the SFG spectrum of morpholine solution in presence of HCl. The fact that we can see additional changes in the VSG spectrum as morpholine concentration increases in presence of HCl of same strength, must be attributed to the change in the structure and orientation of morpholine molecules on the interface. In our experiments,

concentration of HCl (300 mM) is always much higher than the morpholine concentration (10-60 mM), so all morpholine molecules are expected to get protonated. In such scenario, the distinction between the axial and equatorial chair conformers get obliterated, but the distinction between chair and boat conformers still exists.

In the 3000-3800 cm^{-1} region, the VSFG intensity due to hydrogen bonded H_2O molecules in pure water and aqueous solution of morpholine decreases both in *SSP* and *PPP* spectra on addition of HCl, as shown them in Figure 7(A) and 7(B). The recorded spectra showed that both HCl (300 mM) and morpholine (60 mM), when present individually, increases the intensity of all the peaks of hydrogen bonded water (two broad peaks at 3250 cm^{-1} and 3450 cm^{-1} in *SSP* polarization and a single broad one at 3533 cm^{-1} in *PPP* polarization). But, when they are present together, as in the solution of morpholine in 300 mM HCl, all these peaks are almost completely obliterated. In the *SSP* spectrum, a very weak and broad signal is visible roughly centered at 3615 cm^{-1} . Richmond et al.[22] have assigned this peak to water molecules in the topmost layer that interacts with organic molecules. This high frequency peak is not expected from highly coordinated OH species, but rather from species with few hydrogen bonds, i.e., symmetric OH stretching of weakly hydrogen bonded water molecule [23]. The peak at 3700 cm^{-1} is also completely vanished, indicating negligible number of "free OH" groups on the surface. In the *PPP* polarization, a single strong broad peak is observed in aqueous solution of morpholine roughly centered at 3560 cm^{-1} . This peak has been assigned to symmetric OH stretching of weakly hydrogen bonded water molecules (double donors) [23]. On addition of HCl, this peak is somewhat blue shifted and reduced in intensity, which is identical with that of only HCl solution, as can be seen from Fig. 8(B). Since these peaks are much blue shifted from that of pure water, (3533 cm^{-1}), the hydrogen bonding among the interfacial water

molecules is considered to become weaker as HCl is added to morpholine solution.

In presence of both morpholine and HCl, $\text{C}_4\text{H}_9\text{NHO}^+$ cations, softer than protons, accumulate closer to the surface and thus decrease the distinction between anion-cation bilayer, which eventually brings down the ordering of hydrogen bonded network of water molecules. Presence of large number of charged centres also weakens the water-water H-bonding. At lower concentration of morpholine, this effect is much more prominent for decreasing the inherently weaker intensity OH stretching vibrations, compared to much intense CH stretching vibrations, hence the former is almost obliterated but the latter is still visible. As morpholine concentration increases, the effect becomes stronger even for CH stretching vibrations as we have discussed in the previous section.

4. Conclusion

Kinetics studies on the reaction of the OH radical with morpholine reveal high rate constant ($8.0 \pm 0.1 \times 10^{-11} \text{ cm}^3 \text{ molecule}^{-1} \text{ s}^{-1}$ at 298 K) and negative temperature dependence ($k = (1.1 \pm 0.1) \times 10^{-11} \exp[(590 \pm 20)/T] \text{ cm}^3 \text{ molecule}^{-1} \text{ s}^{-1}$) indicating involvement of a stable pre-reactive complex due to the H-bond interaction between the OH radical and N/O atom of morpholine. The pre-reactive complex involving N atom was found to be more stable than that with O atom.

The dynamics investigation of OH generation channel from the photo-excited morpholine molecule at 193 nm revealed that morpholine, like some cyclic ethers and epoxides, produces OH radical as one of the products when photolyzed at 193 nm. Since the molecular structure of morpholine does not contain any OH group, its formation channel must involve intramolecular rearrangements. The OH formation channel was found to follow the general route of ring opening, intramolecular rearrangement, involving H atom shift from C atom to O atom, and finally, cleavage of C-OH bond to free the OH radical. The presence of an extra heteroatom (N) may

open another route for ring opening, but the contribution of this channel to the formation of OH radical is found to be negligible.

Vibrational sum-frequency generation (VSFG) spectroscopy was employed to investigate the structure and orientation of morpholine at the air-morpholine and air-solution interfaces, and also in presence of HCl. The CH stretch intensity in VSFG spectra due to interfacial morpholine molecules at the air-solution interface increases with increasing bulk concentration of morpholine solution, because of its increasing surface concentration. The CH stretch intensity is also enhanced at the air-solution interface in comparison to that at the air-morpholine interface. Similarly, the OH stretch intensity due to interfacial water molecules is enhanced at the air-solution interface. These results suggest increased polar orientation of interfacial morpholine and water molecules due to mainly hydrogen bonded interaction between them. In addition, the equatorial chair conformation of morpholine molecules at the air-morpholine interface changes to the axial chair or probably a twisted boat conformation at the air-solution interface contributing to the enhanced VSFG intensity in the CH region. However, the increased polar orientation of interfacial water molecules, induced by morpholine molecules, is lost on addition of dilute HCl solution, and it becomes random with almost absence of VSFG intensity in the OH stretch region.

References:

- [1] A. Subramanian, R. Gopalakrishnan, C. Boopathi, K. Balakrishnan, T. Vasudevan, M. Natesan and N. S. Rengaswamy, *Bull. Electrochem.*, 1998, **14**, 289-290.
- [2] J. Kielhorn and G. Rosner, *Morpholine; Environmental Health Criteria 179*; World Health Organization: Geneva, 1996.
- [3] Y. L. S. Tse, C. Chen, G. E. Lindberg, R. Kumar, G. A. Voth, *J. Am. Chem. Soc.*, 2015, **137**, 12610-12611.
- [4] Y. R. Shen, *Nature*, 1989, **337**, 519-525.
- [5] S. SenGupta, Y. Indulkar, A. Kumar, S. Dhanya, P. D. Naik, and P. N. Bajaj, *J. Phys. Chem. A* 2010, **114**, 7709-7715
- [6] Frisch, M. J.; et al. *Gaussian 92*, revision E; Gaussian, Inc.:Pittsburgh, PA, 1992.
- [7] A. Cruz-Torres, A. Galano, J. R. Alvarez-Idaboy, *Phys. Chem. Chem. Phys.* 2006, **8**, 285-292.
- [8] A. Galano, J. R. Alvarez-Idaboy, A. Cruz-Torres, M. E. Ruiz-Santoyo, *THEOCHEM* 2003, **629**, 165-174.
- [9] D. D. M. Wayner, K. B. Clark, A. Rauk, D. Yu, D. A. Armstrong, *J. Am. Chem. Soc.* 1997, **119**, 8925-8932.
- [10] L. J. J. Laarhoven, P. Mulder, D. D. M. Wayner, *Acc. Chem. Res.* 1999, **32**, 342-349.
- [11] J. Laleve'e, X. Allonas, J.-P. Fouassier, *J. Am. Chem. Soc.* 2002, **124**, 9613-9621.
- [12] L. Zhu, R. K. Talukdar, J. B. Burkholder, A. R. Ravishankara, *Int. J. Chem. Kinet.* 2008, **40**, 635-646.
- [13] G.H. Dieke, H.M. Crosswhite, *J. Quant. Radiat. Transfer* 1962, **2**, 97-199.
- [14] J.L. Chidsey, D.R. Crosley, *J. Quant. Spectrosc. Radiat. Transfer* 1980, **23**, 187-199.
- [15] S. SenGupta, H.P. Upadhyaya, A. Kumar, P.D. Naik, P.N. Bajaj, *J. Chem. Phys.* 2005, **122**, 1243309(1-8).
- [16] S. SenGupta, H.P. Upadhyaya, A. Kumar, P.D. Naik, P.N. Bajaj, *J. Chem. Phys.* 2006, **124**, 024305(1-7).
- [17] A. Kumar, S. SenGupta, K.K. Pushpa, P.D. Naik, P.N. Bajaj, *Chem. Phys. Lett.* 2006, **430**, 240-246.
- [18] M. Xie, G. Zhu, Y. Hu, H. Gu, *J. Phys. Chem. C*, 2011, **115**, 20596-20602.
- [19] D. Vedal, O. H. Ellestad, P. Klaboe, G. Hagen, *Spectrochimica Acta*, 1976, **32A**, 877-890.
- [20] S. Baldelli, C. Schnitzer, M. J. Schultz, *Chemical Physics Letters*, 1999, **302**, 157-163.
- [21] S. Ashtekar, P. J. Barrie, M. Hargreaves, L. F. Gladden, *Angew. Chem. Int. Ed. Engl.*, 1997, **36**, 876-878.
- [22] T. L. Tarbuck, G. L. Richmond, *J. Phys. Chem. B*, 2005, **109**, 20868-20877.
- [23] Scherer, J. R. *The Vibrational Spectroscopy of Water*; Heyden: Philadelphia, 1978; Vol. 5.

List of Tables:

Table 1: Summary of the Experimental Conditions and Rate Constants for the Reaction OH + Morpholine at Different Temperatures

Temperature (K)	Pressure (torr)	[Morpholine] (molecule cm ⁻³)	k _{II} (cm ³ molecule ⁻¹ s ⁻¹)
298	54	3.2 × 10 ¹³ - 2.3 × 10 ¹⁴	(8.0 ± 0.11) × 10 ⁻¹¹
318	48	2.7 × 10 ¹³ - 1.9 × 10 ¹⁴	(6.8 ± 0.08) × 10 ⁻¹¹
333	55	2.9 × 10 ¹³ - 2.5 × 10 ¹⁴	(6.2 ± 0.13) × 10 ⁻¹¹
348	54	2.7 × 10 ¹³ - 2.4 × 10 ¹⁴	(5.8 ± 0.08) × 10 ⁻¹¹
363	56	2.6 × 10 ¹³ - 1.9 × 10 ¹⁴	(5.6 ± 0.06) × 10 ⁻¹¹

Table 2: Experimentally obtained energy distribution of the OH channel in the photodissociation of morpholine at 193 nm and its comparison with that obtained by employing statistical and impulsive models. Energies for both the triplet and the singlet channels are given, the latter within parentheses. $E_{available} = 52.4$ (58.1) kcal/mol.

	E _T (CM)	E _R (OH)	E _{vib} (OH)	E _{int} (cofrag)
Experimental	19.6 ± 0.8 (19.6 ± 0.8)	1.0 ± 0.2 (1.0 ± 0.02)	0	31.8 ± 1.3 (37.5 ± 1.7)
Impulsive	4.1 (4.4)	2.5 (2.8)	0.2 (0.1)	45.6 (50.8)
Statistical	26.3 (29.1)	1.3(1.5)	0(0)	24.8 (27.5)

Table 3.: Observed C-H Stretch Vibrational Frequencies of Pure Liquid Morpholine, Its Aqueous Solution, and Aqueous Solution in the Presence of HCl in VSFG Spectra.

C-H stretch VSFG frequencies of Morpholine		
Air-morpholine	Air-solution	Air-HCl(aq.)
2791 (2793)	----	----
2826 (2826)	---- (2825)	---- (2832)
2855 (2857)	2854 (2855)	2851 (2851)
2872 (2876)	2883 (2882)	2880 (2877)
2916 (2918)	---- (2912)	2894 (2894)
----	2926 (2923)	2932 (2933)
2942 (2946)	2945 (2945)	2953 (2956)
2969 (2969)	2969 (2971)	---- (2971)



Dr. Sumana SenGupta obtained her M. Sc. Degree from university of Calcutta in the year 2001, and obtained her Ph.D. degree from Homi Bhabha National institute in 2012. She joined Bhabha Atomic research centre in 2002. Her current interest lies in the research and development in chemistry of environmentally important molecules in the gas phase and different interfaces.